

Nano-Photonic Systems Incorporating Single III-V Semiconductor Quantum Dots

Qingqing DUAN



Submitted for the degree of Doctor of Philosophy

Department of Physics and Astronomy

The University of Sheffield

August 2019

Dedicated to my daughter Hermione, my partner and my parents.

Abstract

This thesis focuses on III-V semiconductors single quantum dot properties and on-chip optical cavities, which are potential building blocks for integrated quantum optical circuits.

A fundamental investigation of electron and nuclear spin properties in GaAs/AlGaAs nanohole-filled droplet epitaxial dots is performed using photoluminescence and photoluminescence excitation spectroscopy. A close-to-zero electron g -factor for such QDs is revealed, opening up a potential route for independent control of on-chip QD spin qubits by electrodes. Optical manipulation of the nuclear spin is achieved with an efficient dynamic nuclear polarization degree as large as 65%. The internal structural properties of this type of quantum dots is investigated using nuclear magnetic resonance spectroscopy, revealing the direction and magnitude of strain. Nuclear spin relaxation times of such dots are measured with values over 500 s, indicating a stable nuclear spin bath.

Numerical simulations, theoretical model calculations and experimental investigations are applied to on-chip photonic crystal molecules, demonstrating a continuous and simple route to tune the coupling strength and mode symmetry of the coupled states using end-hole displacement. This demonstration opens up the possibility of new studies of fundamental phenomena such as spontaneous symmetry breaking, long distance radiative coupling and superradiant effects.

Narrow notch filtering and the Purcell enhancement of a single QD emission are achieved in waveguide-coupled ring resonator devices. Mode structures and transmission spectra are measured using photoluminescence spectroscopy measurements. Whispering gallery mode ring resonators provide a possible route to on-chip filtering and optical switching.

Acknowledgements

Firstly, I would like to thank my supervisors Dr. Luke Wilson, Dr. Evgeny Chekhovich and Professor Maurice Skolnick for offering me the chance to study for my PhD in the LDSD group in the University of Sheffield. I have been most fortunate to study with so many adept individuals. I owe particular thanks to Professor David Whittaker for all his, very much appreciated, help and guidance. In addition, this thesis would not be complete without thanking Dr. Ata Ul Haq who spent many hours working with me in the lab during my first year, Dr. Rikki Coles who taught me the simulation software and helped me in the lab during my second year, and Dr. Andrew Foster who helped develop the experimental setup. I would also like to thank the collaborator Dr. Liming Liao for his contributions and numerous discussions. I'm also very grateful to Dr. Deivis Vaitiekus and Dr. Ben Royall for fabricating the photonic crystal cavities and ring resonators.

I'd also like to extend my acknowledgment to all my fellow PhD students who have been the source of many interesting discussions and have created an entertaining working environment.

Finally, I must thank my friends and family who have supported me throughout my PhD studies. In particular, my darling daughter Hermione who has made my PhD so special and meaningful. It's my great fortune to have her and to watch her growing up.

Author's Declaration

I declare that the work presented in this thesis, except where otherwise stated, is based on my own research and has not been submitted previously for a degree in this or any other university. Parts of the work reported in this thesis have been published as follows:

Publications

- Ulhaq, **Q. Duan**, E. Zallo, F. Ding, O. G Schmidt, A. I. Tartakovskii, M. S. Skolnick, and E. A. Chekhovich*. "*Vanishing electron g factor and long-lived nuclear spin polarization in weakly strained nanohole-filled GaAs/AlGaAs quantum dots*". Physical Review B 93, 165306 (2016)
- **Q. Duan**, D.M. Whittaker*, L. Liao, D. Vaitiekus, M.S. Skolnick, and L.R. Wilson*, "*Tuning the coupling strength and mode symmetry of photonic molecules using end-hole displacement*". (Submitted)

Signed

Qingqing Duan 殷清清

QINGQING DUAN

31st August, 2019

Contents

1 Introduction.....	1
1.1 Outline and Scope	1
1.2 Growth of Semiconductor Quantum Dots.....	2
1.3 Physical Properties of Self-assembled Quantum Dots.....	5
1.3.1 Density of States	5
1.3.2 Band Structure	6
1.3.3 Bright Excitons and Dark Excitons.....	9
1.3.4 Hyperfine Interactions.....	9
1.4 Quantum Dots in Magnetic Fields.....	10
1.5 Quantum Dot-Cavities Interaction.....	11
1.5.1 Typical Cavities	11
1.5.2 Quality Factor of Cavity.....	13
1.5.3 Basic Concept of Cavity QED.....	14
1.5.4 Inter-Cavity Coupling.....	16
References	19
2 Simulation Methods	26
2.1 Finite Different Time Domain (FDTD).....	26
2.1.1 Principle of Operation	27
2.1.2 Grid and Step Size Considerations	31

2.1.3	Boundary Conditions.....	32
2.1.4	“2.5D” FDTD.....	34
2.2	Guided Mode Expansion (GME)	34
2.2.1	Basic Configuration of GME.....	35
2.2.2	General Eigen Value Problem.....	35
2.2.3	Advantages of GME Method.....	36
2.3	Comparison with FDTD Method	36
	References.....	38
3	Experimental Methods.....	39
3.1	Fabrication of the Photonic Crystal L3 Cavities and Ring-Resonators	39
3.2	Photoluminescence Spectroscopy of Photonic Devices	40
3.3	Characterization of NFDE QDs.....	43
	References.....	46
4	Vanishing Electron g Factor and Long-Lived Nuclear Spin Polarization in	
	Weakly Strained Nanohole-Filled GaAs/AlGaAs.....	47
4.1	Introduction	47
4.2	Samples and Techniques.....	49
4.3	Experimental Results.....	49
4.3.1	Magnetic Properties of Single Charges.....	50
4.3.2	Optical Dynamic Nuclear Polarization (DNP).....	59
4.3.3	Nuclear Magnetic Resonance (NMR) Spectroscopy.....	70
4.3.4	Long Nuclear Spin Relaxation Times.....	78
4.4	Summary.....	81

References.....	82
5 Tuning the Coupling Strength and Mode Symmetry of Photonic- Molecules Using End-Hole Displacement.....	86
5.1 Introduction.....	86
5.2 Single Photonic Crystal L3 Cavity.....	87
5.3 Simulation Results of Photonic-Molecules.....	88
5.4 Theoretical Model Comparison	91
5.5 Dependence on Cavity Separations	95
5.6 Experimental Results.....	98
5.6.1 Sample Details	98
5.6.2 PL Characterization of Photonic-Molecules	99
5.7 Waveguide Induced Coupling Between Distant L3 Cavities.....	103
5.8 Summary.....	107
References.....	108
6 Waveguide-coupled Ring Resonators for On-Chip Spectral Filtering Applications.....	110
6.1 Introduction.....	110
6.2 Simulation and Design of Ring Resonators.....	111
6.2.1 WGMs Formation and Field Distribution in a Ring Resonator	111
6.2.2 Design of an All-Pass Filter using a Ring Resonator	113
6.2.3 Sample Details	115
6.3 Characterization of Waveguide-Coupled Ring Resonators.....	116
6.4 On-Chip Notch Filtering.....	123

6.5 Single QD Emission and its Purcell Enhancement.....	125
6.6 Add-Drop Filters using Ring Resonators.....	128
6.7 Summary.....	129
References.....	130
7 Conclusions and Outlooks.....	132
References.....	135

Chapter 1

Introduction

1.1 Outline and Scope of this Thesis

This thesis focusses on a number of quantum dots (QDs) and photonic cavities that are relevant to the potential building blocks for integrated quantum optical circuits.

It starts with a chapter that introduces the fabrication of QDs, general physical properties of QDs, basic concept of cavity quantum electrodynamics (cQED) and cavity-cavity interaction in III-V semiconductors.

Following the introduction chapter, Chapter 2 contains the details of the computational methods (Finite Difference Time Domain (FDTD) and Guided Mode Expansion (GME)) used to perform the simulations presented in subsequent chapters.

In Chapter 3, fabrication processes and experimental characterization methods of the photonic crystal L3 cavity and ring-resonator are presented in detail. The confocal spectroscopic setup used to characterize the nanohole-filled droplet epitaxial (NFDE) QDs is also introduced.

Chapter 4 presents the experimental investigations on electron and nuclear spin properties of nanohole-filled droplet epitaxial (NFDE) QDs grown by in situ etching and nanohole in-filling. Vanishing electron g factors ($g < 0.05$) and optical manipulation of the nuclear spin environment are demonstrated. The strain of QDs, revealed by nuclear

magnetic resonance (NMR) spectroscopy, is nearly three orders of magnitude smaller than in self-assembled dots.

Chapter 5 explores the cavity-cavity interaction in a photonic-molecule system by tuning the coupling strength and mode symmetry by end-hole displacement. Simulation results have been performed using FDTD and GME methods. A theoretical model has been built to calculate and explain the mode splitting and symmetry exchange. Experimental results have been carried out and are in good agreement with both simulation results and theoretical analysis.

Chapter 6 presents the application of whispering gallery mode (WGM) ring resonators on spectra filtering. The mode structure and transmission of waveguide-coupled micro ring resonators have been characterized using photoluminescence spectroscopy, revealing ultra-narrow notches filtering effect and Purcell enhancement of a single QD.

Chapter 7 provides a summary of all the chapters and a proposal for potential future work.

1.2 Growth of semiconductor quantum dots

Self-assembled quantum dots are used throughout the work presented in this thesis as they exhibit excellent atom-like optical properties and controllability, which makes them ideal candidates for quantum optics experiments. They can also be used as an internal light source when excited by an external laser or pumped electrically. In this section, the growth mechanism of QDs will be briefly discussed.

Growth approaches of semiconductor quantum dots have been studied since the end of the 1980s. The most popular and commonly used techniques for growth of high quality QDs are those based on self-assembly growth [1]. Particularly, the Stranski-Krastanow (SK) growth mode [2], a bottom-up approach, is an efficient mechanism to create nanostructures with a narrow bandgap and low defect density. The InAs QDs used in Chapter 5 and 6 are produced via molecular beam epitaxy (MBE) [3] based on the SK growth mechanism, during which crystalline layers of InAs are deposited on a GaAs substrate along the [100] plane. Due to the lattice-mismatch between the two

materials (~7%) and a critical thickness (about two monolayers) of the InAs, 3 dimensional (3D) islands form, as illustrated in Figure 1.1.

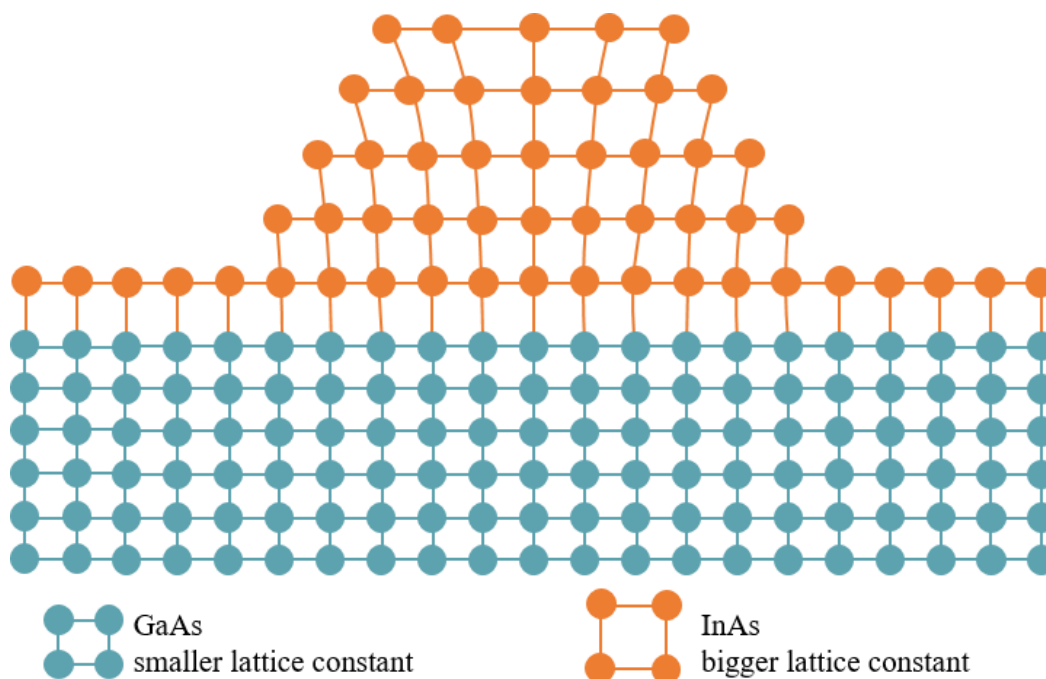


Figure 1.1: Illustration of the structure of an InAs/GaAs QD.

In addition to the SK growth mechanism, other approaches for QD fabrication, such as thickness fluctuations in quantum wells [4, 5], combination of SK growth and in situ etching [6-8], and droplet epitaxy [9-13] etc, open up the opportunity to produce advanced QDs with distinct properties (strong confinement, large optical efficiency, high spatial symmetry, and so on), which is not possible by the SK growth mode alone.

The experimental results presented in Chapter 4 are obtained on NFDE QDs formed by the droplet epitaxy technique. The NFDE QD sample is grown using solid source molecular beam epitaxy (MBE). As illustrated in the schematic picture of the fabrication processes (Figure 1.2), 11 monolayers of Ga are deposited on the GaAs (blue layer) buffer at 520 °C, forming Ga droplets (red dot) by lattice-mismatch. When the droplets are annealed under As flux, nanoholes with their edges exhibiting moundlike structures

along $[\bar{1}10]$ form due to As dissolution and Ga diffusion [6, 67]. A 7 nm of $\text{Al}_{0.44}\text{Ga}_{0.56}\text{As}$ layer (orange color) is then deposited on the top of nanoholes and form the bottom barrier. GaAs quantum dots are formed after the deposition of a 3.5 nm GaAs layer and a 112 nm $\text{Al}_{0.33}\text{Ga}_{0.67}\text{As}$ layer due to the bandgap of the surrounding material is greater than that of the QD material. The cap layer consists of GaAs with a thickness of 20 nm.

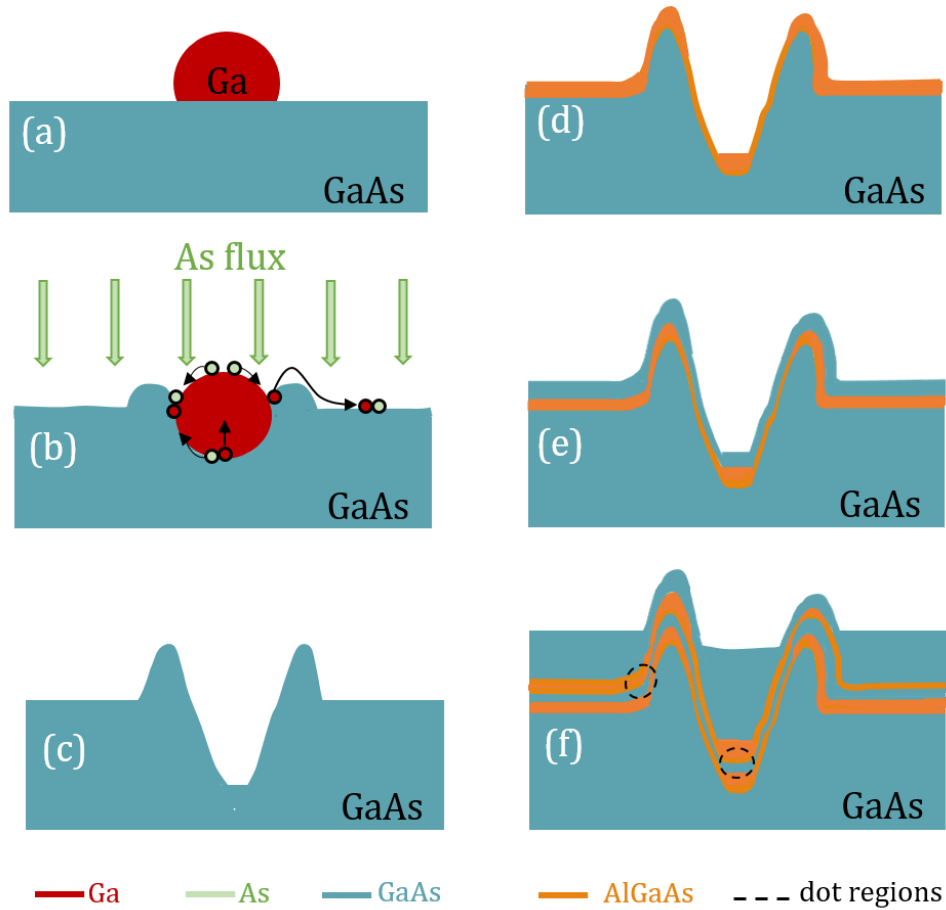


Figure 1.2: Schematic illustration of the nanohole-filled droplet epitaxy quantum dots formation (a)-(f). Blue colour is for GaAs. Red colour represents the Ga droplet. Green arrows indicate the As flux. Orange colour is the $\text{Al}_{0.44}\text{Ga}_{0.56}\text{As}$ layer. The dashed black circles indicate the dot regions, which are formed due to their unique strain properties and the narrowing of the neighboring QWs. A schematic cross-section structure of the studied QDs in this work is shown in (f), based on the reported AFM studies (see reference [22] in chapter 4).

1.3 Physical properties of self-assembled quantum dots

1.3.1 Density of States

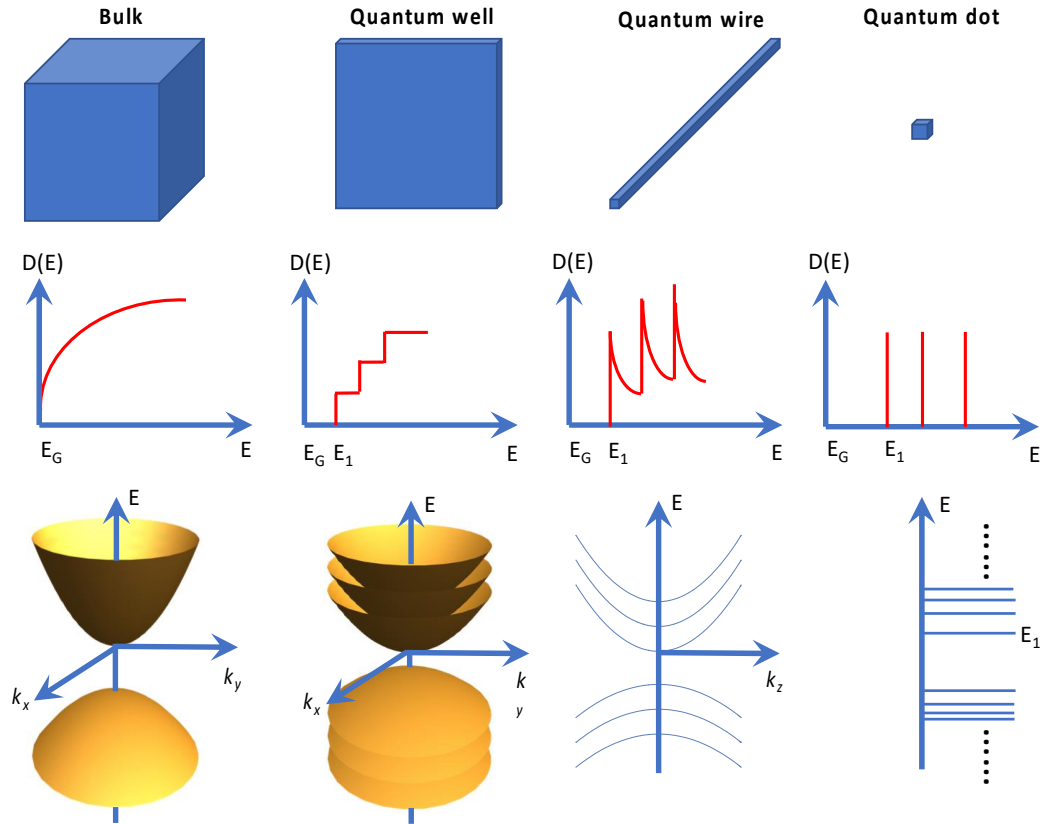


Figure 1.3: Comparison of the density of states $D(E)$ and band structures of bulk material, quantum wells, quantum wires and quantum dots.

Quantum wells, wires and dots are structures that confine particles with 1, 2 and 3 dimensional potential wells, respectively. As the length of confining dimensions becomes comparable to or smaller than the corresponding thermal wavelength, particles display quantum confinement behavior, which is characterized by the changes in the density of states. As illustrated in Figure 1.3, the density of states $D(E)$ of a semiconductor crystal changes when reducing its dimensionality from bulk to quantum dot. Since a quantum dot is a structure with 3D confinement, electrons in a quantum dot

occupy discrete energy levels, characterized by a series of delta-functions in the density of states $D(E)$. This discrete level structure resembles that of an atom, providing ideal candidates for implementing a qubit.

1.3.2 Band Structure

In this section, a brief introduction of the energy level structure of electrons (holes) confined in QDs is given. Generally, the electronic structure in momentum space (k -space) of a material changes from a continuous band structure (continuous dispersion) to discrete energy levels as dimensionality reduces from 3D to 0D, as illustrated at the bottom of Figure 1.3. In bulk III-V semiconductors such as InAs and GaAs, the conduction band originates from s orbitals of the constituent atoms [14] whilst the valence band has dominant p -like nature with a small hybridization of d orbitals [15]. Therefore, electrons in the conduction band of a III-V semiconductor have an s -like wavefunction with zero orbital angular momentum ($L = 0$). The total angular momentum $J=L+S$, where S is the spin angular momentum. For an electron, $|S| = S_e = 1/2$. As a result, the total angular momentum of the electron is $J = S_e = 1/2$. Two projections of the spin are possible along the z -axis ($m_{es,z} = \pm 1/2$) corresponding to the spin up and spin down ($|\uparrow\rangle$ and $|\downarrow\rangle$) state of the electron.

However, for holes in the valence band of a III-V semiconductor, the configuration of angular momentum is more complex. The dominant p -like wavefunction gives an orbital angular momentum for holes of $|L| = l_h = 1$ [110, 111]. Thus the eigenvalues of total angular momentum J are $|L-S|=1/2$ and $|L+S|=3/2$. These two eigenvalues give rise to two bands containing $J_z = \pm 1/2$ (for $J=1/2$) and $J_z = \pm 3/2, \pm 1/2$ (for $J=3/2$), respectively. The $J=1/2$ band corresponds to the low-lying energy band resulting from the spin-orbit splitting (Δ) which is around 0.1 to 0.5 eV for typical III-V semiconductors [16]. For the holes in the $J = 3/2$ band, those with $J_z = m_{hh,z} = \pm 3/2$ are heavy holes (HHs) whilst those with $J_z = m_{lh,z} = \pm 1/2$ are light holes (LHs). The HH and LH bands are degenerate at the Γ point of a bulk semiconductor (as schematically shown in Figure 1.4). However, this degeneracy is lifted when the symmetry of the system is broken (e.g. present of different quantum confinement energies and strain).

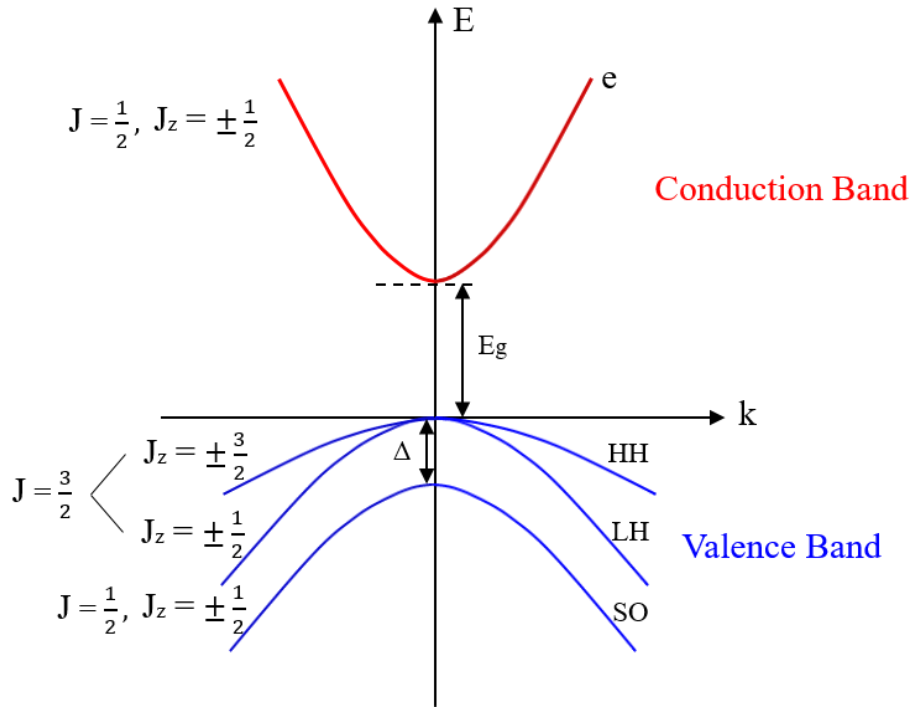


Figure 1.4: Illustration of the typical band structure of a III-V semiconductor. The conduction band (blue) contains a single band which is split from the valence band by the bandgap (E_g). The valence band (red) contains three bands, the Heavy Hole (HH), Light Hole (LH) and Split-Off (SO) bands. The SO band is split from the other bands by the spin-orbit splitting (Δ). At $k = 0$ (Γ point) the HH and LH bands are degenerate however they split with increasing k .

As mentioned above, carriers in a QD occupy discrete energy levels due to the 3 dimensional quantum confinement. Taking an InGaAs QD as an example, the band gap of InGaAs is smaller than that of GaAs. This leads to 3D quantum confinement and thus the discrete density of states and atomic energy levels illustrated in Figure 1.3. For a QD prepared using SK growth technique, the confinement potential may be well approximated by a parabolic confinement potential. This results in a 2D-harmonic-oscillator-like energy spectrum for the QD [17–19], as schematically shown in Figure 1.5. The height of a SK growth QD is generally much smaller than the diameter of their base

leading to stronger confinement of carriers along the vertical axis. As a result, the in-plane orbital structure with circularly symmetric harmonic wavefunctions [19, 20] resembles the spherically symmetrical orbitals found in atomic physics (s , p , d , f ...) (although shells don't have the same angular momentum), and thus the electronic levels in a SK QD are denoted using s , p , d , f ... (see Figure 1.5). In symmetric dots, selection rules only allow valence band electrons to be excited to the conduction band shell with the same label (excluding a weakly allowed $s \rightarrow d$ transition) [20, 21]. In asymmetric QDs, this selection rule may be eased due to shell mixing [20, 21].

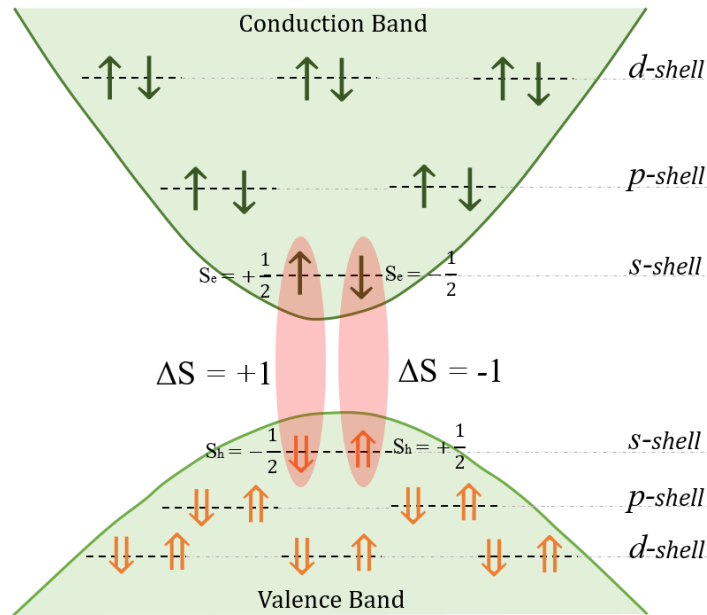


Figure 1.5: Discrete electronic structure of a QD with s , p , and d shells occupied by carriers. Electron spin up and down are labeled as \uparrow and \downarrow , respectively. The spin up and down states of holes are denoted by \uparrow and \downarrow , respectively. Each shell may contain more than one pair of electron and hole with opposite spins. The energy spacing of the conduction band shells is significantly larger than those in the valence band for typical InGaAs self-assembled QDs [22]. The difference of electron spin ($S_e = \pm \frac{1}{2}$) and hole spin ($S_h = \mp \frac{1}{2}$) is $\Delta S = \pm 1$ for the s -shell bright exciton states, highlighted in red regions. The LH and SO bands are ignored for the purposes of this figure.

1.3.3 Bright Excitons and Dark Excitons

In semiconductors, an exciton is a hydrogen-like quasiparticle consisting of a bound pair of an electron and a hole. It releases its energy via electron-hole recombination, governed by the selection rules. During a radiative recombination transition process of an exciton, the difference of the spins between the electron and hole in the exciton must be ± 1 . The exciton with electron spin and hole spin satisfying the optical selection rules is called a bright exciton, which emits a photon when it recombines. When the electron spin and hole spin of an exciton are unable to satisfy the selection rules, the direct recombination of exciton is forbidden; as a result, no photon emission can be observed. This type of exciton is referred to as the dark exciton (optically forbidden exciton) and usually has a long lifetime. In a QD, bright and dark excitons can be formed due to the Coulomb interaction and the different electron-hole spin combination. As illustrated in Figure 1.5, bright exciton states ($\Delta S = \pm 1$, highlighted in red region) have opposite electron/hole spins. However, dark excitons ($\Delta S = \pm 2$) correspond to electron-hole pairs with the same spins. In QDs, the exchange interaction may couple the bright and dark states [23], resulting in an increase of the oscillator strength for the dark exciton, which can be observed in photoluminescence spectra [23-25]. In Chapter 3, dark and bright excitons will be discussed with reference to experimental results.

1.3.4 Hyperfine Interactions

For a typical InGaAs QD prepared by the SK growth technique, the QD itself comprises $\sim 10^6$ nuclei. The nuclear spin bath, which is usually described by an effective magnetic fields known as the Overhauser field, interacts with the carriers in the QD via the hyperfine interaction [26-28]. In turn, a single nuclear spin also experiences a hyperfine interaction from the confined carrier with the corresponding effective field known as the Knight field [27-29].

The average magnitude of the random Overhauser field in a typical InGaAs QDs has been found to be around 30 mT [30-32] at zero external magnetic field. This effective magnetic field fluctuates in time with a measured standard deviation of 14 mT [31]. Since the fluctuation time of the Overhauser field is usually much longer than the

lifetime of the carriers [30], it can be considered as a quasi-static field during the carrier lifetime [33]. However, when repeating a measurement, the carriers in a QD experience different magnetic fields and hence different precession frequencies each time, resulting in dephasing [34]. The time-dependent Overhauser field also induces the emission linewidth broadening for QDs if the measurement is slow relative to the nuclear spin dynamics [30, 35].

1.4 Quantum Dots in Magnetic Fields

When applying a magnetic field \mathbf{B} to a quantum dot, magnetic field induced level splitting due to the opposite signs of m_j for the two s -shell electrons and holes occurs. The splitting is determined by

$$E_Z^i = g^i \mu_B B \quad (1.1)$$

with g^i being the Landé g -factor for the carrier or exciton denoted by the index i ($e \rightarrow$ electron, $h \rightarrow$ hole, $X \rightarrow$ neutral exciton) and μ_B being the Bohr magneton. As the value of g^i contains a factor of m_j , the measured hole g -factor evaluated according to the Zeeman splitting includes an additional factor of 3 compared to the electron, allowing the hole ($m_j = \pm 3/2$) to be regarded as having a pseudospin of $\pm 1/2$. Since the exciton is a quasi-particle of combined electron and hole, its g -factor is defined as $g^X = g^h - g^e$. In addition to Zeeman effect, a quadratic diamagnetic shift is also observed for the neutral exciton [36–39]. This effect shifts the exciton luminescence to higher energy in magnetic field irrespective of spin. Hence the total energy shift of an exciton in a magnetic field may be described by

$$\Delta E = \gamma_1 B + \gamma_2 B^2 \quad (1.2)$$

with γ_2 being the diamagnetic coefficient and $\gamma_1 = S_z g^X \mu_B / 2$.

1.5 Quantum dot-cavities interaction

1.5.1 Typical Cavities

In recent decades, various optical microcavities that can couple to QDs have been developed. As the exciton emission from MBE-grown QDs is generally sharp, optical cavities with small mode volume and high quality factor are needed for achieving efficient QD-cavity coupling. Photonic Crystal Cavities (PCCs) are one type of ideal candidates to satisfy these crucial condition of coupling. Artificial PCCs are fabricated by patterning a periodic structure from two materials with different refractive index. This creates a structure analogous to a crystalline lattice for electrons, resulting in a photonic band structure for light similar to the electronic band structure of semiconductors. The destructive interference of light due to the periodic refractive index difference results in a gap opening in the photonic band structure. By manipulating the periodicity, the photonic band gap may be tuned. Similar to the localized electronic states induced by a defect in crystalline lattices, when a defect is introduced into the photonic crystal, the propagation of photons with energies falling within the band gap will be heavily suppressed, forming localized optical cavity modes in the defect region.

In the III-V semiconductors used in this work, PCCs are formed by EBL etching of air holes in the semiconductor material. As this method only produces a 2D PCC, the sample beneath the cavity is also etched away to produce an air-clad slab with confinement in this axis arising from total internal reflection (TIR) at the slab-air interfaces. Two common types of PCCs are illustrated in Figure 1.6 ((a) and (b)), known as H1 and L3 cavities, where 1 and 3 holes are respectively omitted from a PhC slab. One of the advantages of photonic crystal structures is that it is relatively easy to engineer in-plane emission for optical circuit devices.

Micro-ring (Figure 1.6(c)) and Micro-disk (Figure 1.6(d)) cavities are formed from a ring (and a disk) of etched semiconductor attached to the wafer by a thin pedestal. Optical confinement is provided by TIR in all three directions, resulting in Whispering Gallery Modes (WGMs) with high quality factor. A drawback of micro-ring and micro-disk cavities is that the emission direction is not well-defined, this may be overcome by fabricating waveguides close to the disk but at the cost of reduced Q-factor.

Micropillar cavities shown in Figure 1.6(e) are fabricated by etching the wafer with Distributed Bragg Reflector (DBR) mirror [40] layers into micro-cylinders protruding

from the sample with TIR providing 2D confinement. The DBR mirror layers provide the final dimension of confinement. Similar to that of a Vertical Cavity Surface Emitting Laser (VCSEL) device [41], the emission of the micropillar is well-defined along the pillar axis which allows efficient optical pumping and collection. However, this can be easily applied to a circuit device where in-plane emission is required.

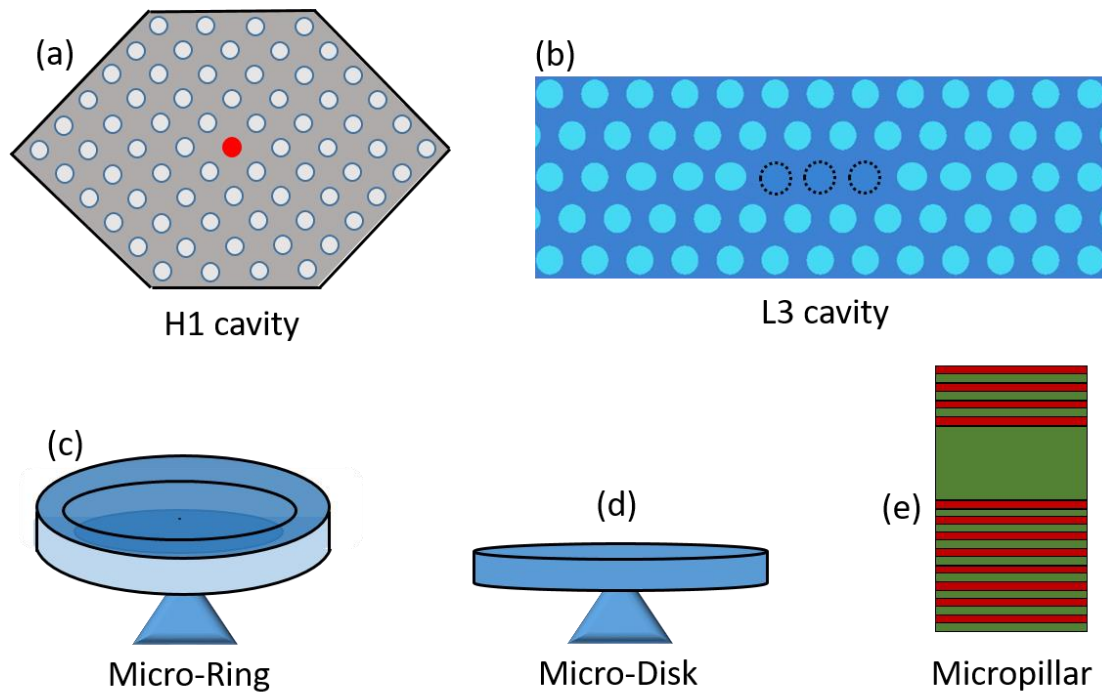


Figure 1.6: Schematics of the main types of optical microcavity. The H1 (a) and L3 PCCs (b) comprise a suspended membrane surrounded by air. The H1 PCC (a) is formed by omitting a single air hole from the lattice. For the L3 PCCs (b), three air holes in a line are omitted. The micro-ring and micro-disk cavity (c and d) consist of an etched ring (disk) of semiconductor supported by a thin pedestal. A micropillar cavity (e) comprises a cylindrical pillar with DBR layers at the top and bottom.

1.5.2 Quality Factor of Cavity

One of the most important parameters characterizing an optical microcavity is the quality factor Q . It is a crucial parameter for achieving both Purcell enhancement and strong exciton-photon coupling. The Q factor is defined as the inverse loss rate from the cavity, and can be expressed as

$$Q = \lambda/\Delta\lambda \quad (1.3)$$

or

$$Q = \omega/\Delta\omega, \quad (1.4)$$

where λ and ω are the resonant wavelength and the angular resonant frequency, respectively; $\Delta\lambda$ and $\Delta\omega$ are the full width at half maximum (FWHM). Due to the limitation of calculating $\Delta\lambda$ or $\Delta\omega$, it is unfeasible to use Eq. (1.3) or (1.4) for high Q calculations. Based on the definition of Q factor, another common expression for Q can be written as

$$Q = \omega \left(\frac{\text{energy stored}}{\text{power loss}} \right), \quad (1.5)$$

where ω is the angular frequency when the stored energy and power loss are measured. The definitions are equivalent in the high Q limit, a regime in which Q may be considered approximately equal to the number of oscillations required for the system's energy to drop to $e^{-2\pi}$ of its former energy without further excitation [42].

An exponentially decaying intensity $I(t) = I(0) e^{-t/\tau}$ corresponds to an amplitude $A(t) = A(0) e^{-t/2\tau}$. Fourier transforming $A(t)$ yields a Lorentzian line shape [43]:

$$L(\omega) = \frac{\tau^{-1}}{2\pi} \frac{1}{(\omega - \omega_0)^2 + (\tau^{-1}/2)^2} \quad (1.6)$$

It is then clear that the full width at half maximum $\Delta\omega = \tau^{-1}$, and thus

$$Q = \omega\tau = \omega\kappa \quad (1.7)$$

with $\kappa = \frac{1}{\tau_{cav}}$ (τ_{cav} is the cavity photon lifetime) being the photon decay rate. Table 1 shows typical values of the mode volume (V_m) and Q factor for five of the most common types of semiconductor optical microcavity. The parameter Q/V_m is also calculated as this represents a figure of merit for the strength of interaction between a cavity and a QD (see Section 1.5.3). As can be seen in Table 1, the PhC cavities have significantly

smaller mode volume. This allows them to couple to the QD with a much stronger coupling strength (see Section 1.5.3). This, together with the in-plane geometry makes PCCs the most attractive cavities for the circuit architecture.

Type	$V_m(\lambda/n)^3$	Q	$Q/V_m(\lambda/n)^3$
H ₁ PhC	0.39 [64]	17,000 [64]	44,000
L ₃ PhC	~1 [63]	25,000 [63]	25,000
Microdisk WGM	8 [65]	12,000 [65]	1,500
Micropillar DBR	16 [66]	12,000 [66]	750

Table 1: Table of state-of-the-art mode volumes (V_m) and Q-factors for a number of common semiconductor optical microcavity implementations [44].

1.5.3 Basic Concept of Cavity QED

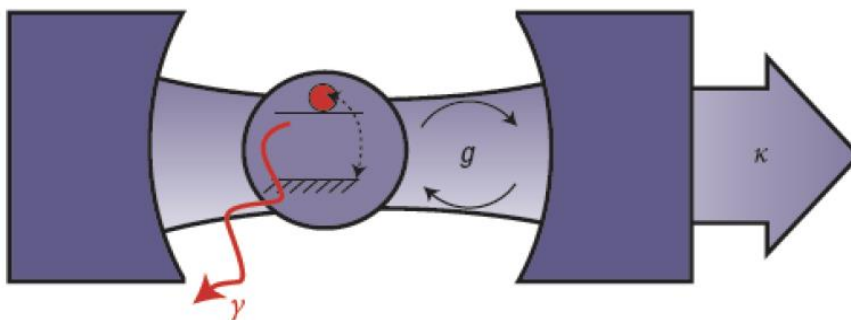


Figure 1.7: Schematic picture of a coupled cavity-QD system. The system is characterized by parameters g , κ and γ . Coupling strength between the cavity photons and the QD is described by g . The rate of leakage from the cavity mode is represented by κ , and γ is a rate incorporating both decay and dephasing of the QD state.

Cavity Quantum Electrodynamics (cQED) is the research field focusing on the interactions between a quantum emitter and an optical cavity. The light-matter interaction is enhanced when a quantum emitter is placed in the light field, confined in an optical cavity. Over the past decades, cQED has been widely studied, and important predictions of quantum optics have been experimentally verified using atom-cavity coupling system [45]. As a solid state implementation of cQED, in the semiconductor QD-cavity coupling systems, microcavities fabricated using lithographic technique can be far smaller than those used in atomic experiments, allowing them to be easily incorporated onto a single chip.

Furthermore, useful effects such as brighter and more indistinguishable single photon sources, enhancement of weaker emission channels such as LA phonon-assisted emission [46-49] and ultrafast optical switching [50-52], have been developed using semiconductor QD-microcavity coupling systems [53, 54]. In this section the basic concepts of cQED are given.

For a coupled QD-cavity system, two parameters of the optical cavity define the performance coupling system [230]. The first one is the Q factor discussed in Section 1.5.2. The second one is the mode volume V_m which is defined by Eq (1.8) [55, 56]:

$$V_m = \frac{\int d^3r \epsilon(r) |E(r)|^2}{\max\{\epsilon(r) |E(r)|^2\}} \quad (1.8)$$

Here ϵ is the relative permittivity and E is the amplitude of the electric field.

With these two parameters, the coherent coupling strength g of the QD-cavity system is then given by Eq (1.9):

$$g = \frac{1}{\hbar} \sqrt{\frac{\hbar \omega}{2V_m}} \mu \quad (1.9)$$

where μ is the dipole moment of the QD and it is assumed that the QD is placed at the maximum of the light field $\epsilon(r) |E(r)|^2$. These parameters are illustrated in Figure 1.7. According to the coupling strength, different operation regimes of the cQED system can be defined.

In the weak coupling regime of a QD-cavity coupling system, the incoherent decay processes, such as cavity losses (κ) or QD decay and dephasing (γ), are dominant. Hence the definition of weak coupling is:

$$g \ll \kappa, \gamma \quad (1.10)$$

In this regime, the Purcell effect [55], where the spontaneous emission rate is either enhanced or suppressed by the cavity depending on the cavity-QD detuning, is expected. This phenomenon is well-observed in QD-cavity systems [57–59] and has been widely used in developing highly efficient single [60] and entangled [61] photon sources. If the cavity is resonant with a QD in the center of the cavity mode, the Purcell factor (F_p) can be defined as:

$$F_p = \frac{3}{4\pi^2} \left(\frac{\lambda_c}{n}\right)^3 \left(\frac{Q}{V_m}\right) \quad (1.11)$$

where λ_c is the cavity wavelength and n is the refractive index of the cavity material.

In the strong coupling regime of a QD-cavity coupling system, the coherent interaction between the QD and the cavity field is dominant:

$$g \gg \kappa, \gamma \quad (1.12)$$

In this regime of coupling, vacuum Rabi oscillations [62] in the time domain with population coherently oscillating between the QD and the cavity field can be observed. In the frequency domain this is characterized by the splitting of peaks corresponding to hybrid light-matter states (polariton states) with a splitting of $\Omega_R = 2g$. The figure of merit for a strongly coupled system is the ratio $Q/\sqrt{V_m}$. Higher quality factor Q reduces the cavity loss rate κ and smaller mode volumes (V_m) increase the coupling strength g .

1.5.4 Inter-Cavity Coupling

As discussed in the previous sections, photonic crystal cavities are the preferential choices for the cQED systems in a circuit-style optical chip due to their high Q factor, small mode volume and nanofabrication compatibility. Furthermore, complex structures such as arrays of photonic crystal cavities can also be achieved. If quantum

dots are placed at/close to cavity centres, the coupling between the cavities might allow them to form building blocks for a scalable quantum photonic network. In this section, the photonic aspect of inter-cavity coupling of two L3 PCCs is briefly discussed (see Chapter 5 for detailed simulation and experimental results).

When two or more PCCs on the same membrane are separated by air holes while in close proximity to each other, they couple to each other. The air holes act as a potential barrier and the eigen modes of the coupled system replace the individual modes of each cavity. Here, in the configuration of a dual cavity system, the resultant eigensolutions are the odd and even combinations of the individual cavity mode. The system behaves as a two-level system described by a matrix Hamiltonian

$$H = \begin{pmatrix} E_1 & J \\ J^* & E_2 \end{pmatrix} \quad (1.13)$$

Where J represents the coupling strength, depending on barrier width and height. The eigen values of the coupled system are:

$$E_{\pm} = \frac{1}{2} \left\{ (E_1 + E_2) \pm \sqrt{(E_1 - E_2)^2 + 4|J|^2} \right\} \quad (1.14)$$

indicating an on resonance splitting of $2|J|$.

When two PCCs are far apart, their coupling can be induced through a waveguide that couples to both cavities (cavity A and cavity B) in the system, as discussed in Section 5.8. In this configuration, the Hamiltonian of the system can be written as:

$$H = \begin{pmatrix} \omega_c & 0 & \sigma_1 & \sigma_2 & \cdots \\ 0 & \omega_c & \Delta_1 & \Delta_2 & \cdots \\ \sigma_1^* & \Delta_1^* & \omega_1 & 0 & \cdots \\ \sigma_2^* & \Delta_2^* & 0 & \omega_2 & \cdots \\ \vdots & \vdots & \vdots & \vdots & \ddots \end{pmatrix}, \quad (1.15)$$

where ω_c is the frequency of cavity mode, ω_1 is the frequency of FP mode (labeled as Mode 1) in waveguide, ω_2 is the frequency of FP mode (labeled as Mode 2) in waveguide. σ_1 and σ_2 indicate that cavity A interacts with Mode 1 and Mode 2, respectively. Δ_1 (Δ_2) is generated by the interaction between cavity B and Mode 1 (Mode 2).

The solutions for the inter-cavity coupling system are:

$$(\omega_c + \sum_i \frac{|\sigma_i|^2}{\omega - \omega_i})\phi_A + \sum_i \frac{\sigma_i \Delta_i^*}{\omega - \omega_i} \phi_B = \omega \phi_A, \quad (1.16)$$

$$(\omega_c + \sum_i \frac{|\sigma_i|^2}{\omega - \omega_i})\phi_B + \sum_i \frac{\sigma_i^* \Delta_i}{\omega - \omega_i} \phi_A = \omega \phi_B, \quad (1.17)$$

where ϕ_A (ϕ_B) is the amplitude in cavity A (B). $\sum_i \frac{|\sigma_i|^2}{\omega - \omega_i}$ is the self-energy term which shifts and broadens the cavity energy. $\sum_i \frac{\sigma_i \Delta_i^*}{\omega - \omega_i}$ and $\sum_i \frac{\sigma_i^* \Delta_i}{\omega - \omega_i}$ are the coupling terms.

- [1] B. J. Riel, 'An introduction to self-assembled quantum dots', *Am. J. Phys.* 76, 7507 (2008).
- [2] J. Venables, *Introduction to Surface and Thin Film Processes*, Cambridge University Press, ISBN 0-521-62460-6 (2000).
- [3] A. Cho (ed.), *Molecular Beam Epitaxy*, Springer, Berlin (1997).
- [4] K. Brunner, G. Abstreiter, G. Bohm, G. Trankle, G. Weimann, 'Sharp-Line Photoluminescence and Two-Photon Absorption of Zero-Dimensional Biexcitons in a GaAs/AlGaAs Structure', *Phys. Rev. Lett.* 73, 1138 (1994).
- [5] A. Zrenner, L. V. Butov, M. Hagn, G. Abstreiter, G. Bohm, G. Weimann, 'Quantum dots formed by interface fluctuations in AlAs/GaAs coupled quantum well structures', *Phys. Rev. Lett.* 72, 3382 (1994).
- [6] T. Kaneko, P. Smilauer, B. A. Joyce, T. Kawamura, D. D. Vvedensky, 'Reentrant Layer-by-Layer Etching of GaAs (001)', *Phys. Rev. Lett.* 74, 3289 (1995).
- [7] H. Schuler, T. Kaneko, M. Lipinski, K. Eberl, 'In situ etching with AsBr_3 and regrowth in molecular beam epitaxy', *Semicond. Sci. Technol.* 15, 169 (2000).
- [8] H. Schuler, N. Y. Jin-Phillipp, F. Phillipp, K. Eberl, 'Size modification of self-assembled InAs quantum dots by in situ etching', *Semicond. Sci. Technol.* 13, 1341 (1998).
- [9] C. D. Lee, C. Park, H. Lee, K. S. Lee, S. J. Parl, S. Noh, N. Koguchi, 'Fabrication of Self-Assembled GaAs/AlGaAs Quantum Dots by Low-Temperature Droplet Epitaxy', *Jpn. J. Appl. Phys.* 37, 7158 (1998).
- [10] K. Watanabe, N. Koguchi, Y. Gotoh, *Jpn. J. Appl. Phys.* 39, 79 (2000).
- [11] T. Mano, K. Watanabe, S. Tsukamoto, N. Koguchi, H. Fujioka, M. Oshima, C. D. Lee, J. Y. Leem, H. J. Lee, S. K. Noh, 'Nanoscale InGaAs concave disks fabricated by heterogeneous droplet epitaxy', *Appl. Phys. Lett.* 76, 3543 (2000).
- [12] M. Yamagiwa, T. Mano, T. Kuroda, T. Tateno, K. Sakoda, G. Kido, N. Koguchi, F. Minami, 'Self-assembly of laterally aligned GaAs quantum dot pairs', *Appl. Phys. Lett.* 89, 113115 (2006).

- [13] C. Heyn, A. Stemmann, A. Schramm, H. Welsh, W. Hansen, A. Nemcsics, 'Regimes of GaAs quantum dot self-assembly by droplet epitaxy', *Phys. Rev. B* 76, 075317 (2007).
- [14] A. Fox, *Optical Properties of Solids*, Oxford master series in condensed matter physics, Oxford University Press (2001).
- [15] E. A. Chekhovich, M. M. Glazov, A. B. Krysa, M. Hopkinson, P. Senellart, A. Lemaitre, M. S. Skolnick, and A. I. Tartakovskii, 'Element-sensitive measurement of the hole-nuclear spin interaction in quantum dots', *Nat. Phys.* 9, 74 (2013).
- [16] S. Economou and T. Reinecke, 'Optical Generation and Control of Quantum Coherence in Semiconductor Nanostructures', *NanoScience and Technology* (ed. By G. Slavcheva and P. Roussignol), Springer, Berlin, 63 (2010).
- [17] W. Que, 'Excitons in quantum dots with parabolic confinement', *Phys. Rev. B* 45, 11036 (1992).
- [18] A. Wojs, P. Hawrylak, S. Fafard, and L. Jacak, 'Electronic structure and magneto-optics of self-assembled quantum dots', *Phys. Rev. B* 54, 5604 (1996).
- [19] S. Tarucha, D. G. Austing, T. Honda, R. J. van der Hage, and L. P. Kouwenhoven, 'Shell Filling and Spin Effects in a Few Electron Quantum Dot', *Phys. Rev. Lett.* 77, 3613 (1996).
- [20] P. Hawrylak and M. Korkusinski, 'Single Quantum Dots: Fundamentals, Applications and New Concepts' In *Topics in Applied Physics* (ed. by P. Michler). Springer, Chap. Electronic Properties of Self-Assembled Quantum Dots, pp. 25–91 (2004).
- [21] P. Hawrylak, G. A. Narvaez, M. Bayer, and A. Forchel, 'Excitonic Absorption in a Quantum Dot', *Phys. Rev. Lett.* 85, 389 (2000).
- [22] P. Petroff, 'Single Quantum Dots: Fundamentals, Applications and New Concepts.' In *Topics in Applied Physics 2* (ed. by P. Michler). Springer, Chap. Epitaxial Growth and Electronic Structure of Self-Assembled Quantum Dots, pp. 1–24 (2004).
- [23] M. Bayer, G. Ortner, O. Stern, A. Kuther, A. A. Gorbunov, A. Forchel, P. Hawrylak, S. Fafard, K. Hinzer, T. L. Reinecke, S. N. Walck, J. P. Reithmaier, F. Klopff, and F. Schafer,

- 'Fine structure of neutral and charged excitons in self-assembled In(Ga)As/(Al)GaAs quantum dots', Phys. Rev. B 65, 195315 (2002).
- [24] J. Puebla, E. A. Chekhovich, M. Hopkinson, P. Senellart, A. Lemaitre, M. S. Skolnick and A. I. Tartakovskii, 'Dynamic nuclear polarization in InGaAs/GaAs and GaAs/AlGaAs quantum dots under nonresonant ultralow-power optical excitation', Phys. Rev. B 88, 045306 (2013).
- [25] E. A. Chekhovich, M. N. Makhonin, J. Skiba-Szymanska, A. B. Krysa, V. D. Kulakovskii, M. S. Skolnick, and A. I. Tartakovskii, 'Dynamics of optically induced nuclear spin polarization in individual InP/Ga_xIn_{1-x}P quantum dots', Phys. Rev. B 81, 245308 (2010).
- [26] I. A. Merkulov, A. L. Efros, and M. Rosen. 'Electron spin relaxation by nuclei in semiconductor quantum dots', Phys. Rev. B 65, 205309 (2002).
- [27] A. Abragam, The Principles of Nuclear Magnetism. International series of monographs on physics, Clarendon Press (1961).
- [28] F. Meier and B. Zakharchenya, 'Optical Orientation', Modern Problems in Condensed Matter Sciences. Elsevier Science (1984).
- [29] C. W. Lai, P. Maletinsky, A. Badolato, and A. Imamoglu, 'Knight-Field-Enabled Nuclear Spin Polarization in Single Quantum Dots', Phys. Rev. Lett. 96, 167403 (2006).
- [30] A. V. Kuhlmann, J. Houel, A. Ludwig, L. Greuter, D. Reuter, A. D. Wieck, M. Poggio, and R. J. Warburton, 'Charge noise and spin noise in a semiconductor quantum device', Nat. Phys. 9, 570 (2013).
- [31] R. N. E. Malein, T. S. Santana, J. M. Zajac, A. C. Dada, E. M. Gauger, P. M. Petroff, J. Y. Lim, J. D. Song, and B. D. Gerardot, 'Screening Nuclear Field Fluctuations in Quantum Dots for Indistinguishable Photon Generation', Phys. Rev. Lett. 116, 257401 (2016).
- [32] R. Stockill, C. Le Gall, C. Matthiesen, L. Huthmacher, E. Clarke, M. Hugues, and M. Atatüre, 'Intrinsic limit to electron spin coherence in InGaAs quantum dots featuring strain-induced nuclear dispersion', ArXiv e-prints (Dec. 2015).

- [33] J. Hansom, C. H. H. Schulte, C. Le Gall, C. Matthiesen, E. Clarke, M. Hugues, J. M. Taylor, and M. Atature, 'Environment-assisted quantum control of a solid-state spin via coherent dark states', *Nat. Phys.* 10, 725 (2014).
- [34] D. Press, K. De Greve, P. L. McMahon, T. D. Ladd, B. Friess, C. Schneider, M. Kamp, S. Hofling, A. Forchel, and Y. Yamamoto, 'Ultrafast optical spin echo in a single quantum dot', *Nat. Photon.* 4, 367 (2010).
- [35] A. V. Kuhlmann, J. H. Prechtel, J. Houel, A. Ludwig, D. Reuter, A. D. Wieck, and R. J. Warburton, 'Transform-limited single photons from a single quantum dot', *Nat. Commun.* 6, 8204 (2015).
- [36] S. N. Walck and T. L. Reinecke, 'Exciton diamagnetic shift in semiconductor nanostructures', *Phys. Rev. B* 57, 9088 (1998).
- [37] M. Bayer, S. N. Walck, T. L. Reinecke, and A. Forchel, 'Exciton binding energies and diamagnetic shifts in semiconductor quantum wires and quantum dots', *Phys. Rev. B* 57, 6584 (1998).
- [38] M. Bayer, A. Kuther, A. Forchel, A. Gorbunov, V. B. Timofeev, F. Schäfer, J. P. Reithmaier, T. L. Reinecke, and S. N. Walck, 'Electron and Hole g Factors and Exchange Interaction from Studies of the Exciton Fine Structure in $\text{In}_{0.60}\text{Ga}_{0.40}\text{As}$ Quantum Dots', *Phys. Rev. Lett.* 82, 1748 (1999).
- [39] A. Kuther, M. Bayer, A. Forchel, A. Gorbunov, V. B. Timofeev, F. Schäfer, and J. P. Reithmaier, 'Zeeman splitting of excitons and biexcitons in single $\text{In}_{0.60}\text{Ga}_{0.40}\text{As}/\text{GaAs}$ self-assembled quantum dots', *Phys. Rev. B* 58, R75089 (1998).
- [40] Rudiger Paschotta 'Bragg Mirrors', *Encyclopedia of Laser Physics and Technology*, RP Photonics, retrieved May 1 (2009).
- [41] Kenichi Iga, 'Surface-emitting laser—Its birth and generation of new optoelectronics field', *IEEE Journal of Selected Topics in Quantum Electronics.* 6, 1201 (2000).
- [42] S.G. Johnson and J.D. Joannopoulos, *Photonic Crystals: The Road from Theory to Practice*, Kluwer Academic Publishers (2002).
- [43] A.M. Fox, *Quantum Optics*, Oxford University Press, 1st edition (2006).

- [44] A. Brash, Thesis: Ultrafast Dynamics of Single Quantum Dots, Page 48 (2016).
- [45] S. Haroche, 'Nobel Lecture: Controlling photons in a box and exploring the quantum to classical boundary', *Rev. Mod. Phys.* 85, 1083 (2013).
- [46] K. Hennessy, A. Badolato, M. Winger, D. Gerace, M. Atature, S. Gulde, S. Falt, E. L. Hu, and A. Imamoglu, 'Quantum nature of a strongly coupled single quantum dot-cavity system', *Nature* 445, 896 (2007).
- [47] K. H. Madsen, S. Ates, J. Liu, A. Javadi, S. M. Albrecht, I. Yeo, S. Stobbe, and P. Lodahl, 'Efficient out-coupling of high-purity single photons from a coherent quantum dot in a photonic crystal cavity', *Phys. Rev. B* 90, 155303 (2014).
- [48] S. M. Ates, S. Ulrich, A. Ulhaq, S. Reitzenstein, A. Löffler, S. Höfling, F. A., and P. Michler, 'Non-resonant dot-cavity coupling and its potential for resonant single quantum-dot spectroscopy', *Nat. Photon.* 3, 724 (2009).
- [49] S. L. Portalupi, G. Hornecker, V. Giesz, T. Grange, A. Lemaitre, J. Demory, I. Sagnes, N. D. Lanzillotti-Kimura, L. Lanco, A. Auffeves, and P. Senellart, 'Bright Phonon Tuned Single-Photon Source', *Nano Letters* 15, 6290 (2015).
- [50] R. Bose, D. Sridharan, H. Kim, G. S. Solomon, and E. Waks, 'Low-Photon-Number Optical Switching with a Single Quantum Dot Coupled to a Photonic Crystal Cavity', *Phys. Rev. Lett.* 108, 227402 (2012).
- [51] D. Englund, A. Majumdar, M. Bajcsy, A. Faraon, P. Petroff, and J. Vuckovic, 'Ultrafast Photon-Photon Interaction in a Strongly Coupled Quantum Dot-Cavity System', *Phys. Rev. Lett.* 108, 093604 (2012).
- [52] T. Volz, A. Reinhard, M. Winger, A. Badolato, K. J. Hennessy, E. L. Hu, and A. Imamoglu, 'Ultrafast all-optical switching by single photons', *Nat. Photon.* 6, 605 (2012).
- [53] X. Ding, Y. He, Z.-C. Duan, N. Gregersen, M.-C. Chen, S. Unsleber, S. Maier, C. Schneider, M. Kamp, S. Höfling, C.-Y. Lu, and J.-W. Pan, 'On-Demand Single Photons with High Extraction Efficiency and Near-Unity Indistinguishability from a Resonantly Driven Quantum Dot in a Micropillar', *Phys. Rev. Lett.* 116, 020401 (2016).

- [54] N. Somaschi, V. Giesz, L. De Santis, J. C. Loredó, M. P. Almeida, G. Hornecker, L. Portalupi, T. Grange, C. Antón, J. Demory, C. Gómez, I. Sagnes, N. D. Lanzillotti-Kimura, A. Lemaître, A. Auffeves, A. G. White, L. Lanco, and P. Senellart, 'Near-optimal single-photon sources in the solid state', *Nat. Photon.* 10, 340 (2016).
- [55] E. M. Purcell, 'Proceedings of the American Physical Society', *Phys. Rev.* 69, 681 (1946).
- [56] R. Coccioli, M. Boroditsky, K. W. Kim, Y. Rahmat-Samii, and E. Yablonovitch, 'Smallest possible electromagnetic mode volume in a dielectric cavity', *Optoelectronics, IEE Proceedings* 145.6 (1998).
- [57] P. Lodahl, A. Floris van Driel, I. S. Nikolaev, A. Irman, K. Overgaag, D. Vanmaekelbergh, and W. L. Vos, 'Controlling the dynamics of spontaneous emission from quantum dots by photonic crystals', *Nature* 430, 654 (2004).
- [58] D. Englund, D. Fattal, E. Waks, G. Solomon, B. Zhang, T. Nakaoka, Y. Arakawa, Y. Yamamoto, and J. Vuckovic. 'Controlling the Spontaneous Emission Rate of Single Quantum Dots in a Two-Dimensional Photonic Crystal', *Phys. Rev. Lett.* 95, 013904 (2005).
- [59] A. Kress, F. Hofbauer, N. Reinelt, M. Kaniber, H. J. Krenner, R. Meyer, G. Böhm, and J. J. Finley, 'Manipulation of the spontaneous emission dynamics of quantum dots in twodimensional photonic crystals', *Phys. Rev. B* 71, 241304 (2005).
- [60] A. Zrenner, E. Beham, S. Stufler, F. Findeis, M. Bichler, and G. Abstreiter, 'Coherent properties of a two-level system based on a quantum-dot photodiode', *Nature* 418, 612 (2002).
- [61] A. Dousse, J. Suffczynski, A. Beveratos, O. Krebs, A. Lemaître, I. Sagnes, J. Bloch, P. Voisin, and P. Senellart. 'Ultrabright source of entangled photon pairs', *Nature* 466, 217 (2010).
- [62] T. B. Norris, J.-K. Rhee, C.-Y. Sung, Y. Arakawa, M. Nishioka, and C. Weisbuch. 'Time-resolved vacuum Rabi oscillations in a semiconductor quantum microcavity', *Phys. Rev. B* 50, 14663 (1994).

- [63] Susanna M. Thon, Matthew T. Rakher, Hyochul Kim, Jan Gudat, William T. M. Irvine, Pierre M. Petroff and Dirk Bouwmeester, 'Strong coupling through optical positioning of a quantum dot in a photonic crystal cavity', *Appl. Phys. Lett.* 94, 111115 (2009).
- [64] Masayuki Shirane, Shunsuke Kono, Jun Ushida, and Shunsuke Ohkouchi, 'Mode identification of high-quality-factor single-defect nanocavities in quantum dot-embedded photonic crystals', *J. Appl. Phys.* 101, 073107 (2007).
- [65] E. Peter, P. Senellart, D. Martrou, A. Lemaitre, J. Hours, J. M. Gerard, and J. Bloch, 'Exciton-Photon Strong-Coupling Regime for a Single Quantum Dot Embedded in a Microcavity', *Phys. Rev. Lett.* 95, 067401 (2005).
- [66] J. P. Reithmaier, G. Sek, A. Löffler, C. Hofmann, S. Kuhn, S. Reitzenstein, L. V. Keldysh, V. D. Kulakovskii, T. L. Reinecke and A. Forchel, 'Strong coupling in a single quantum dot-semiconductor microcavity system', *Nature* 432, 197 (2004).
- [67] Xinlei Li, Jiang Wu, Zhiming M. Wang, Baolai Liang, Jihoon Lee, Eun-Soo Kim and Georgy. J. Salamo, 'Origin of nanohole formation by etching based on droplet epitaxy', *Nanoscale* 6, 2675 (2014).

Chapter 2

Simulation Methods

The computational results of the devices presented in this thesis were calculated using finite-difference time-domain (FDTD) and guided mode expansion (GME). This chapter begins with the general principles of FDTD simulations accompanied by discussing the accuracy and the computational cost of accurate calculating. In this chapter, a thorough explanation of GME is introduced along with a discussion of the advantages and accuracy comparing with FDTD method.

2.1 Finite Different Time Domain (FDTD)

Finite difference time domain (FDTD) (also known as Yee's method) is a primary numerical analysis method for modelling the propagation of electromagnetic waves [1]. It utilises centred finite difference approximations [2] to the grids in space and time for each electric and magnetic field vector component in the time-dependent Maxwell's equations. As it is a time-domain method, its modelling range covers from visible light through microwaves to ultralow-frequency, which is conducive to applications where a broadband result is desired or the resonant frequencies are not known exactly. The computation time of FDTD solutions is linearly related to the number of the spatial grids.

2.1.1 Principle of Operation

There are multiple software application to implement the FDTD method, such as MEEP, Lumerical Mode Solutions, Lumerical FDTD and so on, but central to each method are the Maxwell-Faraday equation and Ampere's circuital law in differential form [3]:

$$\begin{aligned}\nabla \times \mathbf{E} &= -\frac{\partial \mathbf{B}}{\partial t} \\ \nabla \times \mathbf{H} &= \frac{\partial \mathbf{D}}{\partial t} + \mathbf{J}_f\end{aligned}\quad (2.1)$$

Where \mathbf{H} and \mathbf{E} are the macroscopic magnetic and electric fields, respectively. \mathbf{J}_f is the electric free current density. The relations between magnetizing field \mathbf{H} and the magnetic field \mathbf{B} , as well as the displacement \mathbf{D} and the electric field \mathbf{E} can be specified by [3]:

$$\begin{aligned}\mathbf{H} &= \frac{1}{\mu} \mathbf{B} \\ \mathbf{D} &= \varepsilon \mathbf{E}\end{aligned}\quad (2.2)$$

where μ is the permeability and ε the permittivity of the material. Three scalar equivalent component (x, y, and z) equations can be obtained from Eq. (2.1) and (2.2).

$$\begin{aligned}\frac{\partial E_y}{\partial z} - \frac{\partial E_z}{\partial y} &= \mu_x \frac{\partial H_x}{\partial t} \\ \frac{\partial E_z}{\partial x} - \frac{\partial E_x}{\partial z} &= \mu_y \frac{\partial H_y}{\partial t} \\ \frac{\partial E_x}{\partial y} - \frac{\partial E_y}{\partial x} &= \mu_z \frac{\partial H_z}{\partial t}\end{aligned}\quad (2.3)$$

$$\begin{aligned}\frac{\partial H_z}{\partial y} - \frac{\partial H_y}{\partial z} &= \varepsilon_x \frac{\partial E_x}{\partial t} \\ \frac{\partial H_x}{\partial z} - \frac{\partial H_z}{\partial x} &= \varepsilon_y \frac{\partial E_y}{\partial t} \\ \frac{\partial H_y}{\partial x} - \frac{\partial H_x}{\partial y} &= \varepsilon_z \frac{\partial E_z}{\partial t}\end{aligned}\quad (2.4)$$

The simulation domain is composed of cubic cells as shown in Fig. 2.1. The magnetic fields (blue arrows) are recorded through the faces of each cubic cell

and the electric field (red arrows) along the edge of the cube as illustrated in Figure 2.1.

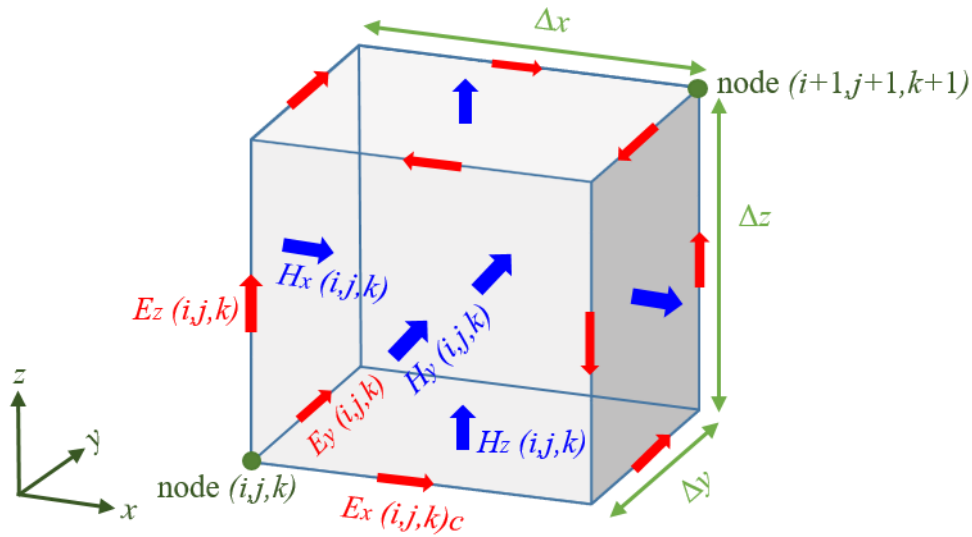


Figure 2.1: Schematic illustration of a standard cubic cell (Yee's cell) used in FDTD, where the magnetic and electric field vector components are distributed as the blue and red arrows, respectively.

In order to obtain the numerical solution of the differential equations, finite difference methods [2] are introduced. The principle is to replace the derivatives occurring in the differential equation by finite differences that approximate them as shown in Figure 2.2 and Eq. (2.6).

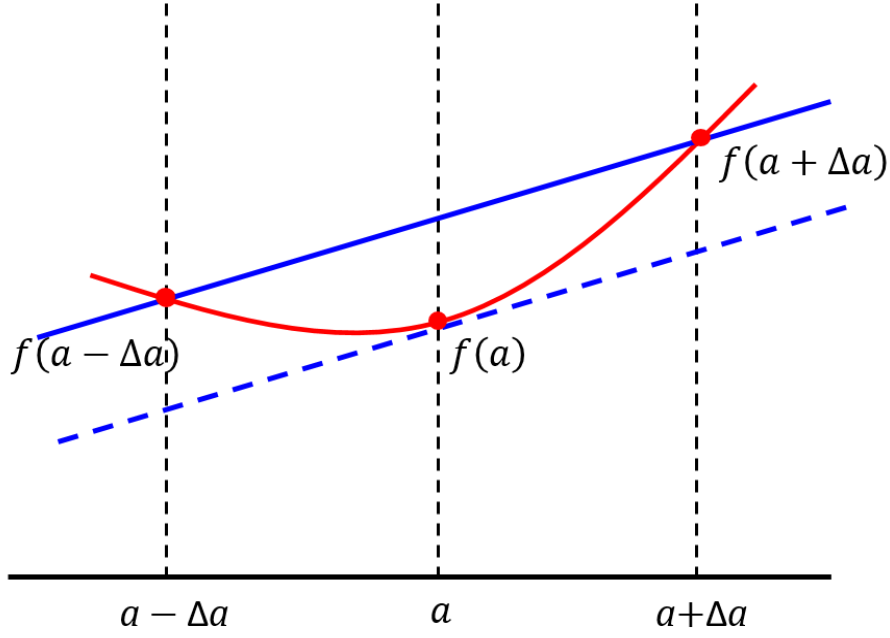


Figure 2.2: Illustration of the second-order accurate central difference formula.

$$\frac{df(a)}{da} = f'(a) \cong \frac{f(a+\Delta a) - f(a-\Delta a)}{2\Delta a} \quad (2.5)$$

The derivatives in Eq. (2.6) can then be represented by finite-differences and the scalar equivalent component equations are improved, as the following expression for the X component [4].

$$\begin{aligned} \varepsilon_x(i, j, k) \frac{E_x^{n+1}(i, j, k) - E_x^n(i, j, k)}{\Delta t} = \\ \frac{H_z^{n+0.5}(i, j, k) - H_z^{n+0.5}(i, j-1, k)}{\Delta y} - \frac{H_y^{n+0.5}(i, j, k) - H_y^{n+0.5}(i, j, k-1)}{\Delta z} \end{aligned} \quad (2.6)$$

$$\begin{aligned} \mu_x(i, j, k) \frac{H_x^{n+0.5}(i, j, k) - H_x^{n-0.5}(i, j, k)}{\Delta t} = \\ \frac{E_y^n(i, j, k+1) - E_y^{n+0.5}(i, j, k)}{\Delta z} - \frac{E_z^n(i, j+1, k) - E_z^n(i, j, k)}{\Delta y} \end{aligned} \quad (2.7)$$

The electric and magnetic field can be computed as follows:

$$E_x^{n+1}(i, j, k) = E_x^n(i, j, k) - \frac{\Delta t}{\epsilon_x(i, j, k)} \left(\frac{H_z^{n+0.5}(i, j, k) - H_z^{n+0.5}(i, j-1, k)}{\Delta y} - \frac{H_y^{n+0.5}(i, j, k) - H_y^{n+0.5}(i, j, k-1)}{\Delta z} \right) \quad (2.8)$$

$$H_x^{n+0.5}(i, j, k) = H_x^{n-0.5}(i, j, k) + \frac{\Delta t}{\mu_x(i, j, k)} \left(\frac{E_y^n(i, j, k+1) - E_y^{n+0.5}(i, j, k)}{\Delta z} - \frac{E_z^n(i, j+1, k) - E_z^n(i, j, k)}{\Delta y} \right) \quad (2.9)$$

where the electric fields at time instant $n + 1$ are calculated by the electric field at time constant n and the magnetic fields at time constant $n + 0.5$; the magnetic fields at time constant $n + 0.5$ are calculated by the magnetic fields at time constant $n - 0.5$ and the electric fields at time constant n . The calculations of electric and magnetic fields form the FDTD algorithm as explained schematically in Figure 2.3.

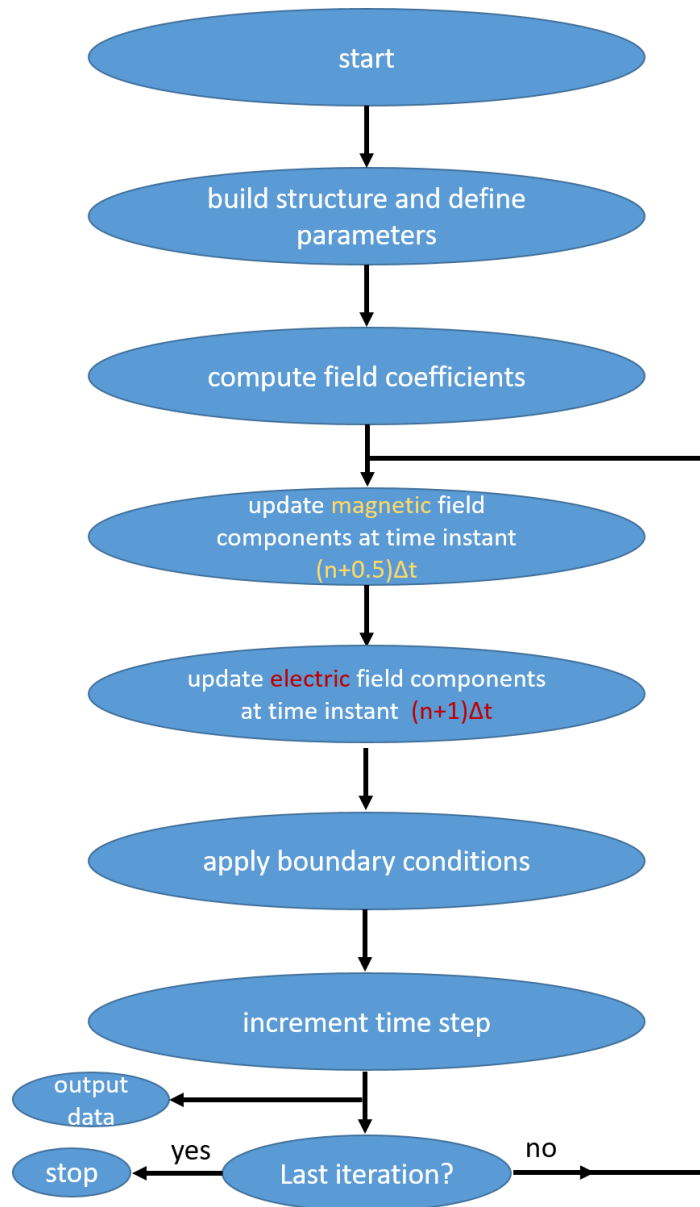


Figure 2.3: Schematic diagram of the Leap-frog algorithm of FDTD.

2.1.2 Grid and Step Size Considerations

In actual simulations, the lattice cells, filled with a weighted intermediate dielectric constant, must be gridded sufficiently finely to resolve both the smallest geometrical feature and the smallest electromagnetic wavelength. In this thesis, the grid and step

size are carefully designed for the air holes. In simulations, the circular shape of the air holes is approximated by the grid. It must be ensured that the approximation is the same for each hole, and is as close to a circle as possible.

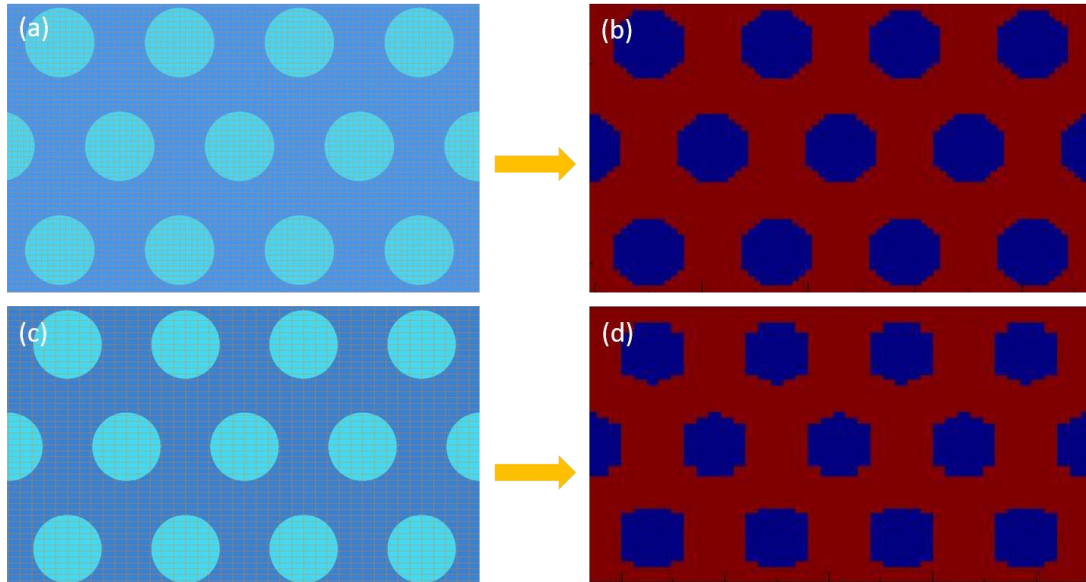


Figure 2.4: Air holes are approximated by different grid and step sizes. Uniform (a) and non-uniform (c) approximations correspond to identical approximately circular shapes (b) and random shapes (d), respectively.

2.1.3 Boundary Conditions

When considering the finite nature of the spatially gridded cells and the solutions to partial differential equations, it is essential to apply artificial boundary conditions at the edge of the simulation area to limit the computation. There are three main kinds of boundary conditions: absorbing [5], metallic [6] and periodic [7]. In this thesis, all the FDTD and varFDTD simulations have been carried out by applying perfectly matched layers (PML), artificial absorbing layers for Maxwell's equations. The key property of the PML is that the electromagnetic waves from the interior of the simulation region are strongly absorbed at the interface without reflecting them back into the interior. PML works very well in most cases and is widely used, but there are a few limitations such as

small numerical reflections for discretized wave equation [8], or unavoidable reflections (or even exponential growth) in 'left-handed' negative index metamaterials [9].

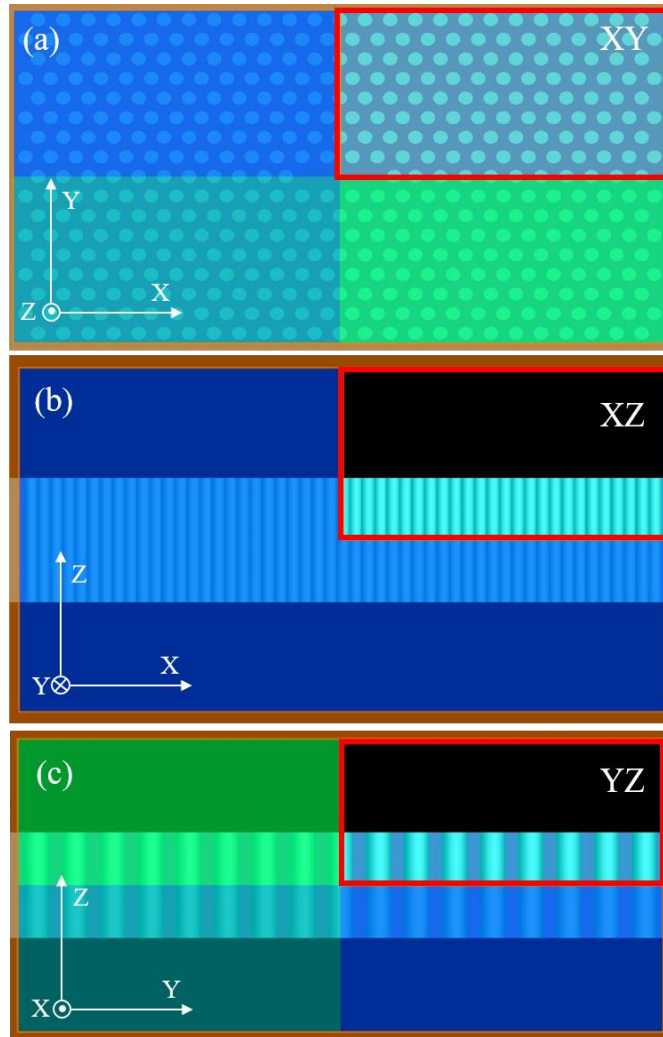


Figure 2.5: Plan view (a) and cross section views ((b), (c)) of the simulated photonic crystal single L3 cavity. Boundary conditions are applied in the red rectangle region. Light blue cylinders are the periodic air holes with refractive index $n = 1$. Green and blue colours indicate the anti-symmetric and symmetric boundary conditions, respectively. The actual simulation region is only $1/8$ of the whole structure.

Additionally, based on the symmetric shape of the simulated structure, mirror and rotational symmetry constraints can be applied along the principle axes, reducing the simulation time excessively. A typical example can be found in Figure 2.5, where the red rectangle region represents the actual simulation area with different views.

2.1.4 “2.5D” FDTD

As discussed above, FDTD is one of the most accurate and versatile methods for modelling the propagation of the electromagnetic waves. However, due to the high resolution grid and step size, large computational domains and long solution times are required. Devices with thin and long features, like wires, are difficult to simulate in FDTD due to the excessively large computational domain, making it difficult to model large integrated optical components efficiently. Alternatively, the varFDTD method [10] in MODE Solutions offers a way in which a fine grid along the Z-direction is not required and assumptions about an optical axis, structure geometry, or the materials are not necessary to make. The varFDTD method provides the best trade-off between simulation accuracy and speed: sufficiently accuracy and versatility to that of 3D FDTD, whilst only requiring the modelling time and memory of a 2D planar FDTD simulation. Here, in section 5.7 of this thesis, the varFDTD method was applied to simulate the large structures with photonic crystal cavities and waveguides. In order to get the accurate results, it is necessary to obtain the effective index.

2.2 Guided Mode Expansion (GME)

Guided mode expansion (GEM) is a novel approach to simulate the electromagnetic waves in patterned membrane photonic crystals, whose energies and fields can be found by a set of basis states from the unpatterned slab. The GME method is a highly specialised technique and offers strong benefits compared with FDTD.

2.2.1 Basic Configuration of GME

As discussed in Section 1.5.1, photonic crystal cavities fabricated by patterning a periodic structure on the unpatterned slab with different refractive index, combine the features of the 2D photonic crystals and slab waveguides, indicating the electromagnetic fields can be treated as a combination of 2D plane waves in XY directions and guided modes along the Z direction.

2.2.2 General Eigen Value Problem

The differential forms of Maxwell's equation for the magnetic field \mathbf{H} can be written as:

$$\nabla \times (\eta \nabla \times \mathbf{H}) = \frac{\omega^2}{c^2} \mathbf{H} \quad (2.10)$$

with the transversality condition

$$\nabla \cdot \mathbf{H} = 0 \quad (2.11)$$

Membrane patterning is introduced as the inverse of dielectric constant, $\eta \rightarrow \eta_0 + \tilde{\eta}$:

$$\nabla \times ((\eta_0 + \tilde{\eta}) \nabla \times \mathbf{H}) = \frac{\omega^2}{c^2} \mathbf{H} \quad (2.12)$$

The form of expanding magnetic field in a set of basis states, $\mathbf{H} \rightarrow \sum_{n,G} \alpha_{nG} \mathbf{H}_{nG}$, can be given by [11]

$$\sum_{n,G} \alpha_{nG} \nabla \times (\eta_0 \nabla \times \mathbf{H}_{nG}) + \sum_{n,G} \alpha_{nG} \nabla \times (\tilde{\eta} \nabla \times \mathbf{H}_{nG}) = \omega^2 \sum_{n,G} \alpha_{nG} \mathbf{H}_{nG}, \quad (2.13)$$

where n represents the mode order and G is the reciprocal lattice vector. Once the magnetic field is obtained, the electric field is calculated as

$$i \frac{c}{\omega} \eta \nabla \times \mathbf{H} = \mathbf{E} \quad (2.14)$$

The final eigenvalue equation can be expressed as Eq. (2.15) after a series of orthonormalization and rearranging, where K is the Bloch vector chosen from the first Brillouin zone.

$$\sum_{n',G'} K_{nG,n'G'} \alpha_{n'G'} = (\omega_{nG}^2 - \omega^2) \alpha_{nG} \quad (2.15)$$

2.2.3 Advantages of GME Method

The GME method is an approximation since the basis set of the guided modes of the effective waveguide is not complete (leaky modes are not included). However, the numerical effort is comparable to that of a 2D plane-wave calculation when a few guided modes are sufficient. The guided and quasi-guided photonic modes can be obtained without introducing any artificial layer (eg. PML) in the vertical direction, so it is very efficient and useful for design and parameter optimization.

2.3 Comparison with FDTD Method

Due to the approximation and the neglected leaky modes, it is essential to know the accuracy of GME method. The comparison between GME and FDTD has been performed on the same configuration, where two photonic crystal cavities are placed as shown in Figure 5.2(a). The energy differences between the anti-bonding and bonding modes are simulated and plotted in Figure 2.6, where red dots and blue triangles represent the results using GME and FDTD methods, respectively. Good agreement can be observed and demonstrate the subsequent results in Chapter 5 are reliable.

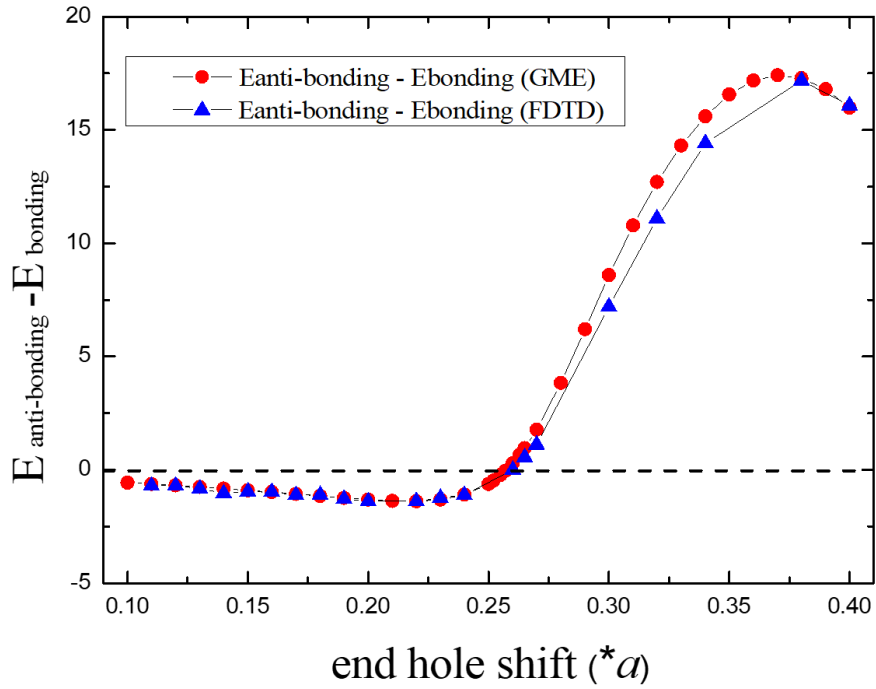


Figure 2.6: The comparison between GME and FDTD has been performed on the same configuration, where two photonic crystal cavities are placed as shown in Figure 5.2(a). The energy differences between the anti-bonding and bonding modes are simulated and plotted. Red dots and blue triangles are the results using GME and FDTD methods, respectively. Good agreement can be observed.

- [1] Kane Yee, 'Numerical solution of initial boundary value problems involving Maxwell's equations in isotropic media', IEEE Transactions on Antennas and Propagation 14, 302 (1966).
- [2] Paul Wilmott, Sam Howison, Jeff Dewynne, The Mathematics of Financial Derivatives: A Student Introduction, Cambridge University Press p137, ISBN 978-0-521-49789-3 (1995).
- [3] John Jackson, 'Maxwell's equations', Science Video Glossary, Berkeley Lab.
- [4] Dennis M. Sullivan, Electromagnetic simulation using the FDTD method, New York: IEEE Press Series (2000).
- [5] Bjorn Engquist and Andrew Majda, 'Absorbing Boundary Conditions for the Numerical Simulation of Waves', Mathematics of Computation 31, 629 (1977).
- [6] Ismo V. Lindell, Ari Sihvola, 'Electromagnetic Boundaries with PEC/PMC Equivalence', arXiv:1608.05519 (2016).
- [7] T. Schlick, Molecular Modeling and Simulation: An Interdisciplinary Guide, Interdisciplinary Applied Mathematics series 21, Springer (2002).
- [8] A. Chern, 'A reflectionless discrete perfectly matched layer', Journal of Computational Physics 381, 91 (2019).
- [9] R. A. Shelby, D. R. Smith, S. Shultz, 'Experimental Verification of a Negative Index of Refraction', Science 292, 77 (2001).
- [10] Manfred Hammer and Olena V. Ivanova, 'Effective index approximation of photonic crystal slabs: a 2-to-1-D assessment', Optical and Quantum Electronics 41, 267 (2009).
- [11] Steven G. Johnson, M. Ibanescu, M. A. Skorobogatiy, O. Weisberg, J. D. Joannopoulos, and Y. Fink, 'Perturbation theory for Maxwell's equations with shifting material boundaries', Phys. Rev. E 65, 066611 (2002).

Chapter 3

Experimental Methods

In this chapter, the experimental methods used to characterise the NFDE dots and photonic devices presented in this thesis will be outlined. Firstly, fabrication of the photonic crystal devices used in this thesis is briefly presented. Following this, the experimental measurement details for photonic samples will be described. Finally, the experimental setup for exploring spin properties of the nanohole-filled droplet-epitaxial (NFDE) QDs will be presented.

3.1 Fabrication of the Photonic Crystal L3 Cavities and Ring-Resonators

The photonic crystal L3 cavities and ring-resonators used in this thesis were prepared by bottom-up epitaxial growth and top-down lithographic techniques. In the growth processes, 1 μm layer of $\text{Al}_{0.6}\text{Ga}_{0.4}\text{As}$ is deposited on the GaAs substrate as a sacrificial layer, above which a 70 nm of GaAs layer is then deposited and forms the bottom barrier. A single layer of InAs QDs are formed before being capped with a 70 nm layer of GaAs as the top barrier. Typically, the principle of fabrication is to confine a single optical mode in the barrier slab with a height of $h=\lambda/2n$, where n is the refractive index of the barrier material. Additionally, the thickness of the sacrificial layer is chosen to protect the optical modes from the perturbation of the substrate. Here, the refractive index of

GaAs at 4K is $n = 3.4$ so that the central wavelength of the ensemble QD emission spectrum can be designed and tuned by the barrier slab height as $\lambda = 2n \cdot h$. Wafers are normally characterized before fabrication into specified devices, such as photonic crystal cavities. The desired pattern of the photonic devices are defined by electron beam lithography (EBL) [1-3] and subsequent etching [4, 5] techniques.

3.2 Photoluminescence Spectroscopy of Photonic Devices

Photoluminescence (PL) is a process where electron-hole pairs formed under optical excitation recombine, emitting photons. Quantum dots can be used to emit light under optical excitation. All experiments in this thesis were carried out using optical excitation, including non-resonant excitation for photonic devices and resonant scanning for NFDE QDs.

In a typical micro PL setup, as shown in Figure 3.2, the laser passes through a series of polarization optics and incidents on a beam splitter (BS). One exit path (green dotted line) leads to the objective lens focusing the laser onto the sample. The PL signal (magenta dotted line) is then collected by the same objective lens passing through another exit of the same beam splitter into the polarization optics and the detection apparatus. The PL measurements for photonic crystal L3 cavities are in typical configuration as described above, while the basic configuration for ring resonator transmission measurements is slightly different. The key to perform selective excitation and collection of light from different regions of the sample whilst making certain of good isolation between the two is using a confocal microscopy setup based on the experimental configuration, as shown in Figure 3.2.

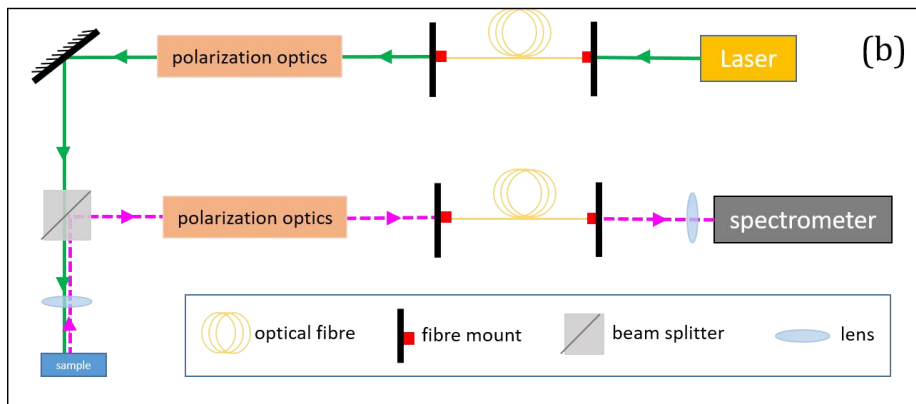
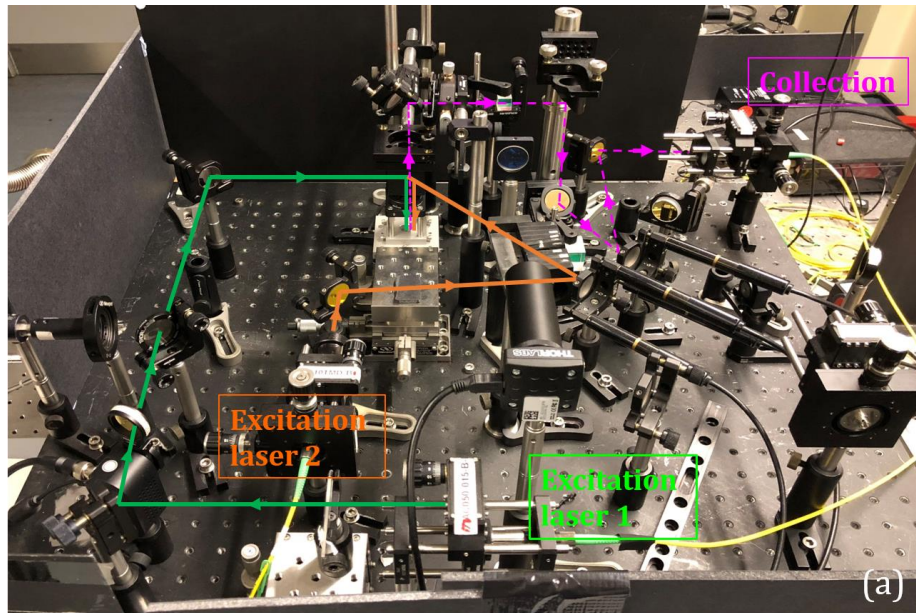


Figure 3.2: A photo of the equipment (a): green and orange lines indicate the excitation light paths; dashed magenta lines are for the collection path. Simplified schematic diagram of the experimental configuration for photoluminescence measurements of photonic devices (b).

Single mode optical fibres are used to couple the laser to/from the sample, on which a diffraction-limited laser spot of $\sim 1\mu\text{m}$ diameter is produced by the guiding core, working as the pinhole required for confocal microscopy. This guarantees the light coupled with fibres is only from/ to a spatially specified spot on the sample so that the transmission measurements through the sample can be performed by separating the

two spots. Figure 3.2 (a) shows a photo of the equipment, where the green and magenta lines indicate the excitation light path 1 and path 2, respectively. Excitation and collection spots can be lined up individually by rotating the mirrors in the excitation (green/orange lines) and collection (magenta lines) light path, respectively. The non-resonant excitation for photonic crystal L3 cavities and ring resonators were implemented using a diode laser (808nm wavelength) and a He:Ne laser (633nm wavelength), respectively. A 0.75 m and a 0.55 m single spectrometer (Acton Spectrometer from Princeton Instrument) were used to detect the PL signals by a liquid nitrogen cooled charge coupled device (CCD). The highest resolution of the spectrometer is approximately $20 \mu eV$.

Due to the requirement of quick exchange of samples, photonic devices were mounted on the cold finger of a continuous flow cryostat with a reasonable degree of stability. A picture of the cryostat is provided in Figure 3.3, where the sample is mounted on a copper cold finger which is in thermal contact with an external heat exchanger and the sample contained within the evacuated chamber. Liquid helium is pumped through the heat exchanger to cool the sample down to 4-10 K. On top of the sample chamber, an optical window allows optical access to focus on the sample. Micrometer driven manual translation stages were fixed under the cryostat to provide the movement around the sample and focus control.

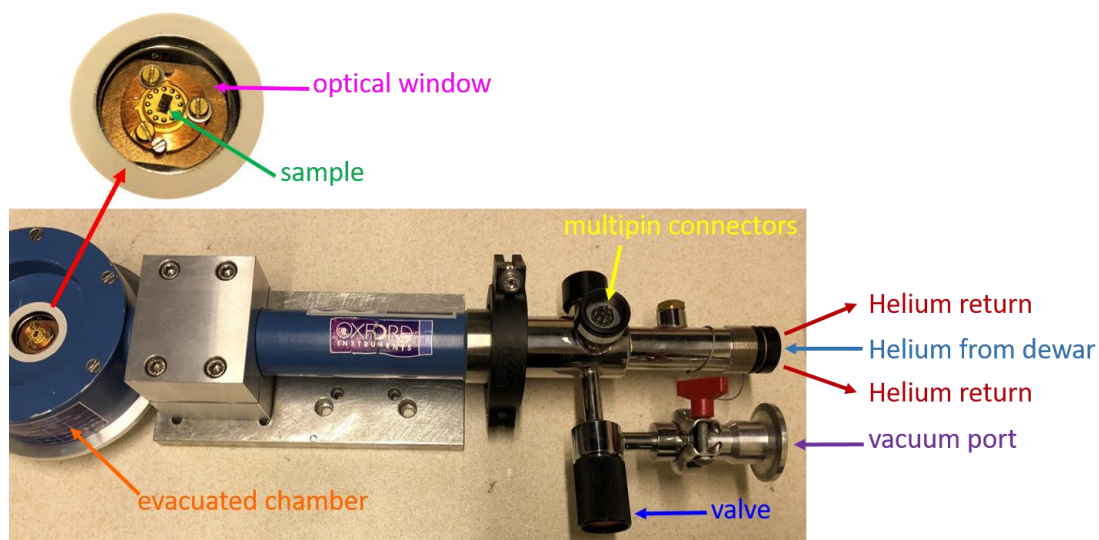


Figure 3.3: Photograph of the cryostat used for PL measurements.

The vibration of the system is mainly caused by the helium pump, and generally the system will maintain the alignment with the incident light for about an hour. As a result, a more stable system is required for long exposure measurements. However, for the purpose of fast characterisation and short exposure measurement, the flow cryostat is an ideal option.

3.3 Characterization of NFDE QDs

The NFDE QDs sample is held in a liquid helium bath cryostat where the temperature is down to 4.2 K and the superconducting magnet provides the magnetic field. The bath cryostat system used in this thesis is schematically illustrated in Figure 3.4.

The main framework of the bath cryostat is supported by a low-loss liquid helium Dewar. The outer and inner vacuum jackets are both pumped to suppress the thermal conduction and convection. Liquid nitrogen is filled between the outer and inner vacuum jackets as another insulating layer. The liquid nitrogen jacket serves as a pre-cooler, protecting the liquid helium from being warmed up (reduce the waste of liquid helium), and absorbs the radiation and heat from the room temperature environment. All these insulating “jackets” ensure a very low loss rate of liquid helium bath cryostat system, which can remain stable for up to several days.

The superconducting magnet [6], made up with superconducting wires, is assembled in the bottom of the bath cryostat. Magnetic fields are achieved by immersion of a superconducting magnet in the liquid helium bath when the magnet is powered by current source. A uniform magnetic field up to 10 T can be reached. Magnetic fields applied in this thesis were in the Faraday geometry, along the sample growth axis.

Cryogenic temperatures for the sample chamber are achieved by immersing a home-made evacuated tube in a Dewar filled with liquid helium at $\sim 4.2\text{K}$. A small amount of helium gas is the medium to achieve the thermal equilibrium in the insert tube. Within the insert tube is a home-made optical cage system, where the sample is mounted on a 3D piezoelectric stack which moves the sample and controls the focus. An aspheric lens is fixed above the sample for focusing the incident light to a spot of $\sim 1\mu\text{m}$ diameter. The aberration effects of the aspheric lens are reduced by two achromatic doublets

mounted along the cage length [7]. On the top of the insert tube is an optical imaging system, which contains an optics board and optical components, leading the optical access to the sample via the optical window on the top of the insert tube.

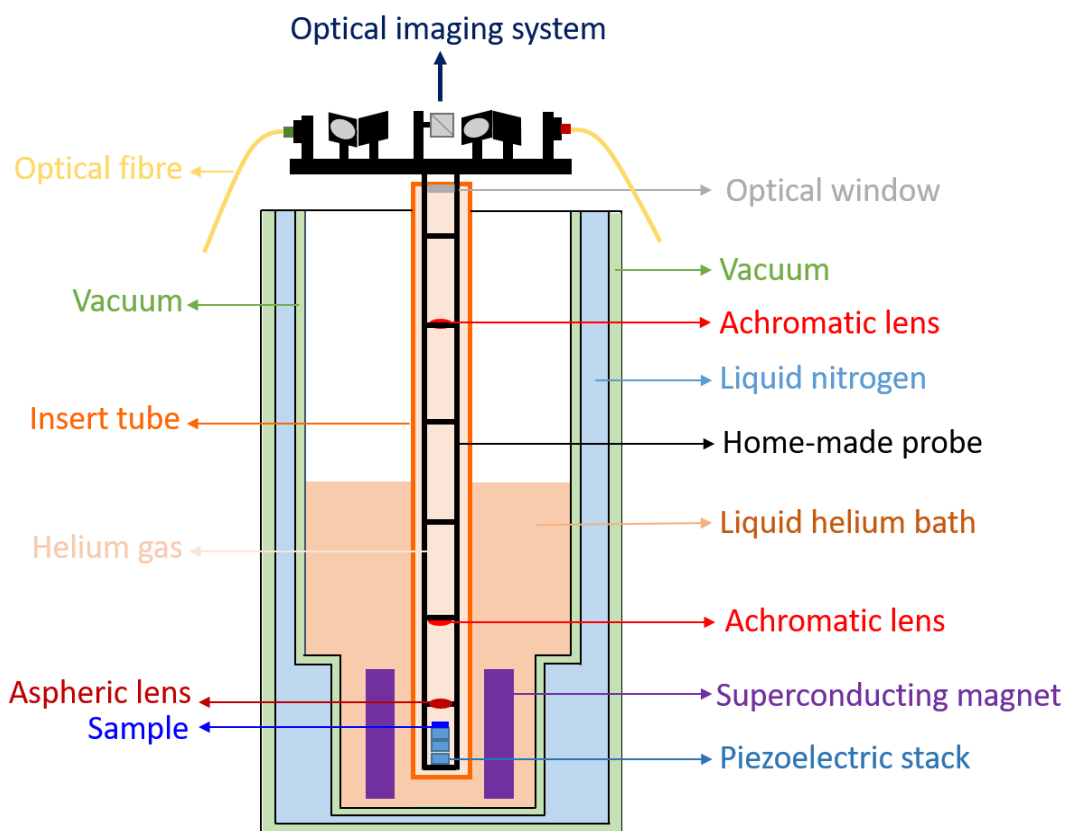


Figure 3.4: Schematic illustration of a liquid helium bath cryostat with superconducting magnet, integrated optics and piezoelectric stack. The optical imaging system mounted on the top of the cryostat can be found in Figure 3.5.

The measurements of PL, dynamic nuclear polarization (DNP), nuclear magnetic resonance (NMR) and nuclear spin decay, presented in Chapter 4, have been carried out on single dots at low temperature using a confocal spectroscopic setup as schematically illustrated in Figure 3.4 and 3.5. Polarization of the incident laser and the detected signal can be tuned by polarization optics. Two laser beams are introduced as pump and prob.

Pump-probe experimental methods are used through all the measurements in Chapter 4. Details will be presented in Chapter 4.

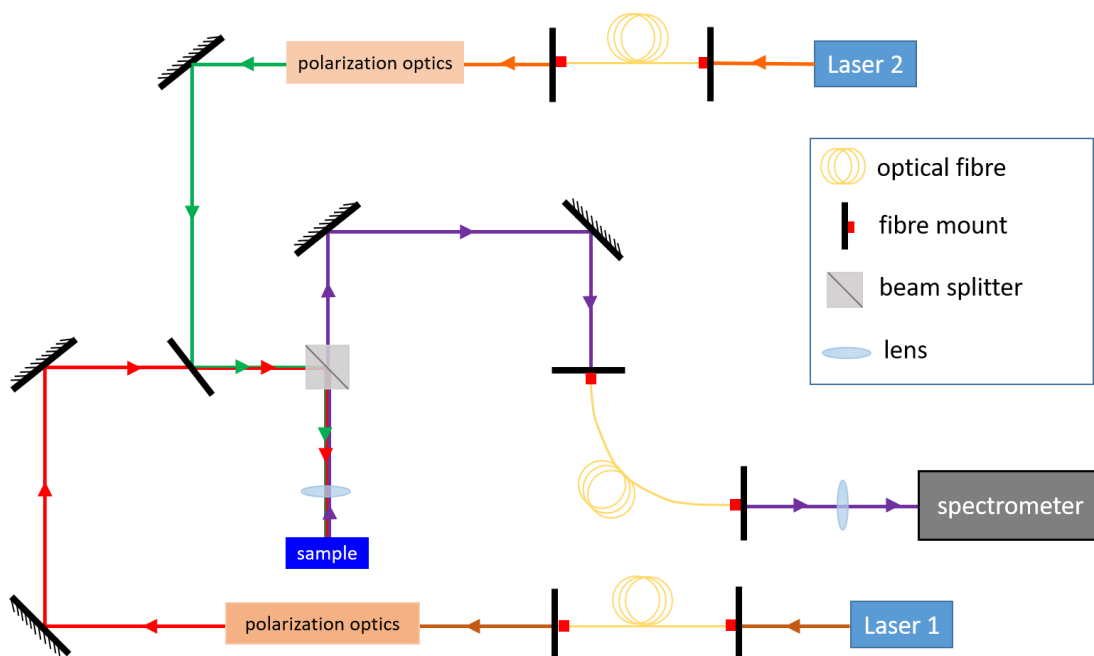


Figure 3.5: Simplified schematic diagram of the experimental configuration for measurements of photoluminescence (PL), dynamic nuclear polarization (DNP), nuclear magnetic resonance (NMR) and nuclear spin decay on NFDE single dots. Excitation and collection spots can be lined up individually by rotating the mirrors in the excitation and collection light paths, allowing the inter-dot DNP process experiment in Chapter 4.

- [1] N. W. Parker et al, 'High-throughput NGL electron-beam direct-write lithography system', Proc. SPIE: Emerging Lithographic Technologies (2000).
- [2] K. W. Lee, 'Secondary electron generation in electron-beam-irradiated solids: resolution limits to nanolithography', J. Kor. Phys. Soc. 55, 1720 (2009).
- [3] Kenji Yamazaki, Kenji Kurihara, Toru Yamaguchi, Hideo Namatsu, Masao Nagase, 'Novel Proximity Effect Including Pattern-Dependent Resist Development in Electron Beam Nanolithography', Jpn. J. Appl. Phys. 36, 7552 (1997).
- [4] R. Chanson, A. Martin, M. Avella, J. Jiménez, F. Pommereau, J. P. Landesman and A. Rhallabi, 'Cathodoluminescence Study of InP Photonic Structures Fabricated by Dry Etching', Journal of Electronic Materials 39, 688 (2010).
- [5] V. Hortelano et al, 'Intermixing in InP-Based Quantum Well Photonic Structures Induced by the Dry-Etching Process: A Spectral Imaging Cathodoluminescence Study', Materials Science Forum 725, 97 (2012).
- [6] E. D. Adams, J. M. Goodkind, 'Cryostat for Investigations to Temperatures below 0.02 K', Cryogenics 3, 83 (1963).
- [7] F. Grazioso, B. R. Patton, and J. M. Smith, The Review of Scientific Instruments 81, 093705 (2010).

Chapter 4

Vanishing electron g factor and long-lived nuclear spin polarization in weakly strained nanohole-filled GaAs/AlGaAs

4.1 Introduction

In the past three decades, electronic spin in semiconductors and their nanostructures, such as quantum dots (QDs), has attracted much attention as it is promising for applications in quantum computation [1-6]. For a semiconductor QD, spin injection and its coherent manipulation can be easily achieved by optical or electrical pumping, making it compatible with the modern optoelectronic integration circuits. Moreover, due to the three-dimensional (3D) confinement, the spin-orbit relaxation effects is suppressed and thus longer spin coherence time is expected. The main factor that limits the electron or hole spin coherence time in a QD is the hyperfine interaction with the nuclear spin environment [1, 6-8]. Therefore, further increase of spin coherence time of carriers in a QD, which is crucial for single spin qubit manipulation, requires an extra control over nuclear spin bath. This extra control can be achieved by maximizing polarization of 10^4 - 10^5 nuclei in a single QD to form well-defined nuclear spin states, and thus suppress the effects caused by nuclear field fluctuations [9-13]. In addition to

the hyperfine coupling, strain-induced quadrupolar effects also have an impact on electron spin decoherence [14, 15]. Consequently, a high-quality QD system, where nuclear quadrupolar effects are minimized, is highly desirable.

The coherent control of carrier spin in a semiconductor QD using resonant ultrafast laser pulses [3-5] has been demonstrated. However, the scalability of this technique is still demanding. Alternatively, spin rotation can be controlled by manipulating its coupling to the external magnetic field or electrically modulating the g -factor [16-18], which relies on the tunability of the g -factor (especially the sign of the g -factor).

Self-assembled InGaAs/GaAs QDs, formed by the Stranski-Krastanow (SK) growth mode, have been one of the major QD systems for spintronics over decades because of their excellent optical qualities. For a long period of time, it was not achievable by the monolayer-fluctuation grown GaAs/AlGaAs dots. The recent development of the droplet epitaxial (DE) growth technique, in particular, nanohole-filled droplet epitaxy (NFDE) (dots are formed by in situ etching and nanohole in-filling), provides GaAs QDs with strong quantum confinement and excellent optical properties [19-22]. Meanwhile, these dots exhibit high symmetries which are unattainable in self-assembled dots [23]. The combination of high crystalline and optical qualities make NFDE QDs ideal candidates for polarization entanglement and photon induced spin manipulation [24]. Although the NFDE QDs have shown their high efficiency in the study of rubidium atoms and a quantum dot interface [25, 26], the spin properties of the carriers in such systems remain to be explored.

In this chapter, photoluminescence (PL) and nuclear magnetic resonance (NMR) spectroscopy are used to study the spin properties of the NFDE grown GaAs/AlGaAs QDs, including the single charge spins and the nuclear spin matrix. Magnetophotoluminescence measurements reveal close-to-zero electron g -factor for the NFDE QDs. Efficient dynamic nuclear polarization (DNP) as large as 65% is also demonstrated.

In order to measure the residual strain in the NFDE grown QDs, radio-frequency (RF) excitation was applied in the NMR experiments and a strain as small as $<0.02\%$ was revealed. Two subgroups of ensemble QDs with compressive and tensile strain along the growth axis were investigated, corresponding to those formed in the nanoholes and at

the rims of the nanoholes, respectively. In such QDs, small quadrupolar effects (~ 20 kHz) was observed due to the small strain, resulting in a large increase of the electron spin coherence time [14, 15]. Although the residual strain is relatively small, it is sufficiently large to induce stable nuclear spin matrix with a relaxation time >500 s. These results suggest that the NFDE QDs can be excellent candidates for spin qubit manipulation as decoherence effects from the nuclear spin environment can be largely minimized.

4.2 Samples and Techniques

As illustrated in Section 1.2, the NFDE QDs sample was grown using solid source molecular beam epitaxy (MBE), and GaAs quantum dots are formed after deposition of Ga, $\text{Al}_{0.44}\text{Ga}_{0.56}\text{As}$ and GaAs in a specific order. The sample was mounted on a 3D piezo stage in the liquid helium bath cryostat with a superconducting magnet as described in Section 3.3. Magnetic fields up to 10 T applied in this experiment were in Faraday geometry, along the sample growth axis. All the measurements, including typical photoluminescence (PL), dynamic nuclear polarization (DNP), nuclear magnetic resonance (NMR) and nuclear spin decay, were performed on single dots at low temperature $T \sim 4.2$ K using a confocal spectroscopic setup. The laser beam can be focussed to a $\sim 1 \mu\text{m}$ spot. The polarization degree of the nuclear spins can be determined by measuring the Overhauser shifts of the excitonic peaks in the PL spectra of QDs. More details about the nuclear spin polarization and the NMR spectroscopy method [27] will be described in this chapter.

4.3 Experimental Results

A typical wide range PL spectrum obtained under non-resonant excitation ($E = 1.69$ eV) with magnetic field $B_z = 6$ T is presented in Figure 4.1. Quantum well (QW) emission can be identified at $E = 1.67$ eV. Two spectral distributions of QD emission at $E = 1.58$ eV and at $E = 1.63$ eV are denoted as type A dots and type B dots, respectively. This chapter investigates various aspects of the spin properties based on type A and B dots (the origin of these two types of QDs will also be discussed). Typically, PL emission from 5–10 dots within the excitation spot of $\sim 1 \mu\text{m}^2$ can be observed in the experiments. Although this

density is too high to reliably distinguish individual dots, it is sufficiently low to identify and interpret hyperfine spectral structures.

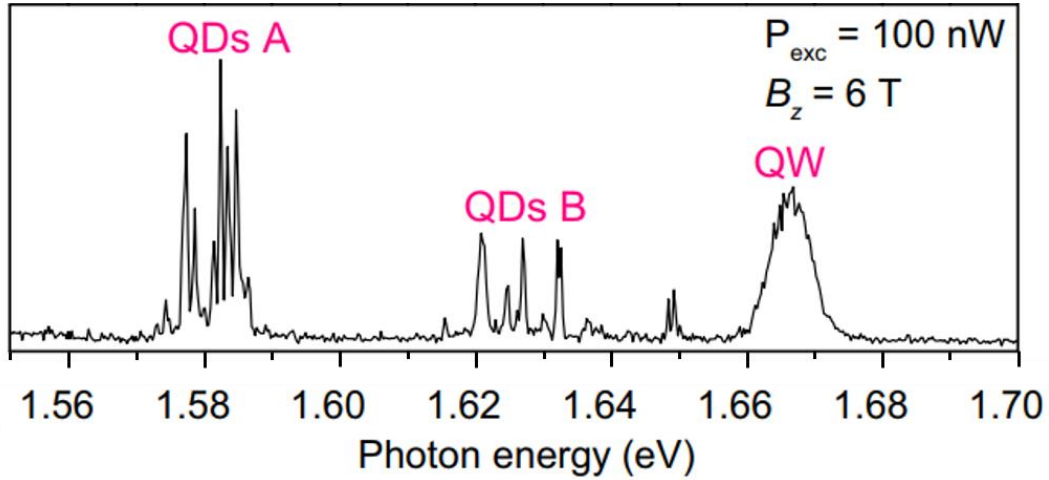


Figure 4.1: A wide range low-temperature photoluminescence spectrum indicates emission from two different types of quantum dots (A and B) and the quantum well under nonresonant excitation ($E = 1.96 \text{ eV}$) with magnetic field $B_z = 6 \text{ T}$.

4.3.1 Magnetic Properties of Single Charges: Close-to-Zero Electron g Factors

As described in Section 1.3.3, in semiconductors, an exciton is a hydrogen-like quasiparticle consisting of a bound pair of electron and hole. It releases its energy via electron-hole recombination, governed by the selection rules. The exciton with electron spin (up \uparrow or down \downarrow) and hole spin (up \uparrow or down \downarrow) satisfying the optical selection rules is called a bright exciton, which emits a photon during recombination. When the electron spin and hole spin of an exciton do not satisfy the selection rules, spin of one component (electron or hole) flips (or relaxes) before the recombination and energy is released via photon emission; however, no emission can be observed in spectra. This type of exciton is referred as the dark exciton (optically forbidden exciton) and usually has long life time. Due to the non-ideal symmetry in QDs, the exchange interaction couples the bright and dark states [28]. As a result, the dark states gain small oscillator strength and can be observed in the photoluminescence spectra [28-30].

A series of PL spectra of QD B1 obtained under different magnetic field B_z with low excitation power $P_{\text{exc}} = 200$ nW are presented in Figure 4.2. The emission from excitons can be observed in Figure 4.2(a), where the two main brightest peaks indicate $|\downarrow\uparrow\rangle$ (where the hole spin is \downarrow and the electron is \uparrow) and $|\uparrow\downarrow\rangle$ bright excitons. The green and magenta spectra correspond to linear polarizations at $B_z = 0$. The black diamonds and green triangles correspond to the weak peaks from dark excitons $|\uparrow\uparrow\rangle$ and $|\downarrow\downarrow\rangle$, respectively. At $B_z = 3$ T, the emission of the $|\uparrow\uparrow\rangle$ dark exciton is enhanced in δ^- polarization due to the mixing with $|\downarrow\uparrow\rangle$ bright exciton.

PL energies of bright (full symbols) and dark (open symbols) exciton peaks extracted from the spectra in Figure 4.2(a) are fitted by solid lines in Figure 4.2(b). The fitting are performed using the following equations:

$$E_b = E_0 + [\kappa + \kappa^{(1)}B_z]B_z^2 + \frac{1}{2}\delta_0 \pm \frac{1}{2}\sqrt{\delta_b^2 + \mu_B^2[g_h + g_h^{(1)}B_z - g_e]^2B_z^2}, \quad (4.1)$$

$$E_d = E_0 + [\kappa + \kappa^{(1)}B_z]B_z^2 - \frac{1}{2}\delta_0 \pm \frac{1}{2}\mu_B[g_h + g_h^{(1)}B_z + g_e]B_z, \quad (4.2)$$

where E_b represents the energy of bright excitons, E_d represents dark excitons, E_0 is the QD bandgap energy, δ_0 is the splitting between bright and dark exciton doublets, δ_b is the fine-structure splitting of bright exciton (dark exciton splitting is neglected), g_e is the g -factor of electron, g_h is the g -factor of hole, κ is the diamagnetic shift and μ_B is the Bohr magneton. $\kappa^{(1)}$ and $g_h^{(1)}$ are the corrections for diamagnetic shift and hole g -factor, respectively.

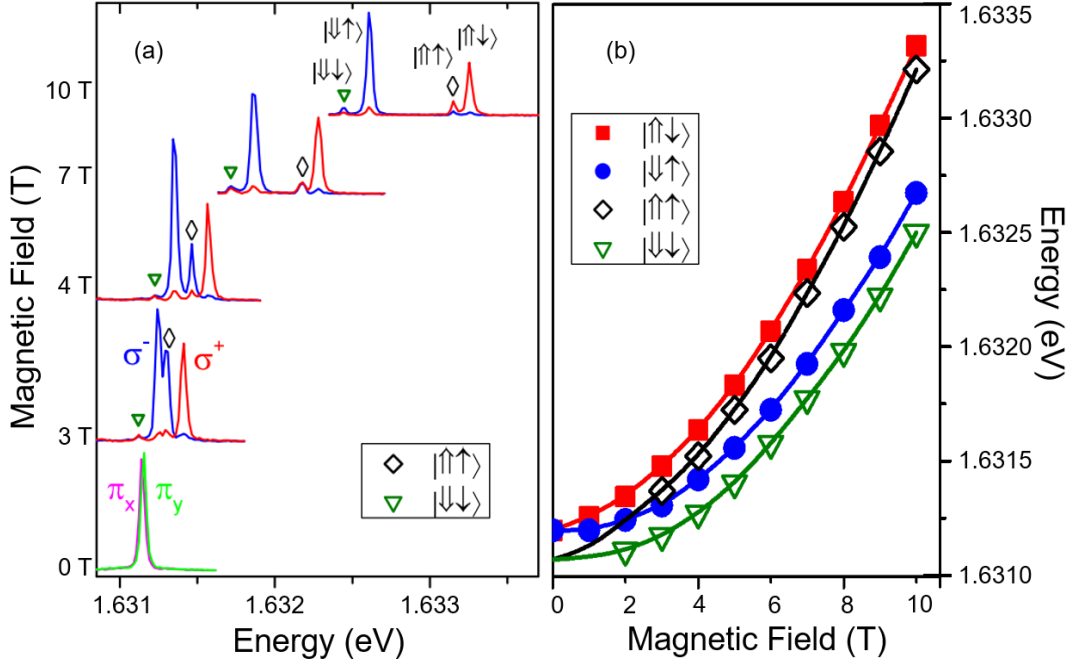


Figure 4.2: Magnetophotoluminescence measurements of NFDE quantum dots. (a) Magnetic field dependence of PL emission from bright and dark excitons in dot B1 with an excitation power of $P_{\text{exc}} = 200$ nW. The green and magenta spectra correspond to linear polarizations at $B_z = 0$. Blue and red lines correspond to spectra recorded under σ^- and σ^+ polarization, respectively. The black diamonds and green triangles indicate the PL emission from dark quantum dots. (b) Energies of the bright (full red and blue symbols) and dark (open black and green symbols) exciton peaks from (a). The data are fitted by solid lines using Eq. (4.1) and Eq. (4.2).

The accuracy of fitting the experimental data measured for QD B1 can be obtained by examining the fitting residuals. Here, the residuals, plotted in Figure 4.3, are the difference between experimental data from Figure 4.2 and theoretical calculations using Eq. (4.1). Symbols in Figure 4.3 (a) are the residuals of fitting where magnetic-field-dependent corrections for diamagnetic shift and hole g-factor are set as $\kappa^{(1)} = 0$ and $g_h^{(1)} = 0$ in Eq. (4.1), respectively. The systematic errors are prominent and with a value of $\sim \pm 50$ μeV . The importance of adding the magnetic-field-dependent corrections to

diamagnetic shift and hole g-factor should be noticed. In Figure 4.3 (b), the systematic errors drop to $\sim \pm 20 \mu\text{eV}$ by introducing $\kappa^{(1)}$ as a fitting variable while keeping $g_h^{(1)} = 0$. It is also obvious that the excitons with parallel hole spin but antiparallel electron spin have the same signs of fitting residuals (red squares $|\uparrow\downarrow\rangle$ and black diamonds $|\uparrow\uparrow\rangle$); blue circles $|\downarrow\uparrow\rangle$ and green triangles $|\downarrow\downarrow\rangle$); the excitons with antiparallel hole spin and parallel/antiparallel electron spin have the opposite signs of fitting residuals (red squares $|\uparrow\downarrow\rangle$ and green triangles $|\downarrow\downarrow\rangle$ / blue circles $|\downarrow\uparrow\rangle$). The remaining systematic errors caused by hole spin can be further eliminated by setting magnetic-field-dependent corrections for hole g-factor as a fitting variable. Fitting residuals are reduced to $< \pm 10 \mu\text{eV}$ suggesting that the systematic errors are eliminated effectively by fitting with variable diamagnetic shift corrections $\kappa^{(1)}$ and hole g-factor corrections $g_h^{(1)}$, see in Figure 4.3 (c).

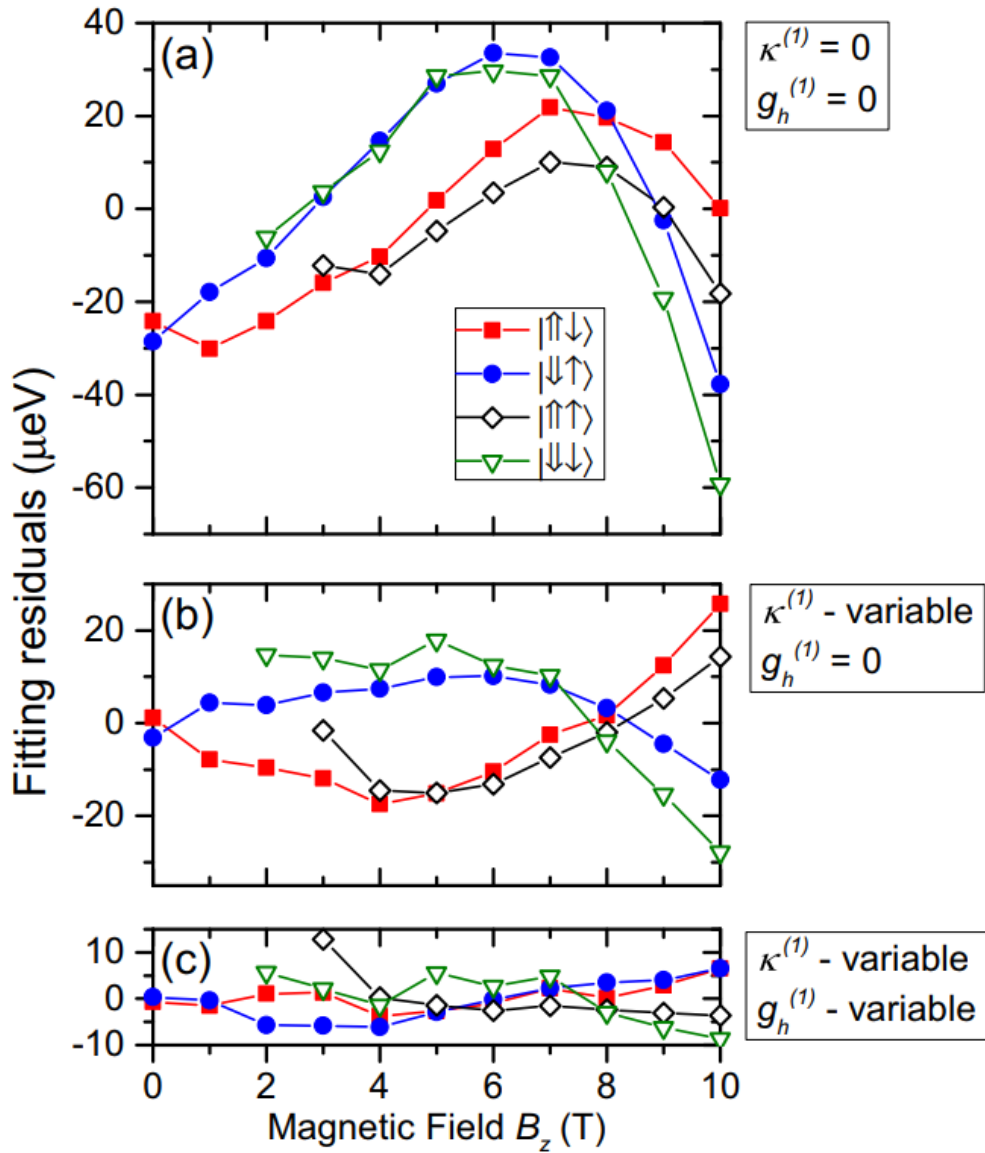


Figure 4.3: Fitting residuals, the difference between experimental data from Figure 4.2 and theoretical calculations using Eq.(4.1) and Eq.(4.2), show the accuracy of fitting process for all excitons as a function of magnetic field. (a) A huge systematic error of $\sim \pm 50 \mu\text{eV}$ results from fitting without linear corrections ($\kappa^{(1)} = 0, g_h^{(1)} = 0$). (b) The systematic errors drop to $\sim \pm 20 \mu\text{eV}$ by introducing diamagnetic shift correction $\kappa^{(1)}$ as a variable while keep $g_h^{(1)} = 0$. (c) Fitting residuals ($< \pm 10 \mu\text{eV}$), achieved by setting diamagnetic shift correction $\kappa^{(1)}$ and hole g-factor correction $g_h^{(1)}$ as variables, are within the accuracy.

Electron g-factor values for QD B1 are obtained from the fitting, where $g_e \approx 0.054 \pm 0.041$ with $\kappa^{(1)} = 0, g_h^{(1)} = 0$; $g_e \approx 0.053 \pm 0.023$ with $g_h^{(1)} = 0$ and $\kappa^{(1)}$ as a variable; $g_e \approx 0.052 \pm 0.009$ with both $\kappa^{(1)}$ and $g_h^{(1)}$ as variables. It can be seen that the values of g_e are similar including and excluding $\kappa^{(1)}$ and $g_h^{(1)}$, but systematic errors are further reduced by using magnetic-field-dependent corrections as fitting variables. The other fitting parameters for QD B1, derived from fitting with $\kappa^{(1)}$ and $g_h^{(1)}$ as variables, are as following: $E_0 = 1.631143 \pm 4 \times 10^{-6}$ eV , $\delta_0 = 122 \pm 3$ μ eV , $\delta_b = 12.7 \pm 13.2$ μ eV , $\kappa = 21.2 \pm 0.3$ μ eV T⁻² , $\kappa^{(1)} = -0.35 \pm 0.03$ μ eV T⁻³ , $g_h = 0.86 \pm 0.04$ and $g_h^{(1)} = 0.031 \pm 0.004$ T⁻¹ . Similar magneto-PL measurements (Figure 4.4(a)-(h)) and fitting procedures (Figure 4.5(a)-(j)) have been performed for a set of individual QDs from the same sample. Figure 4.4(a)-(d) are the magnetic field dependences of PL emissions from bright and dark excitons in QDs under σ^+ excitation with an excitation power of $P_{exc} = 200$ nW. While Figure 4.4(e)-(h) are under σ^- excitation. From these spectra with high signal/noise ratio and the fittings, A and B type QDs can be well distinguished as their corresponding bandgap energy E_0 , g-factors are very different. In Figure 4.4, QD42L and QD56 are type A QDs ($E_0 \sim 1.58$ eV (~ 785 nm)); QD42S-a, QD42S-b and QD50 are type B QDs ($E_0 \sim 1.63$ eV (~ 760 nm)). In order to show clearly the different g-factors for these two types of QDs, the electron and hole g-factors of type A QDs (black squares) and type B QDs (red triangles) were extracted and plotted in Figure 4.6.

The electron and hole g-factors of QDs in type A (black squares) and QDs type B (red triangles) are extracted and plotted in Figure 4.4 (a). Unexpectedly, for type B QDs, the values of electron g-factor are close to zero with an average value of $g_e \approx +0.05$. In typical GaAs/AlGaAs quantum dots, formed by natural fluctuation of the quantum well width, the average value of electron g-factor is an order of magnitude larger [31]. Electron g-factor values for QDs of type A are also small with a negative value of $g_e \approx -0.1$ [48].

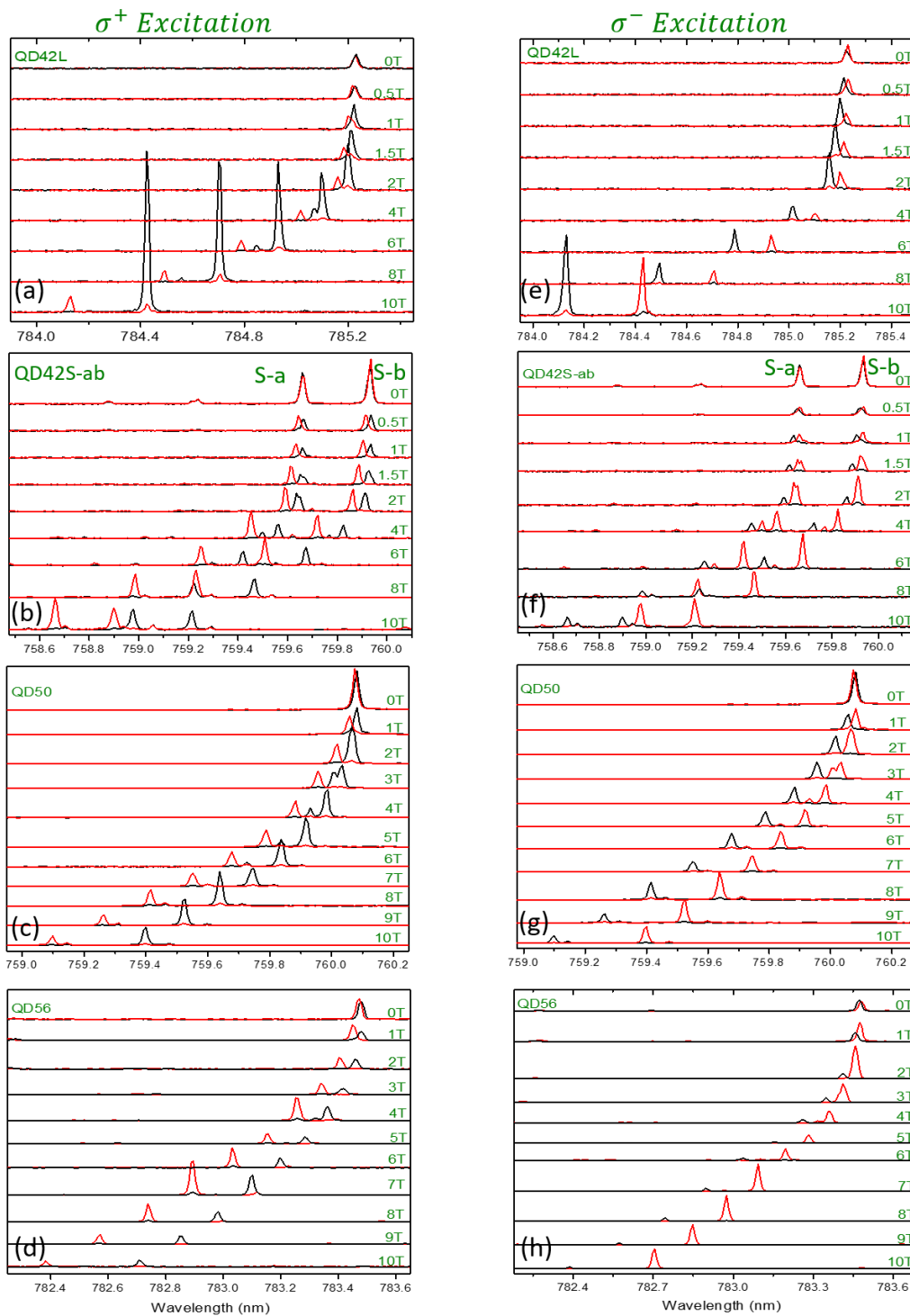


Fig. 4.4 Magneto-PL measurements of a set of individual A and B type QDs on the same sample. (a)-(d) and (e)-(h) are the magnetic field dependences of PL emissions from bright and dark excitons in QDs under σ^+ and σ^- excitation, respectively. Black and red curves correspond to spectra recorded under σ^- and σ^+ polarization, respectively.

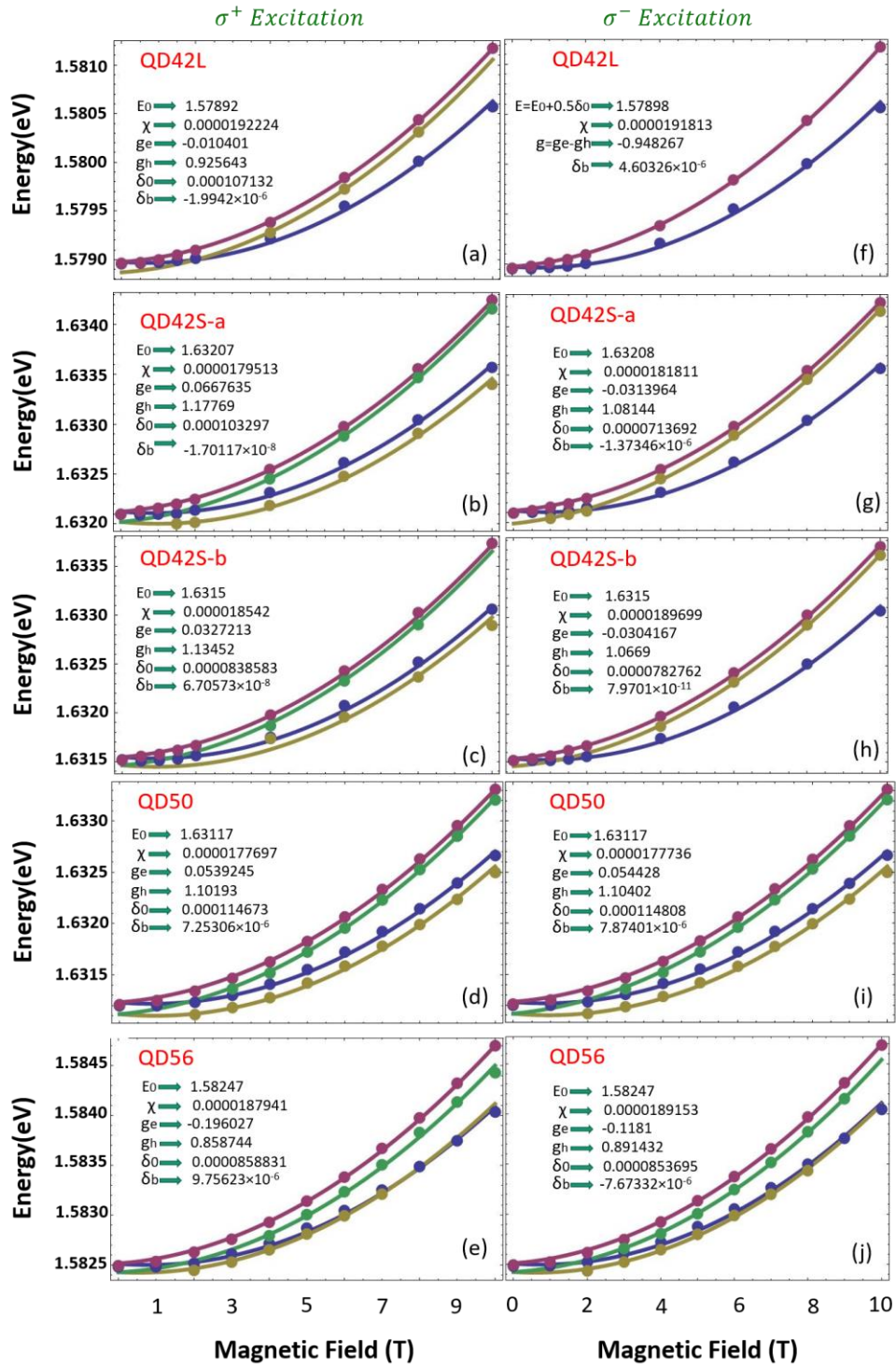


Figure 4.5: Energies of the bright (purple and blue symbols) and dark (brown and green symbols) exciton peaks from Figure 4.4 (a)-(h), fitted by solid lines using Eq. (4.1) and Eq. (4.2).

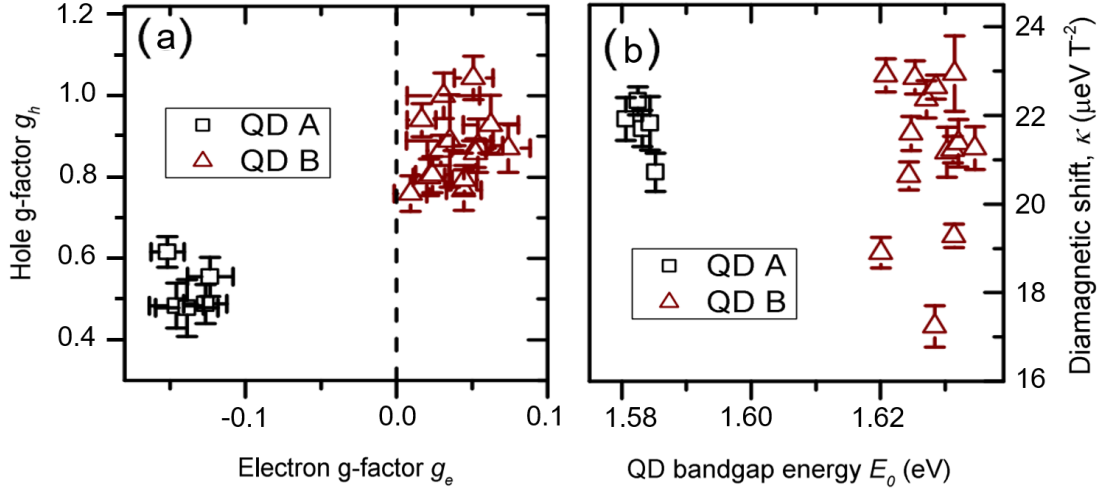


Figure 4.6: The electron and hole Lande g -factors (a) and the diamagnetic shifts κ (b) for A type of QDs (black squares) and B type of QDs (red triangles) are extracted from the fitting in Figure 4.2(b) and Figure 4.5. All the QDs are from the same piece of sample.

Figure 4.6 (b) shows the diamagnetic shift κ versus QD bandgap energies E_0 for the same QDs as in Figure 4.6 (a). As is reported, for natural GaAs/AlGaAs QDs and DE-grown GaAs/AlGaAs dots (obtained by crystallization of Ga droplets), the values of the diamagnetic shift κ are $\sim 10 \mu\text{eV T}^{-2}$ and $\sim 4 - 8 \mu\text{eV T}^{-2}$, respectively. However, for both type A and B QDs, the values of the diamagnetic shift κ are between 17 and $24 \mu\text{eV T}^{-2}$, which is larger than the reported ones [20, 29]. Larger diamagnetic shifts, for the studied NFDE QDs, are usually ascribed to the larger lateral dimensions [32]: a typical nanohole size ($\sim 65 \text{ nm}$ [22]) is larger than the droplet size ($\sim 40 \text{ nm}$ [33]) in DE-grown dots. Large lateral sizes lead to large dimensions of the wave functions in the NFDE dots, implying that the orbital angular momentum is significant.

Due to the large lateral size, the results, derived from extensive studies on g -factors in GaAs/AlGaAs quantum wells, can be applied directly to NFDE dots. Agreement between the small g_e values obtained from QDs A (B) emitting at $E = 1.58 \text{ eV}$ ($E = 1.63 \text{ eV}$) and the dependence of g_e on quantum well ground-state energy can be expected. Particularly, in QDs of type B, when g_e is very close to zero, the derived QD bandgap

energy is $E_0 = 1.62$ eV , which matches the observed band-gap energy in quantum wells with $g_{e,\parallel} \approx 0$ [48].

4.3.2 Optical Dynamic Nuclear Polarization (DNP)

Since the electron spin system is coupled to the nuclear spin environment through the hyperfine interaction, angular momentum is transferred from one to the other. In addition, the nuclear spins interact with the environment, resulting in a dynamical equilibrium. In order to understand more about the properties of nuclear spin system and establish a net nuclear polarization, circularly polarized excitation and PL emission analysis are used for manipulating and monitoring the spin polarization of the nuclei in a single QD. Nuclear spin polarization can be detected by measuring the electronic energy shift of the QD emission line due to the polarized nuclei, referred to as the Overhauser Shift (EOHS). Electron Zeeman splitting in a single QD can be induced by both external magnetic fields and nuclear magnetic fields (referred to as Overhauser field). The total electron Zeeman splitting of the emission lines can be written as:

$$\Delta E^Z = g_e \mu_B (B_{\text{ext}} + B_{\text{nuc}}) \quad (4.3)$$

where g_e is the electron g -factor, μ_B is the Bohr magneton, B_{ext} and B_{nuc} are the magnetic field projection along the z -axis due to the external magnetic field and spin polarized nuclei, respectively.

When excited by linearly polarized light, electrons in the QD are in a superposition of spin up $|\uparrow\rangle$ and spin down $|\downarrow\rangle$, leading to zero Overhauser field ($B_{\text{nuc}} = 0$). The total electron Zeeman splitting thus amounts to:

$$\Delta E^{Z,\text{lin}} = g_e \mu_B B_{\text{ext}} \quad (4.4)$$

Thus, the deviation of Eq.(4.3) and Eq.(4.4) gives a direct measure of the Overhauser shift E_{OHS} and the effective nuclear magnetic fields B_{nuc} .

$$E_{\text{OHS}} = \Delta E^{Z,\sigma^\pm} - \Delta E^{Z,\text{lin}} = g_e \mu_B B_{\text{nuc}} \quad (4.5)$$

Alternatively, E_{OHS} can be calculated without measuring $\Delta E^{Z,lin}$ in external magnetic field. Circularly polarized pump laser (σ^+ or σ^- excitation) is used to polarize the nuclei. Electrons are excited by the linearly polarized probe laser after a sufficient time delay. The electronic energy shift of the QD emission line due to the polarized nuclei is detected. E_{OHS} is extracted from the changing of splitting (Eq. (4.6)) as explained in Figure 4.7.

$$E_{OHS} = \frac{\Delta E^{Z,\sigma^+} - \Delta E^{Z,\sigma^-}}{2} \quad (4.6)$$

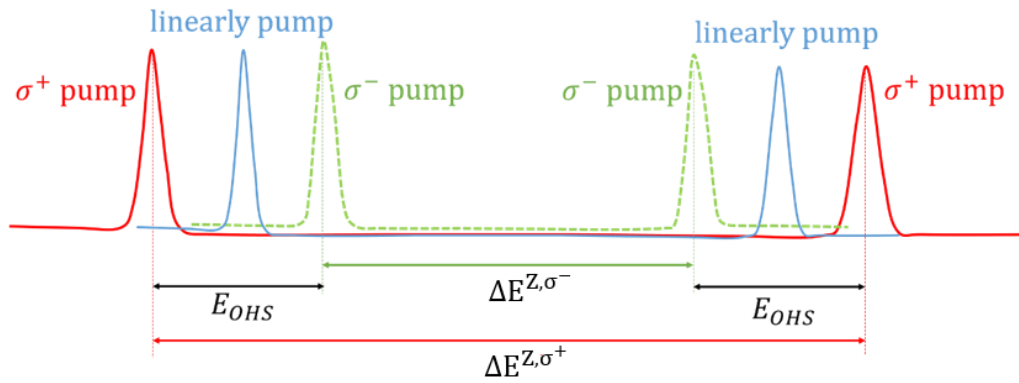


Figure 4.7: Schematic diagram showing how the Overhauser shift can be determined by using a pump-probe experimental method. $\Delta E^{Z,\sigma^+}$ is the splitting under σ^+ polarized pump laser (red solid spectrum); $\Delta E^{Z,\sigma^-}$ is the splitting under σ^- polarized pump laser (green dashed spectrum). The blue spectrum indicates the typical Zeeman splitting under external magnetic field without the impact from the effective nuclear field. E_{OHS} is extracted from the change of the splitting $\Delta E^{Z,\sigma^+} - \Delta E^{Z,\sigma^-}$.

The maximum Overhauser shift, reported in natural GaAs QDs with 60.1%/39.1% abundance of $^{69}Ga / ^{71}Ga$ is $E_{OHS}^{max} = I(A^{(^{75}As)} + 0.601A^{(^{69}Ga)} + 0.399A^{(^{71}Ga)}) \approx 137 \mu\text{eV}$, where $A^{(^{75}As)} \approx 43 \mu\text{eV}$, $A^{(^{71}Ga)} \approx 48 \mu\text{eV}$, and $A^{(^{69}Ga)} \approx 37 \mu\text{eV}$ [47] are the corresponding isotopic hyperfine coupling constants, depending on the value of the

electron Bloch function, with a nuclear spin $I = \frac{3}{2}$. The degree of nuclear spin polarization is defined as $\delta_N = \frac{E_{OHS}}{E_{OHS}^{max}}$, where δ_N is in the range of $[-1, 1]$.

Since the Overhauser shift is the physical quantity used to estimate the degree of nuclear spin polarization, it is essential to experimentally measure the EOHs induced in QDs. The measurements of nuclear magnetic resonance (NMR), dynamic nuclear polarization (DNP), and nuclear spin decay, presented in this chapter, are performed by “pump-probe” experimental method [27, 34]. Every single spectrum is the result of a few pump-probe cycles; and a linearly polarized laser, referred as the erase laser, is applied to create depolarized nuclear spins before each pump-probe cycle (see Figure 4.8). The t_{erase} is kept at 3.5 s in this measurement. Circularly polarized optical excitation with a high power pump pulse can be used to dynamically polarize the nuclear spins in the QD. The optical excitation power is 500 μ W, which is 10 times more than the saturation power of the ground-state emission. In order to build a saturated and steady nuclear polarization state initially, the duration of pumping t_{pump} should be sufficiently long to induce DNP. The nuclear spin buildup time $t_{buildup}$ can be revealed using exponential fitting in Figure 4.8; whereas the pump duration applied in the measurements is 5-7 s, which is much longer than the $t_{buildup}$ and almost maximizes the degree of nuclear spin polarization. In earlier reports, the time to build up nuclear spin were: few milliseconds in self-assembled GaAs/InAs dots under applied magnetic field $B = 0-1$ T [35, 36]; few seconds in GaAs/AlGaAs fluctuation dots at $B = 1-2$ T [37, 38]; and few seconds in InP/GaInP when the applied magnetic field was over 2 T [30]. The nuclear spin buildup time presented in this study (in NFDE GaAs/AlGaAs QDs) is similar to the one reported in droplet epitaxial grown GaAs/AlAs QDs ($t_{buildup} = 600$ ms at $B = 2.5$ T) [19].

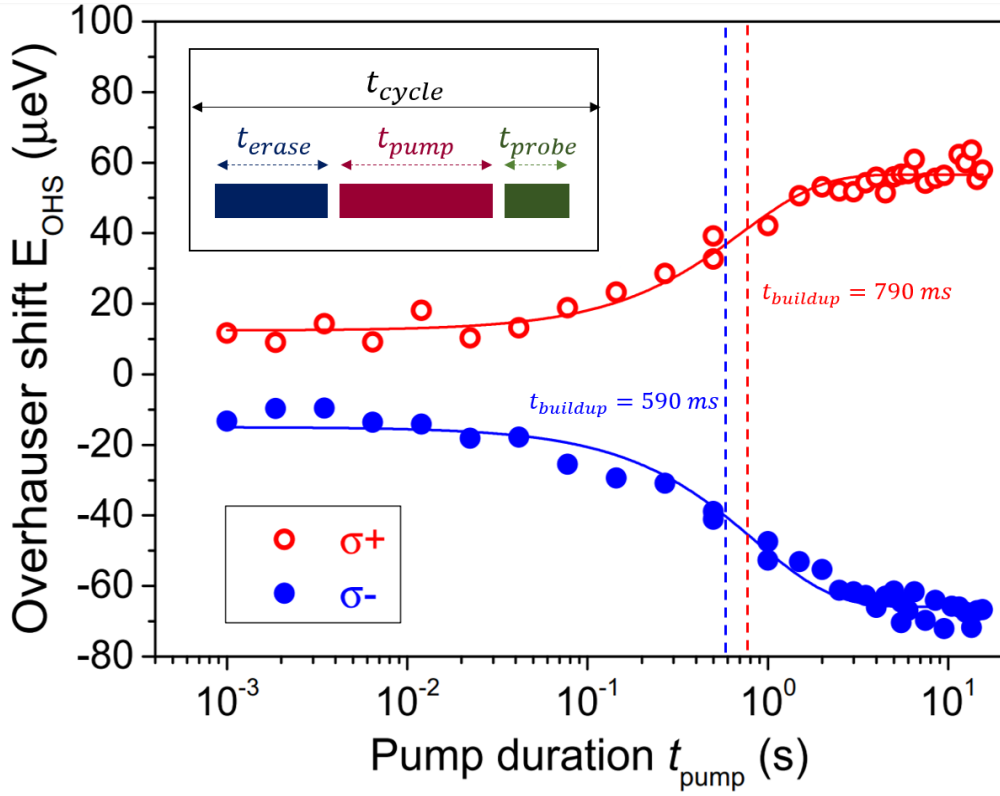


Figure 4.8: Establishment of the optically induced nuclear spin polarization dynamics. The Overhauser shift E_{OHS} of QD depends on the pump pulse duration (t_{pump}) under σ^+ (red open circles) and σ^- (blue solid circles) polarization at $B = 6$ T. Each red or blue data point is extracted from a spectrum obtained during one erase-pump-probe cycle (t_{cycle}) shown in the inset. The solid curves are the exponential fitting of the data points. The red and blue dashed lines indicate nuclear spin buildup times 790 ms and 590 ms for σ^+ and σ^- pumping, respectively.

In III-V compounds, GaAs in particular, the nuclear spin relaxation time T_1 is on the order of 1,000 s for Ga and As at a low temperature ~ 4 K [39]; while the typical T_1 -time of electron in QDs can be extended up to 1 s in a moderate magnetic field due to the spin-orbit interaction [40]. A time delay Δt , sufficiently longer than electron T_1 , should be introduced before the optical probe process. The probe pulse is linearly polarized, which can cause the nuclear depolarization. In order to keep the probe-induced nuclear depolarization degree within 3%, probe pulse duration t_{probe} varies with individual QD,

and probe excitation power should be sufficiently low. Here, in the measurements, probe duration is fixed at $t_{probe} = 50 \text{ ms}$ and probe excitation power is 0.2-0.3 times of the saturation power of the ground-state emission. To keep depolarization duration t_{erase} and probe duration t_{probe} constant in the pump-probe cycles, the duration of pump process varies (5-7 s, as mentioned above).

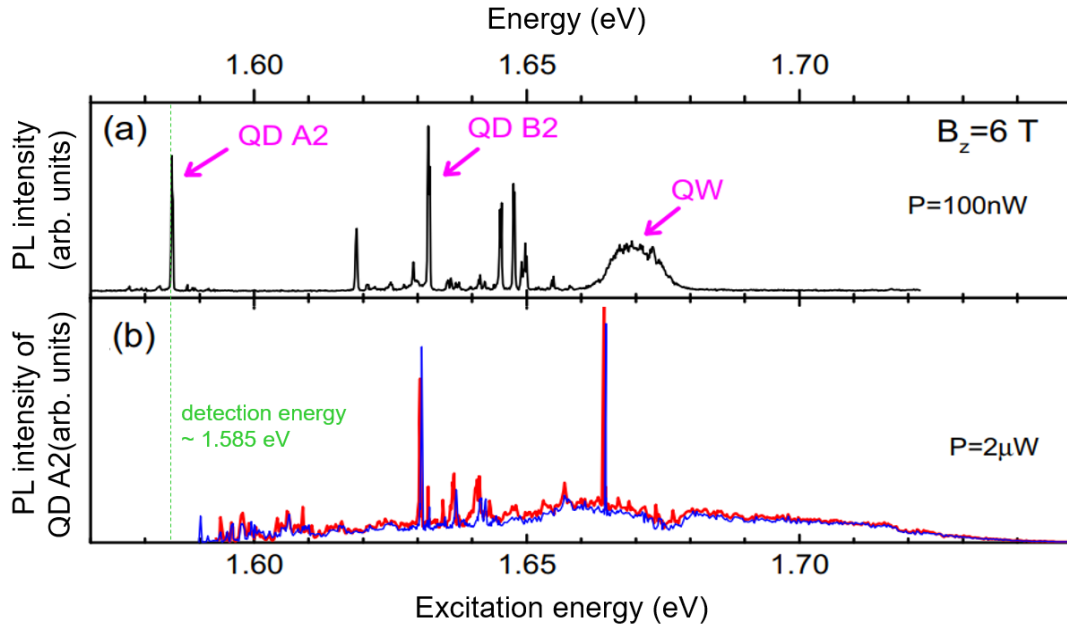


Figure 4.9: (a) Wide range PL spectrum showing the quantum well (QW), QD A2 and QD B2 emission under non-resonant excitation $E = 1.96 \text{ eV}$; (b) Photoluminescence excitation (PLE) measurements are performed on QD A2. PL emission intensity of QD A2 are measured as a function of the excitation laser E_{laser} under σ^+ (red line) and σ^- (blue line) excitation.

In order to investigate the dynamic nuclear polarization (DNP) of NFDE QDs, optical pumping has been applied to the dependence of the excitation laser energy. Figure 4.9(a) shows a wide range PL spectrum, where QD A2, QD B2 and QW emissions can be identified clearly under nonresonant excitation with laser excitation energy $E_{laser} = 1.96 \text{ eV}$, excitation power $P = 100 \text{ nW}$, and magnetic field $B = 6 \text{ T}$. Photoluminescence excitation (PLE) is a specific and useful experimental tool for investigating the energy

level structure of the material. The energy of the excitation is varied while the luminescence is detected at the typical emission energy of the QD being studied in the PLE measurements. A typical photoluminescence excitation (PLE) spectrum is plotted in Figure 4.9(b). The PL intensity of QD A2 was detected by CCD with a fixed energy of 1.585 eV (ground state energy of QD A2) when the excitation laser was scanning from 1.57 to 1.75 eV. Both of the σ^+ (red line) and σ^- (blue line) circular polarizations were applied for excitation at low optical power of 2 uW. Peaks can be observed in the region of 1.59 – 1.61 eV, which is ~ 25 meV above the energy of ground state ($E = 1.585$ eV). In PLE spectra, peaks often represent absorption lines of the material; here, these peaks are ascribed to the excited states of QD A2. As discussed in the previous section, the large lateral size causes some QW-like properties with 3D confinement effects. High density of energy levels of the excited states can be expected, resulting in a continuous broad background.

Additional to PLE spectroscopy, the nuclear polarization E_{OHS} is recorded as a function of the energy of the excitation laser E_{laser} in Figure 5.0. The red and blue lines show the Overhauser shift measured on QD A2 under σ^+ and σ^- polarized optical excitation, respectively. The measurements were performed by the “pump-probe” techniques as described above with an excitation power of 500 μ W. It can be seen that DNP emerges as the E_{laser} is over the bandgap of QD A2. The highest E_{OHS} value of 70 μ eV can be achieved at $E_{laser} = 1.675$ eV, corresponding to the QW states. Sharp peaks, observed between 1.585-1.60 eV, reflects circularly and resonant pumping of either the ground state or excited states of QD A2. This mechanism has been studied in self-assembled QDs [41, 42]. Similar to the PLE spectrum in Figure 4.9 (b), a nearly continuum spectrum between 1.61-1.63 eV is attributed to the excited stated due to the large lateral dimensions of the NFDE QDs. In the region of 1.63-1.66 eV, a series of sharp peaks is observed, where both PL and PLE signal of type B QDs show correlated peaks. Particularly, the peaks produced by QD B2 at 1.63 eV under resonantly optical excitation, indicates that DNP in type A dot can be induced by type B dot under optical excitation. Previous studies have not reported this mechanism, which is such a unique property of NFDE QDs.

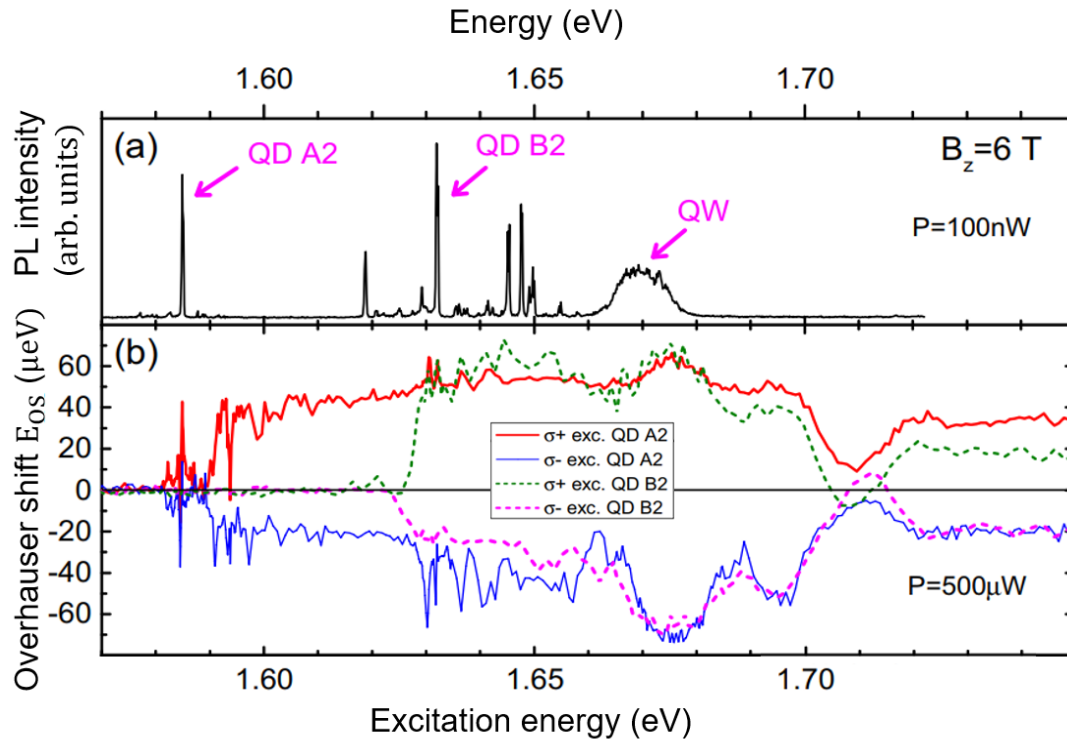


Figure 4.10: (a) Wide range PL spectrum showing the quantum well (QW), QD A2 and QD B2 emission under nonresonant excitation $E = 1.96$ eV as shown in Figure 4.9(a); (b) Overhauser shift measured on QD A2 and QD B2 as a function of the energy of excitation laser E_{laser} . Red and blue lines are for QD A2 under σ^+ and σ^- excitation, respectively; green and magenta lines are for QD B2 under σ^+ and σ^- excitation, respectively.

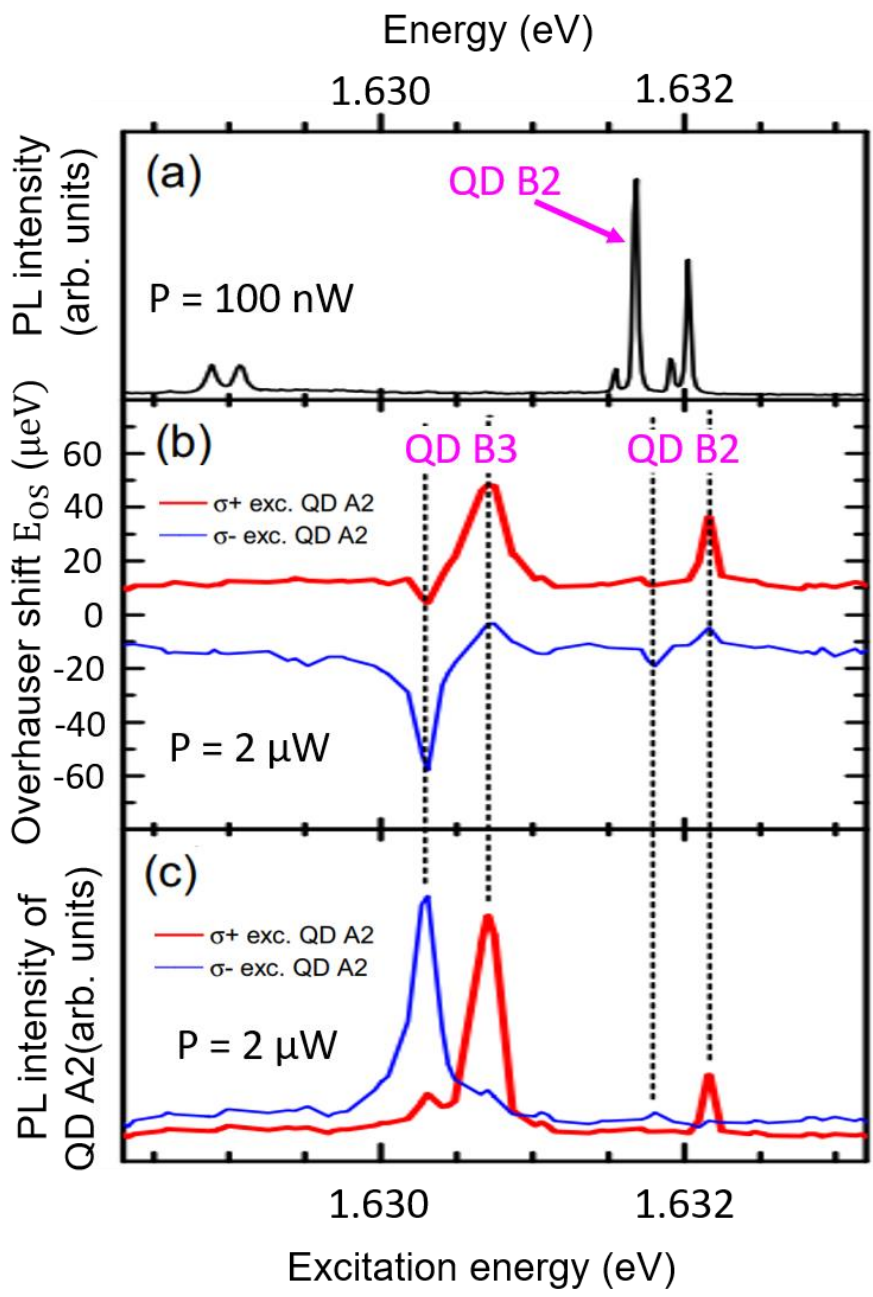


Figure 4.11: Higher resolution photoluminescence spectra focusing on QD B2, B3 and A2. (a) PL spectrum of QD B2. (b) DNP measurement of QD A2 when E_{laser} is scanned close to the resonance of QD B2 by low power excitation. (c) PLE spectra of QD A2: a close-up of Figure 4.8(b).

In order to understand more details about the inter-dot DNP process, higher resolution spectroscopy has been performed focusing around the ground state of QD B2. PL spectrum of QD B2 can be found in Figure 4.11(a). DNP measurement of QD A2 was detected when E_{laser} is scanned close to the resonance of QD B2 by low power excitation as shown in Figure 4.11(b). Black dashed lines in Figure 4.11 point direct correspondences between the peaks in the DNP (Figure 4.11(b)) and PLE (Figure 4.11(c)) spectra, indicating that the DNP in QD A2 is induced by the resonant optical electron-hole injection mechanism. A doublet occurs near 1.632 eV in both of the DNP and PLE spectra due to the Zeeman effect under circularly polarized excitation and external magnetic field ($B = 6$ T). However, there is a small mismatch: the PL peaks of QD B2 in Figure 4.11(a) are red-shifted by 150 μ eV comparing with the corresponding DNP and PLE peaks in Figure 4.11(b) and (c). This red-shift can be a result of Coulomb shift [43]. In PL measurements, the existing exciton in QD A2 interacts with the exciton tunneling from QD B2, resulting in a red-shift of the ground-state emission of QD B2. By contrast, in PLE measurements of QD A2, ground-state exciton emission of QD A2 is measured and photon absorption in QD B2 happens when there is no exciton occupying in QD A2. Under resonant excitation, an exciton generated in QD B2 can tunnel into QD A2 and recombine. The PLE peak in Figure 4.11(c) is a result of the exciton recombination. During the process of exciton tunneling or recombining, the spin of the exciton electron from QD B2 can be exchanged with nuclei in QD A2, leading to a DNP peak in Figure 4.11(b).

As can be noticed obviously, prominent DNP and PLE doublets are observed at 1.630 eV in Figure 4.11(b) and (c), respectively. However, there is no PL emission in Figure 4.11(a) to relate to them. In order to understand this phenomenon, assume that a QD, denoted as QD B3, exists and has a much greater tunneling rate than QD B2. Therefore, excitons from QD B3 tunnel into QD A2 before electrons and holes can recombine in QD B3, resulting in an enhancement of the PL and DNP in QD A2 while a suppression of PL emission in QD B3.

Additionally, the same measurements (DNP) have been performed on QD B2 (green line for sigma plus and magenta line for sigma plus excitation). However, there is no Overhauser shift detected in QD B2 when exciting QD A2 due to the band structure of

type A and B dots. Based on the above spectral analysis of Figure 4.11 and the previous AFM studies [22], a most likely schematic cross-section structure of the sample and the corresponding band structure are displayed in Figure 4.12(a) [49] and (b), respectively. QDs of type A are formed as nanohole filling, while the “mounds” are formed at the edge of the nanohole, creating 3D confinement in additional spots, defined as QDs B. The potential well of QD B type is much shallower than that in type A dots, and thus the excitons generated in QD B under resonant excitation can tunnel into QD A and recombine (This process results in a PLE peak in Figure 4.11(c)). Furthermore, it is also possible that the exciton electron can exchange its spin with a nucleus either during exciton tunneling into QD A or during recombination in QD A (this results in a DNP peak in Figure 4.11(b)). The above analysis also suggests that the nuclear spin diffusion between dots can be neglected and the DNP in QD of type A can be induced by another QD of type B using optical excitation, which has not been reported in previous studies and can be unique to the NFDE QDs.

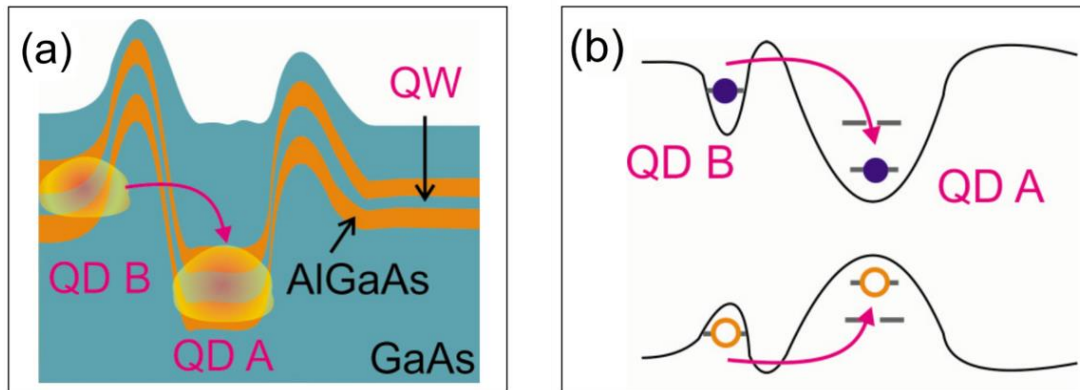


Figure 4.12 (a) Schematic diagram of sample cross section and formation of type A QDs and type B QDs [22,49]; (b) Schematic energy band structure of type A QD and type B QD.

In order to investigate the reproducibility of DNP in NFDE QDs, a series of pump-probe measurements were performed on several dots from the same sample. The results presented in Figure 4.13 show contour maps of Overhauser shift in the parameter space of excitation laser power and magnetic field for QD A7 under σ^+ and

σ^- excitation. A cw pump laser at 1.642 eV is used to build up the nuclear spin by tuning in resonance with a type B dot. At high powers ($P > 10 \mu\text{W}$), DNP can be produced in a wide range of external magnetic fields for both σ^+ and σ^- excitation. The maximum Overhauser shifts achieved for this dot is 65 μeV at $B = 8-9 \text{ T}$ under σ^+ excitation, while -55 μeV at $B = 3 \text{ T}$ under σ^- excitation.

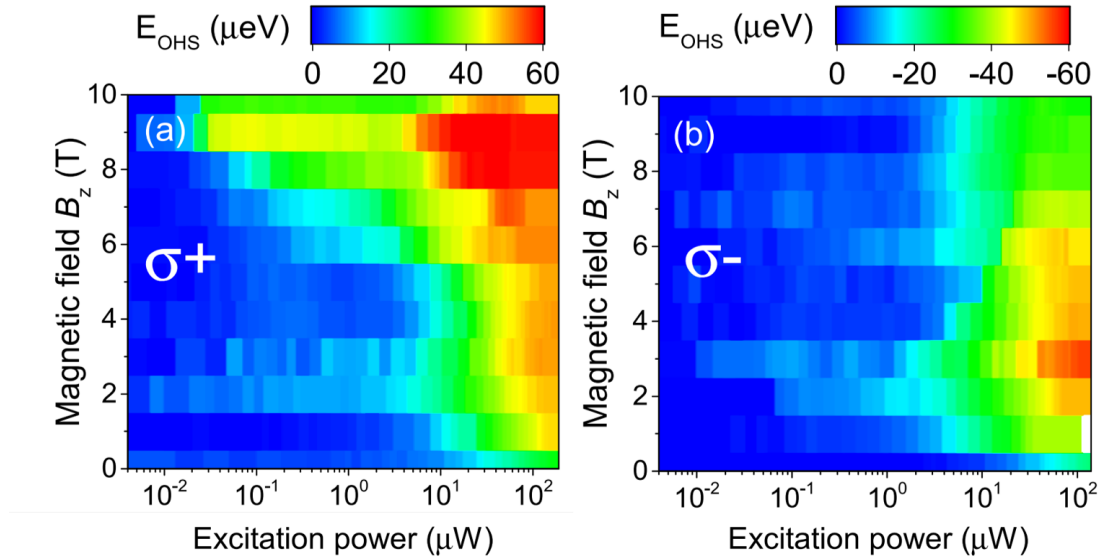


Figure 4.13: 3D contour plots of the Overhauser shift E_{OHS} as excitation power P_{exc} and magnetic field B_z vary under σ^+ (a) and σ^- (b) excitation for QD A7. The colour scheme bar on the top of each plot is a depiction of the corresponding scale of E_{OHS} .

As can be noticed obviously in Figure 4.13(a), under high magnetic field $B = 9 \text{ T}$, a significant Overhauser shift with a value of 50 μeV is detected even when the σ^+ excitation power is down to 50 nW. Such low-power DNP has been ascribed to the recombination of the long-lived dark excitons via second-order process involving a nuclear spin flip in neutral QDs in other materials according to previous report [29, 44]. By contrast, there is no low-power DNP under σ^- excitation, and the maximum Overhauser shift appears at $B = 3 \text{ T}$. In Figure 4.13, it is found that the DNP can be induced efficiently at magnetic field B_z as small as 0.5 T.

After examining several other dots on the same sample, a net, well reproduced results can be achieved similarly as those presented in Figure 4.9 and Figure 4.10. DNP via

optical pumping the QW states and DNP via tunneling from type B dots to type A dots are larger than that induced via pumping type A dots resonantly, with values of 85 μeV and 50 μeV , respectively. However, interdot tunneling mechanism provides a selective way to control the nuclear polarization in QDs individually, while the nuclei in all dots can be polarized under nonresonant pumping as long as the dots are covered by the laser spot. The key factor of governing the DNP process is to make the electron-nuclear spin flip-flop inefficient by keeping excitation the Zeeman energy much larger than the nuclear Zeeman energy.

4.3.3 Nuclear Magnetic Resonance (NMR) Spectroscopy: Probing Quantum Dot Internal Structure

According to quantum mechanics, nuclear spin “ I ” represents the total angular momentum of a nucleus and depends on the mass number (A). Half-integer spins result from odd mass numbers; while integer spins correspond to even mass numbers. Nuclear spin angular momentum exists in $2 * I + 1$ distinct quantum states possessing different orientations in an externally applied static magnetic field. The spin projections parallel to the field has values m running from $-I$ to I in steps of unity. Here, in this measurement, for ^{75}As spin $I = \frac{3}{2}$, m takes the values $-\frac{3}{2}, -\frac{1}{2}, +\frac{1}{2}, +\frac{3}{2}$ (see Figure 4.14).

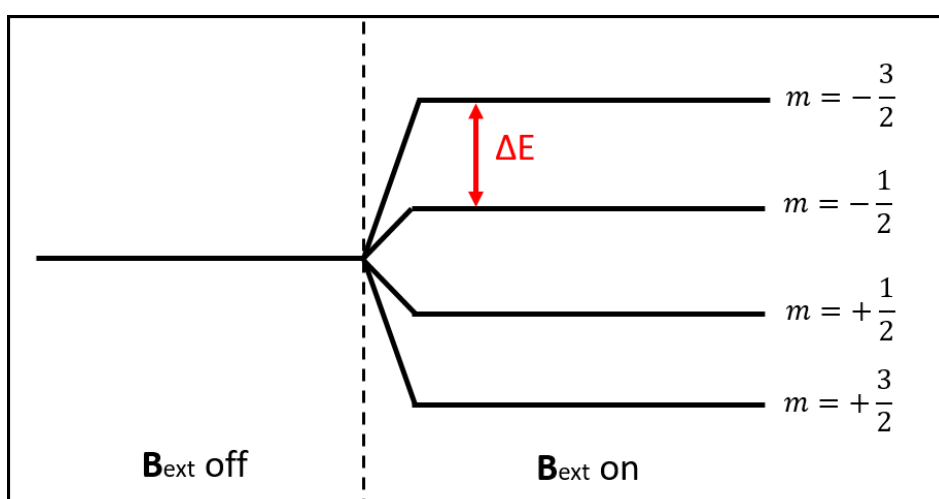


Figure 4.14: Energy levels for a ^{75}As nuclear spin of $I = \frac{3}{2}$ in a magnetic field B .

Nuclear spins can be polarized (aligned) based on the ability to induce efficient and large DNP as discussed in previous measurements. Nuclear magnetic moment, arising from the spin of the nuclei, is in the same direction as nuclear spin and proportional to the angular momentum of a nucleus. When placed in an external magnetic field, the nuclear magnetic moment can move like a gyroscope with a certain frequency around the external magnetic field. Such motion is called Larmor precession. The frequency of the precession is referred to as Larmor frequency, determined by external magnetic field, nuclear magnetic moment, and the angle between them. The angle formed by external magnetic field and nuclear magnetic moment directions depends on the magnetic quantum number m . The energy level of the m_{th} state is

$$E_m = -\gamma m \hbar B \quad (4.7)$$

Where γ is the nuclear magnetogyric ration and $\gamma = \frac{g_I e}{2m_p}$ (g_I is the nuclear g -factor; m_p is the mass of proton). So the energy difference between adjacent states is given by

$$\Delta E = \gamma \hbar B \quad (4.8)$$

According to Einstein relation $\Delta E = \hbar \omega$, transitions occurs when the applied radiation has an angular frequency ω of

$$\omega = \gamma B. \quad (4.9)$$

The resonance transition condition, Eq. (4.9), indicates γ is an important constant. It varies for different nuclei. Usually, the perturbation inducing transitions in NMR lies in the RF (radio-frequency) range (10^6 - 10^9 Hz.)

NMR measurements are performed using “pump-probe” technique (similar to the method discussed in Section 4.3.2) with a radio frequency (RF) pulse introduced between the pump and probe duration. RF pulse differs for different nuclei. The Overhauser shift, induced by transitions between the spin states, can be detect by probe spectrum. Here, in this experiment, the duration of the RF probe is about 150 ms.

Nuclear magnetic resonance spectroscopy is a powerful spectroscopic tool for investigating the local magnetic field induced by transitions between the nuclear spin states. NMR spectra is a well-resolved, analytically tractable, highly predictable and unique method to identify small molecules, providing specific information about the

reaction states, structure of the material, dynamics, monomolecular organic compounds, and chemical environment of molecules [45]. However, any nucleus with a non-spherical charge distribution has a nuclear electric quadrupole moment. Energy levels split by a magnetic field are shifted unequally due to the quadrupole moment interacts with local electric field gradient (EFG) created by the non-uniform distribution of electron density or/and the bonding environment of the nuclei, see in Figure 4.15. In analogy with NMR, a perturbation of nuclear quadrupole energy levels occurs when an oscillating RF electromagnetic radiation is applied whose frequency closely matches the precession frequency. The quadrupolar shift, due to the transitions between the quadrupole energy levels, can be expected in the measurements. NMR investigations in semiconductor nanostructures are restricted largely by the quadrupole-induced broad spectra.

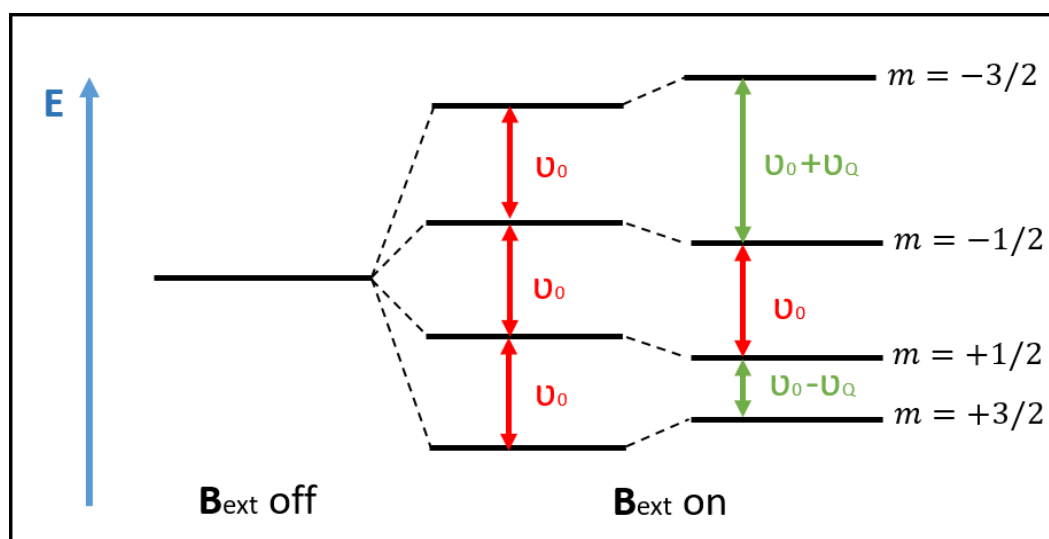


Figure 4.15: Energy levels for a ^{75}As nuclear spin of $I = \frac{3}{2}$ in a magnetic field B and the local electric field gradient (EFG) created by the non-uniform distribution of electron density or/and the bonding environment of the nuclei.

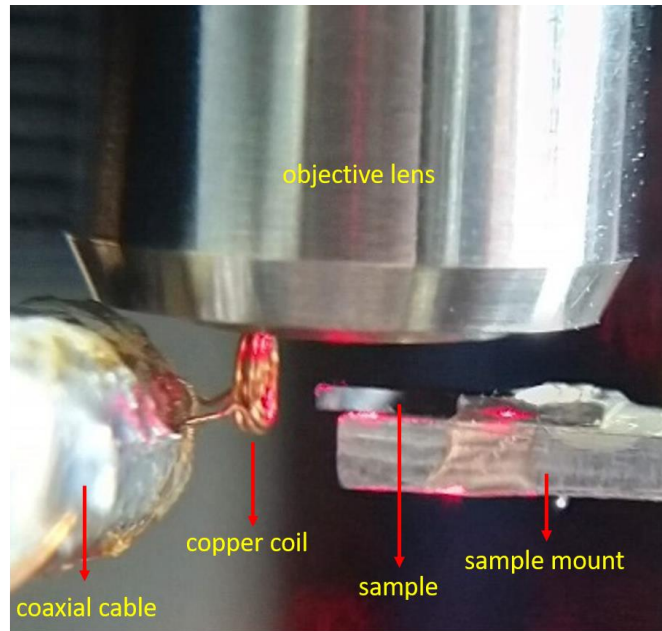


Figure 4.16: A close-up of the sample mount inside the cryostat. The multi-layer copper coil (the hole in the middle of the coil is ~ 0.4 mm) is soldered to a coaxial cable and placed close to the sample to provide the RF excitation in NMR measurements.

As shown in Figure 4.16, the sample is fixed on an aluminium mount and can be controlled by a set of three spatial dimensional piezo stages. The multi-layer copper coil (the hole in the middle of the coil is ~ 0.4 mm) is soldered to a coaxial cable and placed close to the sample to provide the RF excitation in NMR measurements. The RF excitation itself is created by a waveform generator and passed through an RF amplifier before reaching the coil. In order to study the structural properties of the QD, an optically detected “inverse” NMR spectroscopy method, developed by Dr. Evgeny Chekhovich, is utilised. The improvement of the “inverse” NMR, based on the typical NMR measurements, is that a continuum broadband RF excitation replaces the FR pulse. The excitation RF in “inverse” NMR contains a gap with a width f_{gap} (see Figure 4.17(b)), which is selected to balance the signal amplitude and the spectral resolution. Full details about the inverse NMR method can be found in the reference [27].

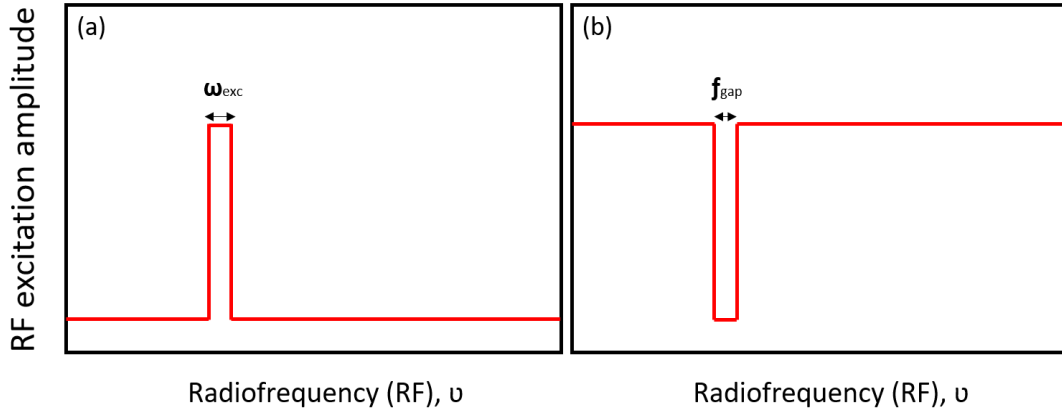


Figure 4.17: Schematic diagram of the radiofrequency excitation spectra for the typical saturation spectroscopy method (a) and the improved 'inverse' spectroscopy (b).

As can be noticed, the radiofrequency excitation spectrum in Figure 4.17(b) is the inversion of that in Figure 4.17(a). Narrow-band and broadband excitation is the main difference between the typical saturation spectroscopy (Figure 4.17(a)) and 'inverse' spectroscopy (Figure 4.17(b)). The effect of excitation on the population probability P_{I_m} is significant. The population distribution follows the Boltzman distribution [27] under narrow-band excitation, while under the 'inverse' broadband excitation, the population probabilities of the nuclear spin levels can be built to enhance the transitions in the nuclear spectra corresponding to the spin states coupled by the RF field [27]. The RF pulse duration in this measurement was 1.2 s long and $f_{\text{gap}} = 400$ kHz.

The nuclear spin polarization (quantified by the total Overhauser shift E_{OHS}) includes contributions from all the isotopes within the QD (Al, Ga, As and Ga). The contributions can be separated individually by selectively depolarizing each isotope after fully build up the optical DNP. Resonant RF excitation measurements were performed to erase the polarization of As at $B = 6$ T in this work. The NMR spectra of the ^{75}As isotope for QDs A4 and QDs B4 are shown in Figure 4.18(a) and (b), respectively. The NMR signal is detected optically and is the subtraction between the total Overhauser shift E_{OHS} and the Overhauser shift $E_{\text{OHS}(\text{rf})}$ measured with RF depolarizing the ^{75}As isotope. Red dotted lines and blue solid lines are measured under σ^+ and σ^- optical nuclear spin pumping, respectively. Sharp central peak dominating in both Figure 4.18(a) and (b)

corresponds to the central transitions (CTs) between nuclear spin $-\frac{1}{2} \leftrightarrow +\frac{1}{2}$. Quadrupolar shift transitions, defined as satellite transitions (STs), are expected to be measured as discussed above. The two STs correspond to nuclear spin $+\frac{1}{2} \leftrightarrow +\frac{3}{2}$ and $-\frac{3}{2} \leftrightarrow -\frac{1}{2}$, shifting from CT by $+v_Q$ and $-v_Q$, respectively. The nonzero quadrupolar shift v_Q (sidebands) indicates the existence of shear elastic strain [19] although lattice mismatch is not expected in GaAs/AlGaAs structures. Asymmetric STs can be observed in QD A4 and QD B4 under σ^+ optical pumping.

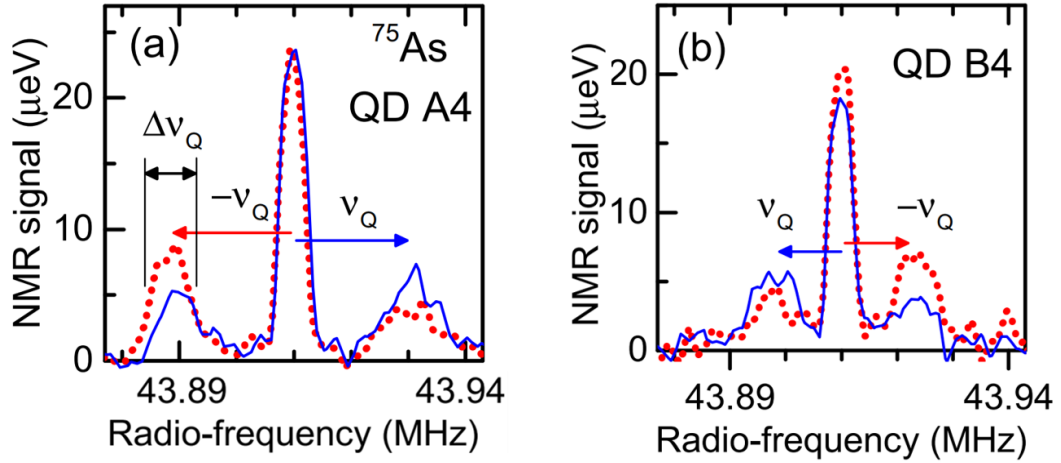


Figure 4.18: Nuclear magnetic resonance spectra of ^{75}As nuclei in QD A4 (a) and QD B4 (b) under σ^+ (red dotted line) and σ^- (blue solid line) optical pumping. The central transition (CT) is observed at $\nu \approx 43.91$ MHz. The satellite transitions (STs) are separated from the CT by the strain-induced quadrupolar shift $\pm v_Q$.

An increment of the NMR signal for the low-frequency ST of QD A4 and high-frequency ST of QD B4 can be noted due to the enhancement of the $-\frac{3}{2} \leftrightarrow -\frac{1}{2}$ ST by sigma plus light [27], which suggests that QD A4 and QD B4 have opposite signs of the quadrupolar shifts (v_Q). Figure 4.19 reveals systematic quadrupolar shift values of several individual dots: positive $v_Q \sim +20$ kHz for type A QDs and negative $v_Q \sim -10$ kHz for type B QDs, corresponding to the black squares and red rectangles, respectively. The linewidth at

half maximum of ST (Δv_Q), reflecting the inhomogeneous distribution of v_Q in the dot, varies in a range of 10-20 kHz. The average v_Q in self-assembled dots has been reported as ~ 1.15 MHz, which is almost three orders of magnitude larger than in NFDE dots.

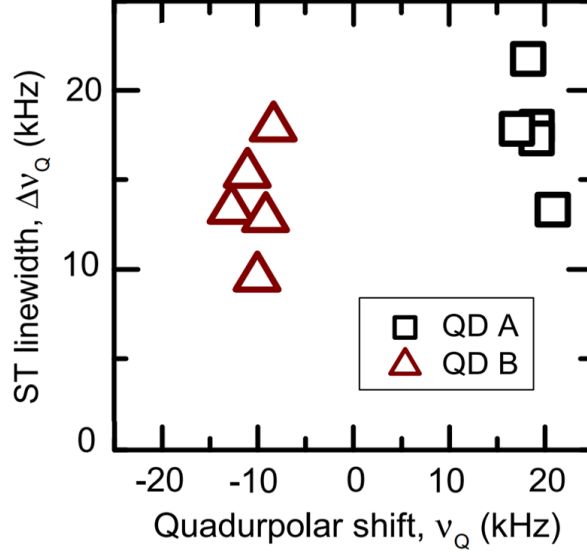


Figure 4.19: The linewidths at half maximum of STs versus the corresponding quadrupolar shifts for A (back open squares) and B (red open triangles) type of QDs.

In general, quadrupolar shifts, induced by the shear strain rather than isotropic hydrostatic strain, are related to the orientations configuration of the strain tensor axes and the magnetic field. Here, as the experimental configuration is Faraday geometry and samples are planar QD structures, the dominant contribution to the quadrupolar shifts origins from the uniaxial strain with its main axis parallel to magnetic field (along Oz). The strain is normally characterized with $\epsilon_b = \epsilon_{zz} - \frac{\epsilon_{xx} + \epsilon_{yy}}{2}$. When $\epsilon_b > 0$, a tensile strain is along the direction of magnetic field ($\epsilon_{zz} > 0$), but the compressive strain is perpendicular to the magnetic field ($\epsilon_{xx} < 0, \epsilon_{yy} < 0$). The quadrupolar shift induced by this deformation amounts to

$$v_Q = \frac{3eQS_{11}\epsilon_b}{2hI(2I-1)}, \quad (4.10)$$

where h is the Planck's constant, I is the spin of ^{75}As nuclei, e is the charge of electron,

Q is the quadrupolar moment of ^{75}As nuclei ($\sim 0.31 \times 10^{-28} \text{ m}^2$), and S_{11} is the gradient elastic tensor of ^{75}As in bulk GaAs ($|S_{11}| \approx 3.9 \times 10^{22} \text{ Vm}^{-2}$) with undefined sign [50]. Accordingly, the strain distribution in QDs can be derived from the ST linewidth $\Delta\nu_Q$ and the average strain can be worked out by the average quadrupolar shift ν_Q :

$$\epsilon_b = \frac{2\nu_Q h I(2I-1)}{3eQS_{11}}. \quad (4.11)$$

As discussed in Section 4.3.1, the studied NFDE QDs have large lateral sizes. Comparing with previous investigations on disk-shaped self-assembled InGaAs/GaAs QDs (large lateral sizes), the results of studies on ν_Q for ^{75}As and the tensile strain ϵ_b are applicable to NFDE dots. ν_Q is negative ($\nu_Q < 0$) and ϵ_b is positive ($\epsilon_b > 0$) in disk-shaped self-assembled InGaAs/GaAs QDs [51], indicating $S_{11} < 0$ (sign convention by Eq. (4.11)). Applying $S_{11} < 0$ ($S_{11} \approx -3.9 \times 10^{22} \text{ Vm}^{-2}$) to GaAs/AlGaAs NFDE QDs for the sign convention on ν_Q . Although the GaAs lattice constant is slightly smaller than that of AlGaAs (contrary to InGaAs/GaAs pair), ϵ_b can be roughly estimated according to disk-shaped dots. In A type of GaAs/AlGaAs QDs, positive ν_Q ($\nu_Q \approx +19 \text{ kHz}$) was measured and $\epsilon_b < 0$ was derived from Eq. (4.11) with a value of -0.0014% , corresponding to a compressive deformation along the magnetic field. However, in B type of QDs ($\nu_Q \approx -10 \text{ kHz}$, $S_{11} \approx -3.9 \times 10^{22} \text{ Vm}^{-2}$), an anomalous positive ϵ_b ($+0.007\%$) was estimated, corresponding to a tensile strain along Oz in the structure [51].

More interestingly, for the type A QDs, the values of ϵ_b are all distinctly negative whilst for the type B QDs, their ϵ_b are all distinctly positive. This implies that the wavefunction overlap between the excitons in type A and B QDs is small [27], and it is consistent with our previous deduction basing on the analysis of DNP measurements that the origin and structure of these types of QDs is different.

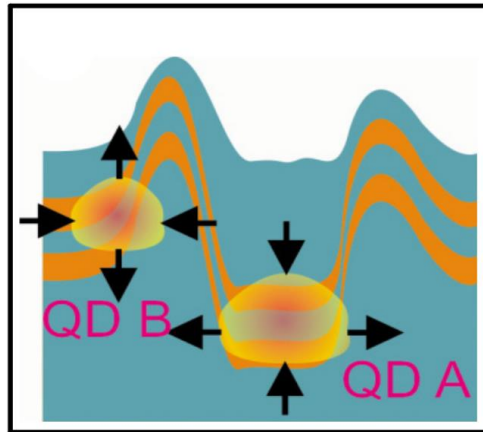


Figure 4.20: Schematic diagram of the strain profile for A type of QDs and B type of QDs. Black arrows indicate the direction of strain, deduced from the NMR spectra in Figure 4.16(a) and (b).

As discussed above, the cross sectional structure of the QDs is shown in Figure 4.12(a) and in Figure 4.20. Type A QDs are located in the nanohole whilst type B QDs form outside the moundlike edge of the nanohole due to the 3D confinement. The tensile strain along Oz observed in type B QDs is induced by the “sloped” AlGaAs barriers applying stretching force along Oz axis on the GaAs layer, whilst resulting in a compressive in-plane deformation, as illustrated by the arrows in Figure 4.20. For type A QDs, as they are located in the nanoholes, AlGaAs barriers stretch the GaAs layer in the horizontal plane inducing compressive strain along Oz ($\epsilon_b < 0$).

4.3.4 Long Nuclear Spin Relaxation Times

Nuclear spin relaxation in III-V compounds has been studied in detail by NMR measurements. Relaxation is the conversion from a non-equilibrium population (excited state) to a normal population (ground state), describing how signals deteriorate with time. The processes of relaxation in the dynamics of a spin system involve the interactions of the spin dipoles with their environment (spin-lattice) and with themselves (spin-spin). Time constant T_1 , known as spin-lattice relaxation time, characterizes the rate where the longitudinal (parallel to the B field) component of the

magnetization restores exponentially towards the thermodynamic equilibrium. Spin-spin relaxation time, known as T_2 , characterizes the signal decay of the transverse component of the magnetization. The lifetime of nuclear spin states in QDs are limited by the relaxation time by paramagnetic impurities, quadrupolar relaxation, charge fluctuations in the dots or in nearby dots and nuclear spin diffusion. In order to investigate the relaxation time in NFDE QDs, a set of measurements was performed by pump-wait-probe protocol. Figure 4.21 schematically shows the experiment cycle of the pump-wait-probe, where t_{pump} is the excitation time of the circularly polarized pump laser, t_{probe} is the detection time of the PL signals under probe laser, and Δt is the delay (dark waiting time) between pump and probe. The dark waiting time Δt is varied keeping the other parameters constant.

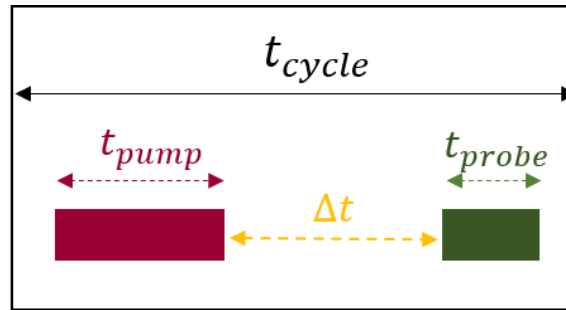


Figure 4.21: Schematic diagram of the experiment cycle of pump-wait-probe. t_{pump} is the excitation time of the circularly polarized pump laser; t_{probe} is the detection time of the PL signals under probe laser; and Δt is the delay (dark waiting time) between pump and probe.

The dependence of Overhauser shift on Δt is presented in Figure 4.22 for two individual QDs. The red open circles from QD A6 and blue full circles from QD B6 were measured under sigma plus and sigma minus excitation, respectively. The relaxation time T_1 can be obtained by the exponential fits (the red and blue solid lines in Figure 4.20): $T_1 = 7800$ s for QD A6 and $T_1 = 4900$ s for QD B6. As can be noticed in the dotted circles, some experimental data points and the exponential decay fitting diverge

significantly. Such deviation is caused by nuclear spin diffusion. These points were measured after all the other points with very long Δt (>1000 s). After repeated excitation of circularly polarized light with the same helicity, the nuclei in the surrounding environment of the QD are polarized, restraining the spin diffusion [45] and extending the relaxation time T_1 .

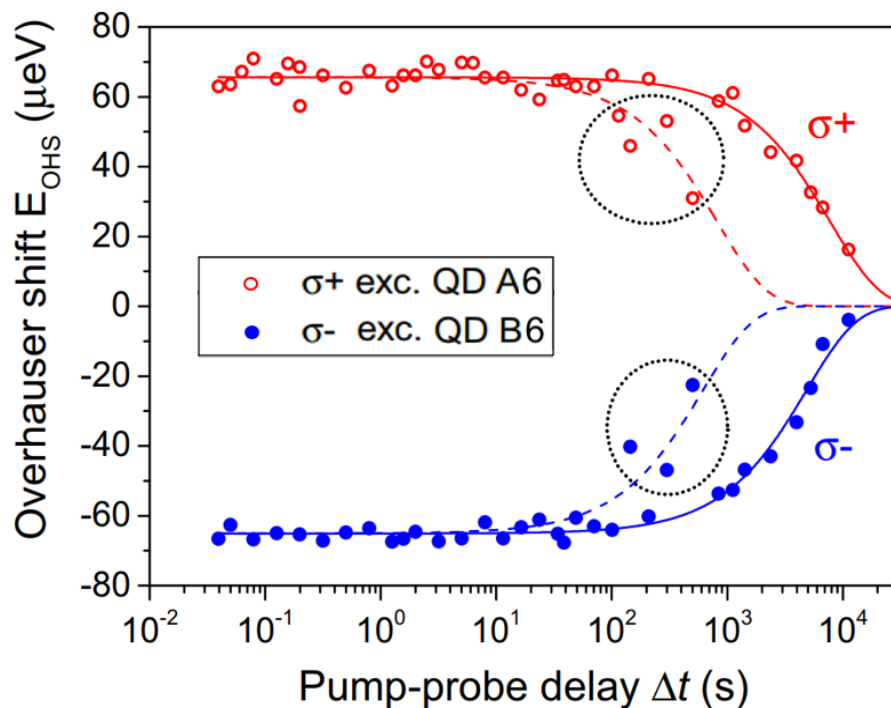


Figure 4.22: Decay dynamics of the nuclear spin polarization in the dark measured by using pump-wait-probe protocol. Overhauser shift is detected with various pump-probe delay Δt for QD A6 (red open circles) and QD B6 (blue full circles) under σ^+ and σ^- excitation, respectively. The solid lines fit exponentially to the data revealing $T_1 = 7800$ s and $T_1 = 4900$ s for QD A6 and B6, respectively. The highlighted data within circles were recorded after keeping the QD in the dark for durations >1000 s and fitted by dashed lines, revealing a much shorter decay time due to the reduction of nuclear spin diffusion effect on the subsequent pump-probe cycle with $T'_1 = 860$ s and $T_1 = 640$ s for QD A6 and B6, respectively.

In natural GaAs/AlGaAs QDs, all the nuclear spin transitions are degenerate, allowing a nuclear spin state $I = \frac{3}{2}$ to flip into a $I = \frac{1}{2}$ state and transferring the excess polarization to adjacent spin. By contrast, such a process would be suppressed due to the energy mismatch in NFDE QDs, reducing the spin exchange rate and slowing down the propagation of nuclear spin polarization into the AlGaAs barrier. As a result, the lifetime of the nuclear spin magnetization in QDs can be increased.

4.4 Summary

In conclusion, electron and nuclear spin properties of in situ nanohole-filled droplet epitaxial (NFDE) quantum dots have been explored. The close-to-zero electron g-factor for such QDs is revealed, which offers a potential route to independent control of QD spin qubits by electrodes. Optical manipulation of the nuclear spin bath is achieved with an efficient dynamic nuclear polarization degree as large as 65%. NMR (nuclear magnetic resonance) spectroscopy reveals the internal structural properties of NFDE quantum dots, together with the direction and magnitude of strain. The nuclear spin system of NFDE dots demonstrate a very long nuclear spin lifetimes, which are comparable to those reported previously in self-assembled InP [52] and InGaAs [53] dots.

- [1] B. Urbaszek, X. Marie, T. Amand, O. Krebs, P. Voisin, P. Maletinsky, A. Hoegele, and A. Imamoglu, *Rev. Mod. Phys.* 85, 79 (2013).
- [2] O. Gywat, H. J. Krenner, and J. Berezovsky, *Spins in Optically Active Quantum Dots*, 1st ed., Wiley-VCH, Weinheim (2010).
- [3] D. Press, K. De Greve, P. L. McMahon, T. D. Ladd, B. Friess, C. Schneider, M. Kamp, S. Hofling, A. Forchel, and Y. Yamamoto, *Nat. Photon.* 4, 367 (2010).
- [4] K. De Greve, P. L. McMahon, D. Press, T. D. Ladd, D. Bisping, C. Schneider, M. Kamp, L. Worschech, S. Hofling, A. Forchel, and Y. Yamamoto, *Nat. Phys.* 7, 872 (2011).
- [5] T. M. Godden, J. H. Quilter, A. J. Ramsay, Y. Wu, P. Brereton, S. J. Boyle, I. J. Luxmoore, J. Puebla-Nunez, A. M. Fox, and M. S. Skolnick, *Phys. Rev. Lett.* 108, 017402 (2012).
- [6] A. V. Khaetskii, D. Loss, and L. Glazman, *Phys. Rev. Lett.* 88, 186802 (2002).
- [7] I. A. Merkulov, A. L. Efros, and M. Rosen, *Phys. Rev. B* 65, 205309 (2002).
- [8] E. A. Chekhovich, M. N. Makhonin, A. I. Tartakovskii, A. Yacoby, H. Bluhm, K. C. Nowack, and L. M. K. Vandersypen, *Nat. Mater.* 12, 494 (2013).
- [9] W. A. Coish and D. Loss, *Phys. Rev. B* 70, 195340 (2004).
- [10] A. S. Bracker, E. A. Stinaff, D. Gammon, M. E. Ware, J. G. Tischler, A. Shabaev, A. L. Efros, D. Park, D. Gershoni, V. L. Korenev, and I. A. Merkulov, *Phys. Rev. Lett.* 94, 047402 (2005).
- [11] B. Urbaszek, P.-F. Braun, T. Amand, O. Krebs, T. Belhadj, A. Lemaitre, P. Voisin, and X. Marie, *Phys. Rev. B* 76, 201301 (2007).
- [12] D. J. Reilly, J. M. Taylor, J. R. Petta, C. M. Marcus, M. P. Hanson, and A. C. Gossard, *Science* 321, 817 (2008).
- [13] M. Issler, E. M. Kessler, G. Giedke, S. Yelin, I. Cirac, M. D. Lukin, and A. Imamoglu, *Phys. Rev. Lett.* 105, 267202 (2010).
- [14] A. Bechtold, D. Rauch, F. Li, T. Simmet, P.-L. Ardel, A. Regler, K. Muller, N. A. Sinitsyn, and J. J. Finley, *Nat. Phys.* 11, 1005 (2015).

- [15] R. Stockill, C. Le Gall, C. Matthiesen, L. Huthmacher, E. Clarke, M. Hugues, and M. Atature, arXiv:1512.01811.
- [16] Y. Kato, R. C. Myers, D. C. Driscoll, A. C. Gossard, J. Levy, and D. D. Awschalom, *Science* 299, 1201 (2003).
- [17] J. Pingenot, C. E. Pryor, and M. E. Flatte, *Appl. Phys. Lett.* 92, 222502 (2008).
- [18] J. Pingenot, C. E. Pryor, and M. E. Flatte, *Phys. Rev. B* 84, 195403 (2011).
- [19] T. Belhadj, T. Kuroda, C.-M. Simon, T. Amand, T. Mano, K. Sakoda, N. Koguchi, X. Marie, and B. Urbaszek, *Phys. Rev. B* 78, 205325 (2008).
- [20] M. Abbarchi, T. Kuroda, T. Mano, K. Sakoda, and M. Gurioli, *Phys. Rev. B* 81, 035334 (2010).
- [21] G. Sallen, S. Kunz, T. Amand, L. Bouet, T. Kuroda, T. Mano, D. Paget, O. Krebs, X. Marie, K. Sakoda, and B. Urbaszek, *Nat. Commun.* 5, 3268 (2014).
- [22] P. Atkinson, E. Zallo, and O. G. Schmidt, *J. Appl. Phys.* 112, 054303 (2012).
- [23] Y. H. Huo, A. Rastelli, and O. G. Schmidt, *Appl. Phys. Lett.* 102, 152105 (2013).
- [24] W. B. Gao, A. Imamoglu, H. Bernien, and R. Hanson, *Nat. Photonics* 9, 363 (2015).
- [25] N. Akopian, L. Wang, A. Rastelli, O. G. Schmidt, and V. Zwiller, *Nat. Photonics* 5, 230 (2011).
- [26] J.-P. Jahn, M. Munsch, L. Béguin, A. V. Kuhlmann, M. Renggli, Y. Huo, F. Ding, R. Trotta, M. Reindl, O. G. Schmidt, A. Rastelli, P. Treutlein, and R. J. Warburton, *Phys. Rev. B* 92, 245439 (2015).
- [27] E. Chekhovich, K. Kavokin, J. Puebla, A. Krysa, M. Hopkinson, A. Andreev, A. Sanchez, R. Beanland, M. Skolnick, and A. Tartakovskii, *Nat. Nanotechnol.* 7, 646 (2012).
- [28] M. Bayer, G. Ortner, O. Stern, A. Kuther, A. A. Gorbunov, A. Forchel, P. Hawrylak, S. Fafard, K. Hinzer, T. L. Reinecke, S. N. Walck, J. P. Reithmaier, F. Klopff, and F. Schafer, *Phys. Rev. B* 65, 195315 (2002).
- [29] J. Puebla, E. A. Chekhovich, M. Hopkinson, P. Senellart, A. Lemaître, M. S. Skolnick, and A. I. Tartakovskii, *Phys. Rev. B* 88, 045306 (2013).

- [30] E. A. Chekhovich, M. N. Makhonin, J. Skiba-Szymanska, A. B. Krysa, V. D. Kulakovskii, M. S. Skolnick, and A. I. Tartakovskii, *Phys. Rev. B* 81, 245308 (2010).
- [31] D. Gammon, S. W. Brown, E. S. Snow, T. A. Kennedy, D. S. Katzer, and D. Park, *Science* 277, 85 (1997).
- [32] K. L. Janssens, F. M. Peeters, and V. A. Schweigert, *Phys. Rev. B* 63, 205311 (2001).
- [33] T. Mano, M. Abbarchi, T. Kuroda, B. McSkimming, A. Ohtake, K. Mitsuishi, and K. Sakoda, *Appl. Phys. Express* 3, 065203 (2010).
- [34] E. A. Chekhovich, M. M. Glazov, A. B. Krysa, M. Hopkinson, P. Senellart, A. Lemaitre, M. S. Skolnick, and A. I. Tartakovskii, *Nat. Phys.* 9, 74 (2013).
- [35] P. Maletinsky, A. Badolato, and A. Imamoglu, *Phys. Rev. Lett.* 99, 056804 (2007).
- [36] P. Maletinsky, C. W. Lai, A. Badolato, and A. Imamoglu, *Phys. Rev. B* 75, 035409 (2007).
- [37] A. E. Nikolaenko, E. A. Chekhovich, M. N. Makhonin, I. W. Drouzas, A. B. Van'kov, J. Skiba-Szymanska, M. S. Skolnick, P. Senellart, D. Martrou, A. Lemaître, and A. I. Tartakovskii, *Phys. Rev. B* 79, 081303 (2009).
- [38] D. Gammon, A. L. Efros, T. A. Kennedy, M. Rosen, D. S. Katzer, D. Park, S. W. Brown, V. L. Korenev, and I. A. Merkulov, *Phys. Rev. Lett.* 86, 5176 (2001).
- [39] Peter Michler, *Single Semiconductor Quantum Dots*, Springer, Page 152 (2009).
- [40] S. Amasha, K. MacLean, Iuliana P. Radu, D. M. Zumbühl, M. A. Kastner, M. P. Hanson, and A. C. Gossard, *Phys. Rev. Lett.* 100, 046803 (2008).
- [41] C. W. Lai, P. Maletinsky, A. Badolato, and A. Imamoglu, *Phys. Rev. Lett.* 96, 167403 (2006).
- [42] C. Latta, A. Högele, Y. Zhao, A. N. Vamivakas, M. Maletinsky, M. Kroner, J. Dreiser, I. Carusotto, A. Badolato, D. Schuh, W. Wegscheider, M. Atature, and A. Imamoglu, *Nat. Phys.* 5, 758 (2009).
- [43] C. A. Kessler, M. Reischle, R. Robach, E. Koroknay, M. Jetter, H. Schweizer, and P. Michler, *Phys. Status Solidi B* 249, 747 (2012).

- [44] E. A. Chekhovich, A. B. Krysa, M. S. Skolnick, and A. I. Tartakovskii, *Phys. Rev. B* **83**, 125318 (2011).
- [45] Changxue Deng and Xuedong Hu, *Phys. Rev. B* **72**, 165333 (2005).
- [46] C. Le Gall, A. Brunetti, H. Boukari, and L. Besombes, *Phys. Rev. B* **85**, 195312 (2012).
- [47] W. A. Coish and J. Baugh, *Phys. Status Solidi B* **246**, 2203 (2009).
- [48] E. Reyes-Gómez, N. Porrás-Montenegro, C. A. Perdomo-Leiva, H. S. Brandi, and L. E. Oliveira, *J. Appl. Phys.* **104**, 023704 (2008).
- [49] A. Ulhaq, Q. Duan, E. Zallo, F. Ding, O. G Schmidt, A. I. Tartakovskii, M. S. Skolnick, and E. A. Chekhovich, *Phys. Rev. B* **93**, 165306 (2016).
- [50] R. K. Sundfors, *Phys. Rev. B* **10**, 4244 (1974).
- [51] G. S. Pearson and D. A. Faux, *J. Appl. Phys.* **88**, 730 (2000).
- [52] E. A. Chekhovich, M. N. Makhonin, J. Skiba-Szymanska, A. B. Krysa, V. D. Kulakovskii, M. S. Skolnick, and A. I. Tartakovskii, *Phys. Rev. B* **81**, 245308 (2010).
- [53] Christian Latta, Ajit Srivastava, and Atac Imamoğlu, *Phys. Rev. Lett.* **107**, 167401 (2011).

Chapter 5

Tuning the Coupling Strength and Mode Symmetry of Photonic-Molecules Using End-Hole Displacement

5.1 Introduction

Coupled photonic crystal (PhC) microcavities, also known as “photonic molecules” due to their molecular-bond-like optical mode bonding and anti-bonding, have attracted much attention lately for their unique properties such as optical analogue of superradiance [1,2], electromagnetically induced transparency [3-5] and their potential application in quantum computational devices containing quantum emitters [6-8]. In photonic nanostructures, photonic cavities are key components because photons can be trapped and stored in cavities and interactions with various gain and nonlinear media such as QDs can be induced. For this attractive potential, tuning of the coupling strength and symmetry of the optical modes is essential. Various factors affecting the coupling strength between two resonators have been studied, such as the cavity-cavity distance [9], the pumping location [10], and the cavity geometries [11]. Due to the high optical

quality factor and small modal volume, L3 cavities have been explored extensively ever since Yoshihiro Akahane et al reported their silicon-based two-dimensional photonic-crystal nanocavity with ultra-high Q factor [12]. Varying the numbers of air holes that separate two L3 cavities can digitally shift the mode splitting, however, a continuous tuning of the coupling is preferable. Although elaborate barrier engineering has been carried out to continuously tailor the coupling strength and sign of coupled L3 cavities in the ΓM and ΓK direction [11], a simple but efficient tuning technique is yet to be demonstrated for the coupled systems along the line of missing holes.

In this chapter, investigations on energy splitting, quality factor and electric field distribution of the fundamental modes of coupled L3 photonic crystal cavities have been carried out using Lumerical FDTD (introduced in Section 2.1) and GME (discussed in Section 2.2) methods. A continuous variation of the energy splitting with the end-hole shift of the cavity is calculated, together with a large tuning range and symmetry-reversible bonding and anti-bonding states. The calculations agree well with optical spectroscopic measurements using cavity-coupled QD emitters. Combining the fine control of localized mode symmetry demonstrated here with optical nonlinearities opens up the possibility of new studies of fundamental phenomena such as spontaneous symmetry breaking [13, 14], Josephson oscillations [15, 16] and optical self-trapping [16, 17].

5.2 Single Photonic Crystal L3 Cavity

As one of the most important PhC microcavity types, the L3 defect photonic crystal resonator consists of a PhC membrane with a line of three missing holes in the centre. A typical photonic crystal L3 cavity, noting the end-hole with red circles, is shown in Figure 5.1(a), where the insert indicates the end-hole shifts from the original position by a distance S . The central wavelength of the cavity mode is located at 899.115 nm with a calculated Q factor of 97,000. $|E|^2$ profile (c), E_x (d) and E_y (e) represent the electric field distributions of the simulated cavity mode corresponding to the yellow rectangle region in (a).

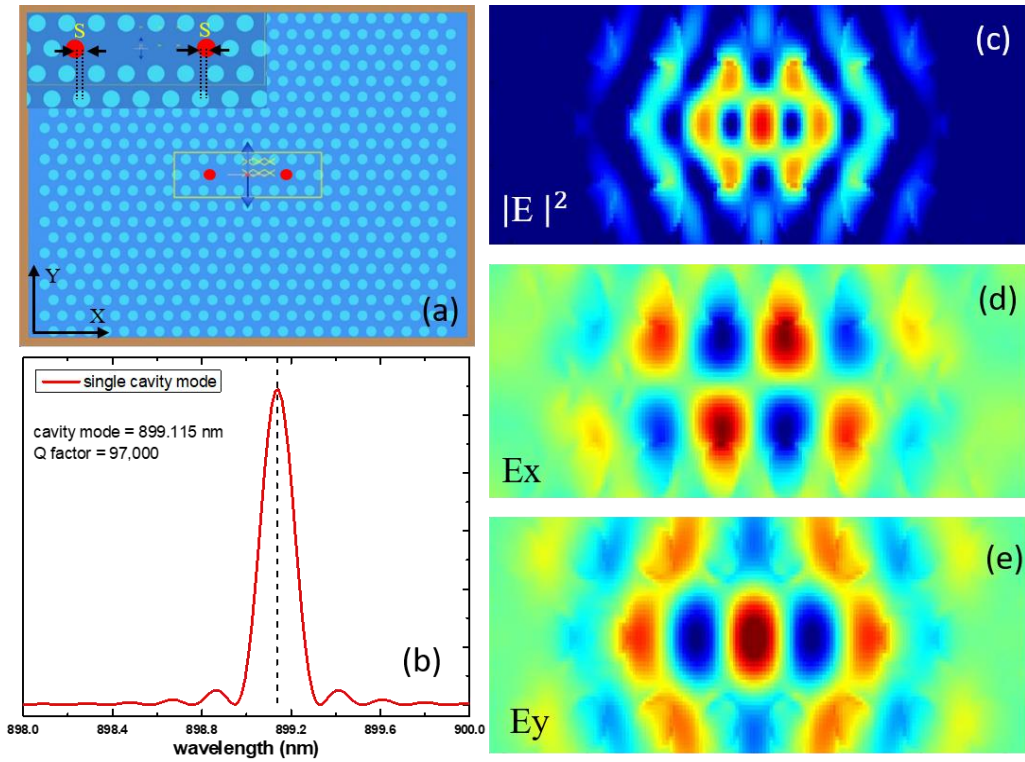


Figure 5.1: A typical photonic crystal L3 cavity (a), noting the end-hole with red circles. The insert in (a) indicates the end-hole shifts from the original position by a distance S . The central wavelength of the cavity mode is located at 899.115 nm with a Q factor of 97,000 (b). $|E|^2$ profile (c), E_x (d) and E_y (e) represent the electric field distributions of the simulated cavity mode corresponding to the yellow rectangle region in (a).

5.3 Simulation Results of Photonic-Molecules

The photonic molecule, shown in Figure 5.2(a), is a two dimensional hexagonal lattice of air holes (refractive index $n=1$) with lattice constant $a=240$ nm, depth $d=140$ nm, fill factor $r=0.29*a$ with variable end-hole displacement. It has been demonstrated that, by shifting the position of the two end holes of a single L3 cavity, the envelope function of field distribution for the fundamental mode can be tailored, and a much higher quality factor of the cavity mode can be achieved [10]. In the case of two coupled L3 cavities, wavefunction modification induced by the end-hole shift results in a variation of cavity coupling, and can be used to tune the L3 cavity coupling.

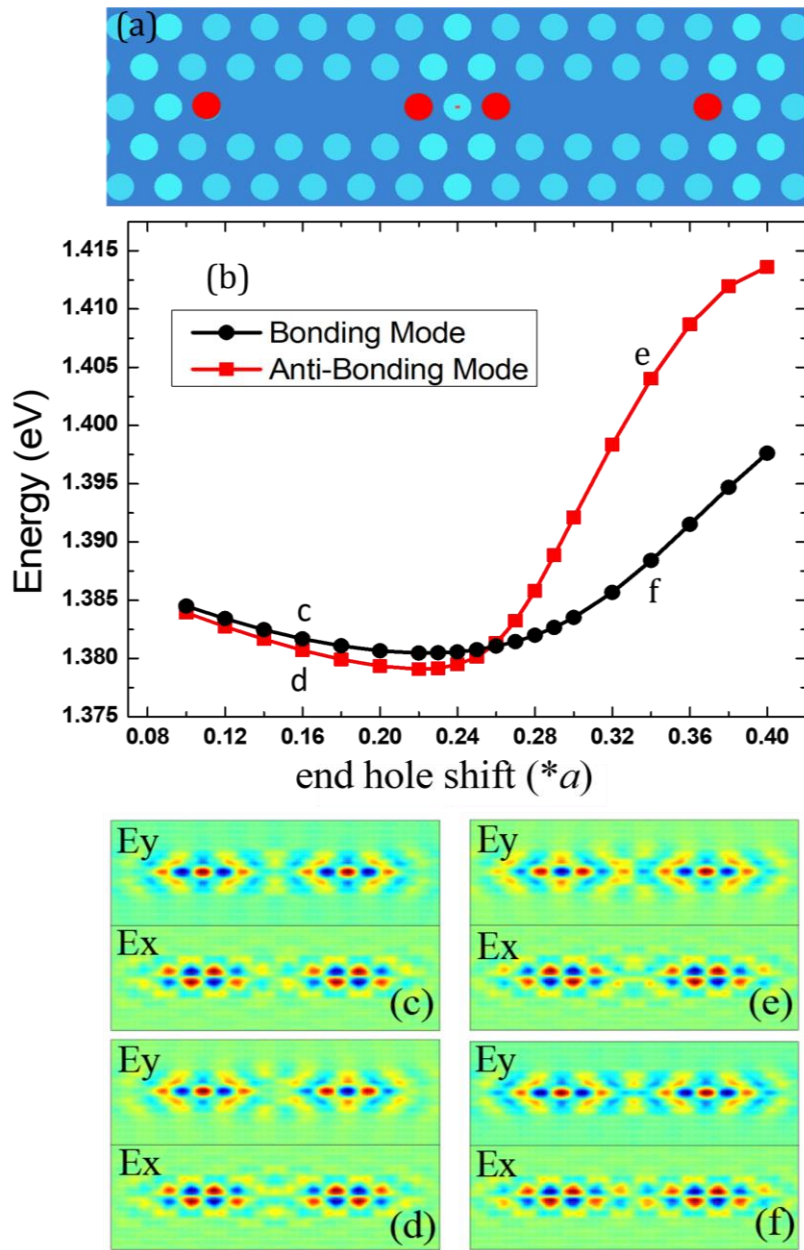


Figure 5.2. (a) Schematic of the photonic molecule. Red holes represent the end holes of the two coupled L3 cavities. (b) The split states of the coupled L3 cavities separated by 3 air holes. The black-dot curve is the bonding mode (even parity) and the red-square curve shows the antibonding mode (odd parity). (c) Simulated E_x and E_y field distributions of the higher energy mode and (d) lower energy mode with the end hole shift of $0.16*a$; (e) Simulated E_x and E_y field distributions of the higher energy mode and (f) lower energy mode with the end hole shift of $0.34*a$.

Figure 5.2(b) shows the calculated energies of the split fundamental modes of parallel L3 cavities separated by 3 air holes and coupled along the line of missing holes for different end-hole shifts. The simulated E_x and E_y field distributions of the coupled modes are shown in Figure 5.2(c), (d), (e) and (f), corresponding to the split energy states in Figure 5.2(b) labelled as c, d for the higher and lower energy states with end hole shift of $0.16*a$, and e, f for the higher and lower energy states with end hole shift of $0.34*a$. Following the terminology of quantum mechanics, the parity of the coupling states can be clearly identified from those field distributions, where the photonic molecular state with even (symmetric) parity is defined as the bonding (B) state and it corresponds to the ground state in the case of positive coupling; the photonic molecular state with odd (asymmetric) parity is defined as the antibonding (AB) state and is associated to the excited state if the coupling is positive coupling [18]. In other words, the state with its E_y component at the centre of the coupled cavities having the same sign is attributed to the bonding states, and the states with opposite sign of E_y component at the cavity centre is attributed to anti-bonding modes. By this definition, c and f states (all the states shown by the red-dot curve in Figure 5.2(b)) are B modes with even parity, whilst d and e states (all the states shown by the black-dot curve in Figure 5.2 (b)) are AB modes with odd parity, as shown in Figure 5.2(c)-(f).

It is obvious from Figure 5.2 (b) that the energies of the split fundamental modes depend strongly on the position of the end holes (red holes in Figure 5.2 (a)). For an end hole shift smaller than $0.23a$, the energies of both B mode and AB mode decrease slowly as the displacement of the end-holes increase; with further increasing the end hole shift from $0.23*a$, these two modes approach degeneracy at 1.382 eV with end hole shift of $0.256*a$. When the end-hole shift is larger than $0.256*a$, the mode splits again and mode ordering is reversed, i.e. the B mode is the ground state and the AB mode becomes the excited state, due to oscillations in the coupling matrix element. With end-hole shift larger than $0.256*a$, the energy of AB mode increases sharply, while the energy of B mode grows steadily.

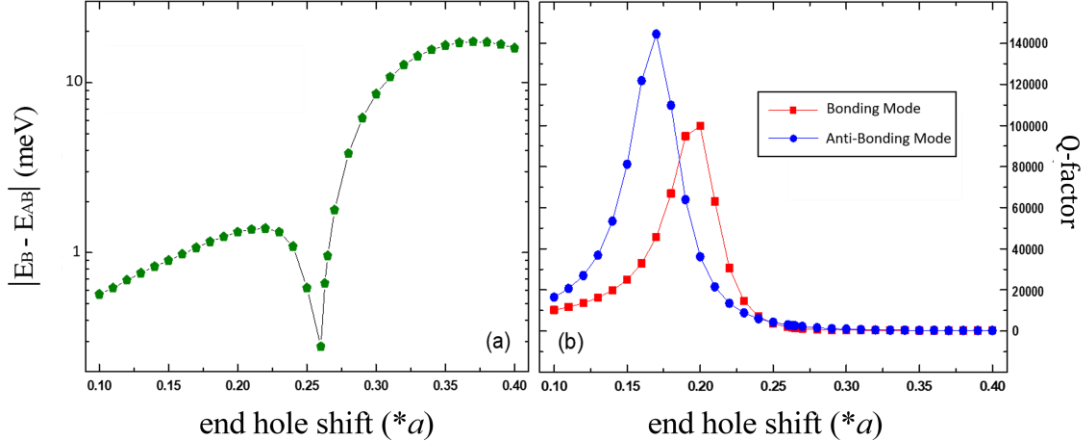


Figure 5.3: End-hole shift dependence of B-AB mode energy splitting (a) and Q factors for B mode and AB mode (b).

The energy splitting ΔE , corresponding to the absolute value of the subtraction between B mode and AB mode, can be increased by more than one order of magnitude when tune end-hole shift as displayed in Figure 5.3(a). The minimum splitting appears at $0.256*a$. Figure 5.3(b) shows the end hole shift dependence of the quality factors for the B mode and the AB mode. The Q factor reaches the maxima (over 100000) at $0.20*a$ and $0.17*a$ for B and AB mode, respectively.

5.4 Theoretical Model Comparison with FDTD Simulation

In order to understand better the susceptibility of the bonding-antibonding splitting (BAB) to the end-hole displacement, it is instructive to start with a simple perturbation theory calculation of the coupling between two L3 cavities following the model of coupling in quantum systems.

The eigenvalue equation for the magnetic field \mathbf{H} is calculated:

$$\nabla \times (\eta \nabla \times \mathbf{H}) = \omega^2 \mathbf{H} \quad (5.1)$$

where $\eta(\mathbf{r})$ is the inverse of the permittivity $\varepsilon(\mathbf{r})$ and ω is the frequency.

To solve the perturbation theory calculation, a basis of the eigen-modes of two isolated L3 cavities is chosen carefully. The two isolated cavities are located at the positions within the lattice of the actual cavities, called \mathbf{H}_1 and \mathbf{H}_2 . Similarly, the η function is divided into two parts: $\eta(\mathbf{r}) = \eta_1(\mathbf{r}) + \tilde{\eta}_{12}(\mathbf{r})$, where $\eta_1(\mathbf{r})$ presents the single isolated cavity (cavity 1) in the photonic crystal and the perturbation part $\tilde{\eta}_{12}(\mathbf{r})$ is the correction to this because of the presence of another cavity (cavity 2).

$$\begin{aligned}\nabla \times [(\eta_1 + \tilde{\eta}_{12})\nabla \times \mathbf{H}_1] &= \omega_1^2 \mathbf{H}_1 + \nabla \times (\tilde{\eta}_{12} \nabla \times \mathbf{H}_1) \\ \int d^3\mathbf{r} \mathbf{H}_1(\mathbf{r}) \cdot \nabla \times (\eta(\mathbf{r})\nabla \times \mathbf{H}_1(\mathbf{r})) &= \omega_1^2 + \int d^3\mathbf{r} \mathbf{H}_1(\mathbf{r}) \cdot \nabla \times (\tilde{\eta}_{12}(\mathbf{r})\nabla \times \mathbf{H}_1(\mathbf{r})) \\ &= \omega_1^2 + V_{11}\end{aligned}\quad (5.2)$$

where

$$\begin{aligned}V_{11} &= \int d^3\mathbf{r} \mathbf{H}_1(\mathbf{r}) \cdot \nabla \times (\tilde{\eta}_{12}(\mathbf{r})\nabla \times \mathbf{H}_1(\mathbf{r})) \\ &= -\omega_1^2 \int d^3\mathbf{r} \mathbf{D}_1(\mathbf{r}) \cdot \mathbf{D}_2(\mathbf{r}) \tilde{\eta}_{12}(\mathbf{r})\end{aligned}\quad (5.3)$$

Similarly

$$\int d^3\mathbf{r} \mathbf{H}_2(\mathbf{r}) \cdot \nabla \times (\eta(\mathbf{r})\nabla \times \mathbf{H}_1(\mathbf{r})) = \omega_1^2 S_{12} + V_{12}, \quad (5.4)$$

where

$$V_{12} = -\omega_1 \omega_2 \int d^3\mathbf{r} \mathbf{D}_2(\mathbf{r}) \cdot \mathbf{D}_1(\mathbf{r}) \tilde{\eta}_{12}(\mathbf{r}). \quad (5.5)$$

So equation $E_1 = \omega_1^2$ needs to be solved

$$\begin{pmatrix} E_1 + V_{11} & E_1 S_{12} + V_{12} \\ E_2 S_{12} + V_{21} & E_2 + V_{22} \end{pmatrix} \begin{pmatrix} \alpha \\ \beta \end{pmatrix} = \begin{pmatrix} 1 & S_{12} \\ S_{12} & 1 \end{pmatrix} \begin{pmatrix} \alpha \\ \beta \end{pmatrix}. \quad (5.6)$$

The BAB splitting is then given by

$$\Delta_{\text{BAB}} = \frac{2V_{12}}{1-S_{12}^2} - \frac{2S_{12}}{1-S_{12}^2} V_{11} \quad (5.7)$$

The contribution arising from the non-orthogonality of the basis states \mathbf{H}_1 and \mathbf{H}_2 can be negligible for the parameters considered here ($V_{11} \ll V_{12}$ and $S_{12} \ll 1$), the second term in Eq. (5.7) is very small. Therefore, the BAB splitting Δ_{BAB} can be simplified as

$$\Delta_{\text{BAB}} = 2V_{12} = -2\omega_0^2 \int d^3\mathbf{r} \mathbf{D}_1(\mathbf{r}) \cdot \mathbf{D}_2(\mathbf{r}) \tilde{\eta}_{12}(\mathbf{r}) \quad (5.8)$$

Assuming the two cavities are identical, ω_0 is the isolated mode frequency. The second identity follows from applying the divergence theorem and using Maxwell's equations to convert the magnetic fields \mathbf{H}_1 and \mathbf{H}_2 to the corresponding electric displacement fields \mathbf{D}_1 and \mathbf{D}_2 . Based on the theoretical derivation, the BAB splitting has been calculated using Eq. (5.8), for various values of the end-hole displacement, in the same structure as shown in Figure 5.2(a), with three holes between two cavities. The result can be found in Figure 5.4, which indicates the theoretical calculation (red circles) and FDTD simulation (blue squares) are in good agreement.

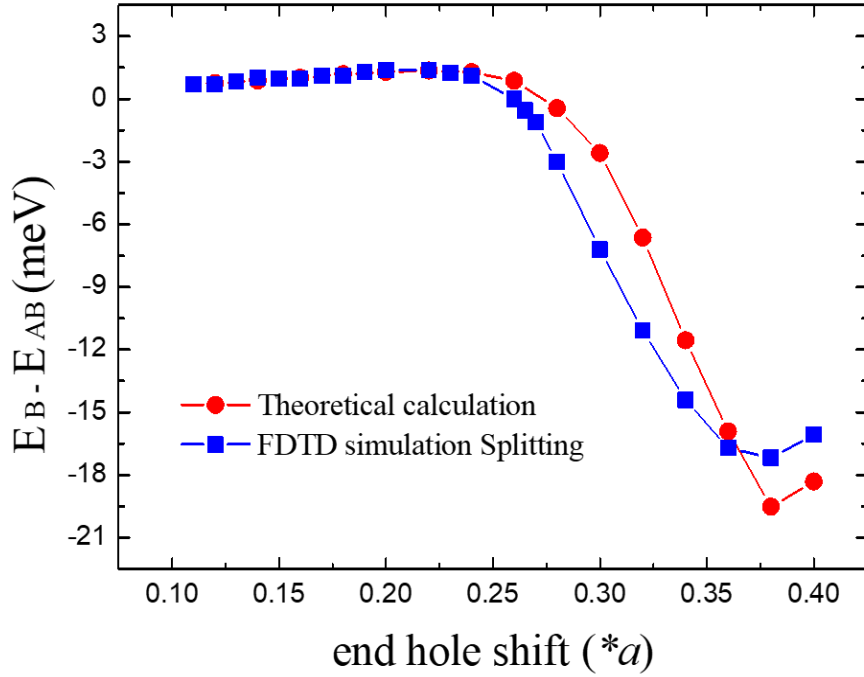


Figure 5.4: Mode splitting, Δ_{BAB} , for a double cavity structure with three holes separation, as determined by simulations of the full structure (blue points and lines) and evaluation of the matrix element V_{12} in Eq.(5.2) (red). The lines are a guide to the eye.

The sensitivity of the BAB splitting to small changes in the structure can be explained by the form of matrix element in Eq. (5.6). $\tilde{\eta}_{12}$ is the perturbation of the lattice

corresponding to the addition of the other cavity (cavity 2), so it is only non-zero at the locations of the three holes which are removed to make this cavity and on either side of the shifted end holes. That is, inside the circles and crescents shown in Figure 5.5, where the black dotted rectangle in (a) indicates the region being simulated in (b).

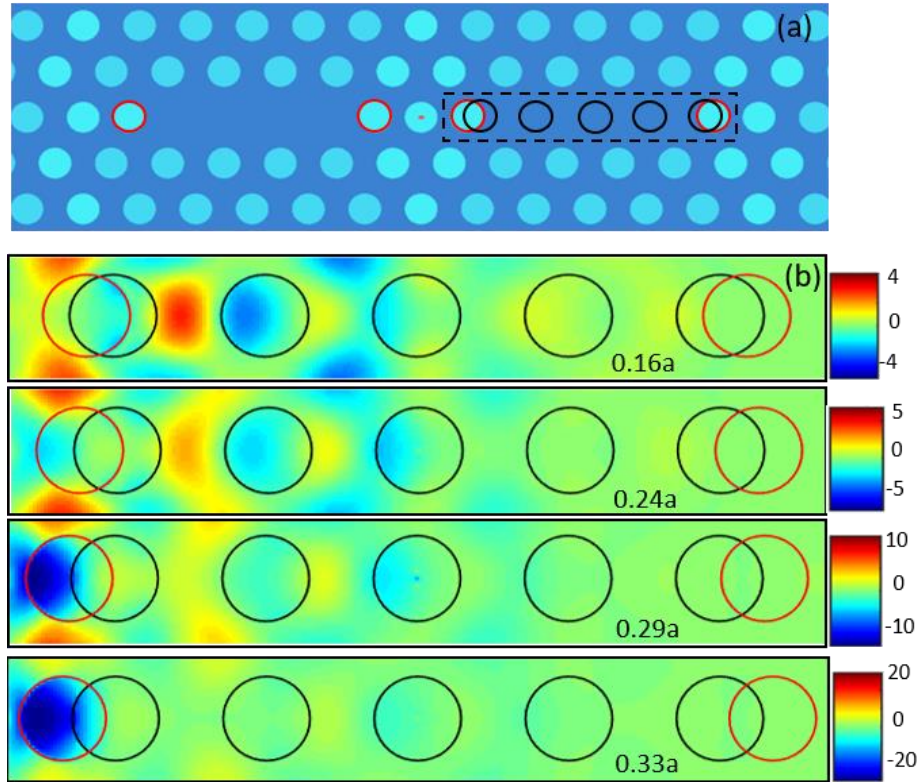


Figure 5.5: (a) Schematic of the photonic molecule as in Figure 5.2(a). The dotted black rectangle indicates the region being calculated. (b) shows the real part of $\mathbf{D}_1 \cdot \mathbf{D}_2$, as a colour scale, in the region of the second cavity for a plane bisecting the slab. The other cavity would be off the figure to the left. $\tilde{\eta}_{12}$ is non-zero only inside the three central circles, which correspond to the holes removed to produce the cavity, and the pairs of crescents at either end, where the holes are shifted. The significant changes to $\mathbf{D}_1 \cdot \mathbf{D}_2$ in these zones, when the end-hole shift is carried, explains the large effect on the BAB splitting.

The three central black circles correspond to the holes removed to produce the cavity, and the pairs of black circles at either end of the black rectangle point out the original position of the end holes while red circles present the shifted holes. Figure 5.5(b) shows

the real part of $\mathbf{D}_1 \cdot \mathbf{D}_2$; and the colour scale on the right side of the figure gives the value of $\mathbf{D}_1 \cdot \mathbf{D}_2$, in the plane of the centre of the slab, for the region around these holes. It can be seen that the relevant part of this, inside the circles and crescents, varies significantly with the end-hole shift, suggesting that the splitting is determined only by the values of the fields in these small regions, even though the overall effect on the single cavity is just a slight change in the strength of the confinement along the axis of the cavity.

5.5 Dependence on Cavity Separations

In order to verify the effectiveness of this tuning method, simulations for coupling L3 cavities with different cavity centre separation (cavities separated by different numbers of holes) have been carried out. The end-hole shift dependence of the B-AB mode splitting for different cavity separations can be found in Figure 5.6, where the tendencies of the mode splitting for different cavity separations are similar. Symmetry exchange and level crossing occur at certain end-hole shifts. Particularly, for the case of cavities separated by 4 holes, the B-AB modes cross and parity exchange twice (at $0.20a$ and $0.37a$). Such a multiple level crossing and parity exchange may occur to coupling systems with different cavity separations if the end hole shift is large enough (limited by the photonic lattice constant a).

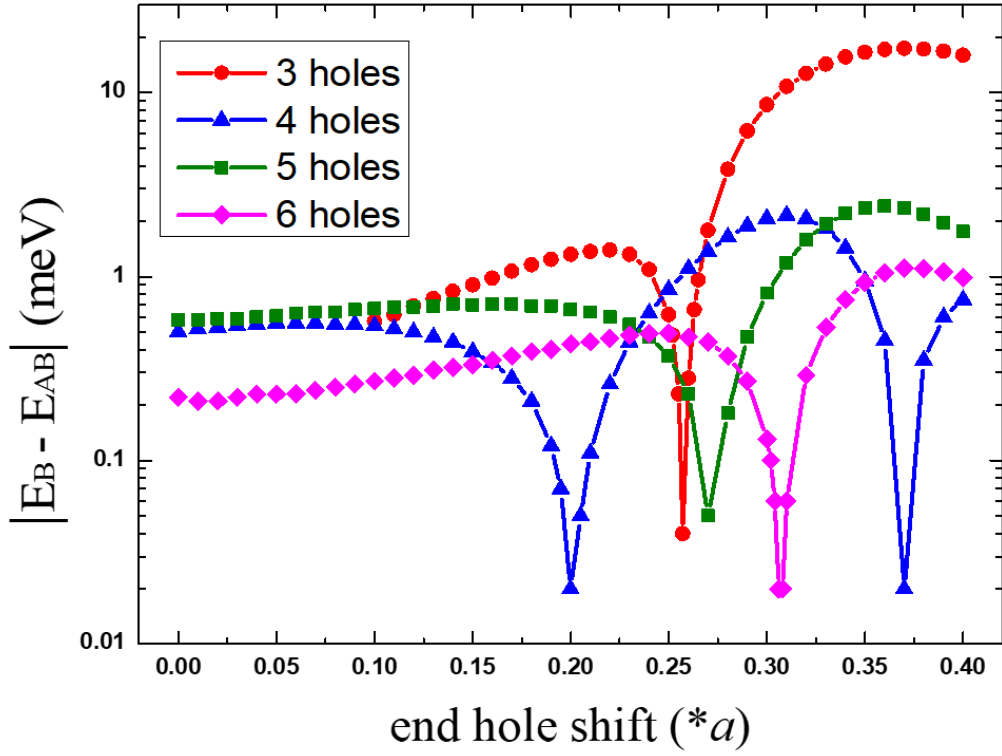


Figure 5.6: End-hole shift dependence of the modes splitting for different cavity separations.

Similarly, the B-AB mode splitting, using Eq. (5.8), for various values of the end-hole shift in structures with different cavity separations, have been calculated. The comparisons between the FDTD simulation results and theoretical model calculations have been made for 4, 5 and 6 holes separation configuration in Figure 5.7. The results are all in good agreement.

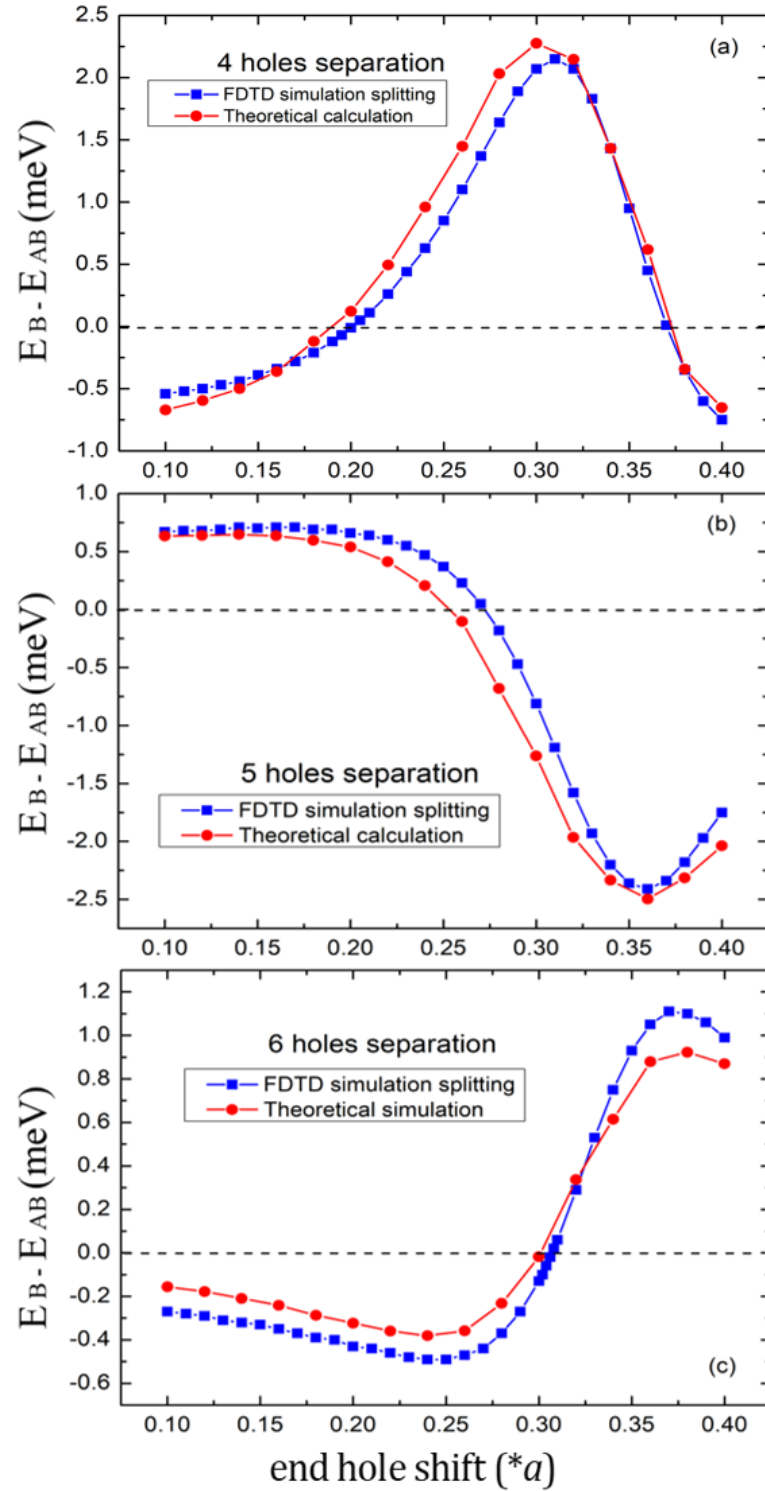


Figure 5.7: Mode splitting, Δ_{BAB} , for a double cavity structure with different hole separations, determined by simulations of the full structure (blue points and lines) and evaluation of the matrix element V_{12} in Eq. (5.5) (red). The lines are a guide to the eye.

5.6 Experimental Results

5.6.1 Sample Details

The simulation and theoretical model studied in Section 5.3 indicate that the 3 holes separation configuration offers the largest control of the coupling. Photonic molecules with 3 holes between two L3 cavities were fabricated by Dr. Davis Vaitiekus using electron beam lithography on a 140 nm GaAs membrane containing a single layer of InAs quantum dots (the same procedures presented in Section 3.1). The density of the dots is low enough for further investigation on single quantum dot coupling to cavities. A $\sim 1 \mu\text{m}$ AlGaAs sacrifice layer was between the GaAs membrane and Si substrate. HF acid was used to remove the AlGaAs sacrificial layer. The duration of underetch was vital as the HF acid needs to remove the material in the position of air holes forming periodic arrays. An overview SEM image of a photonic molecule device is shown in Figure 5.8. In order to confine the light strongly, air holes should be fabricated over at least $2 \mu\text{m}$ distance away from the cavity in X and Y directions.

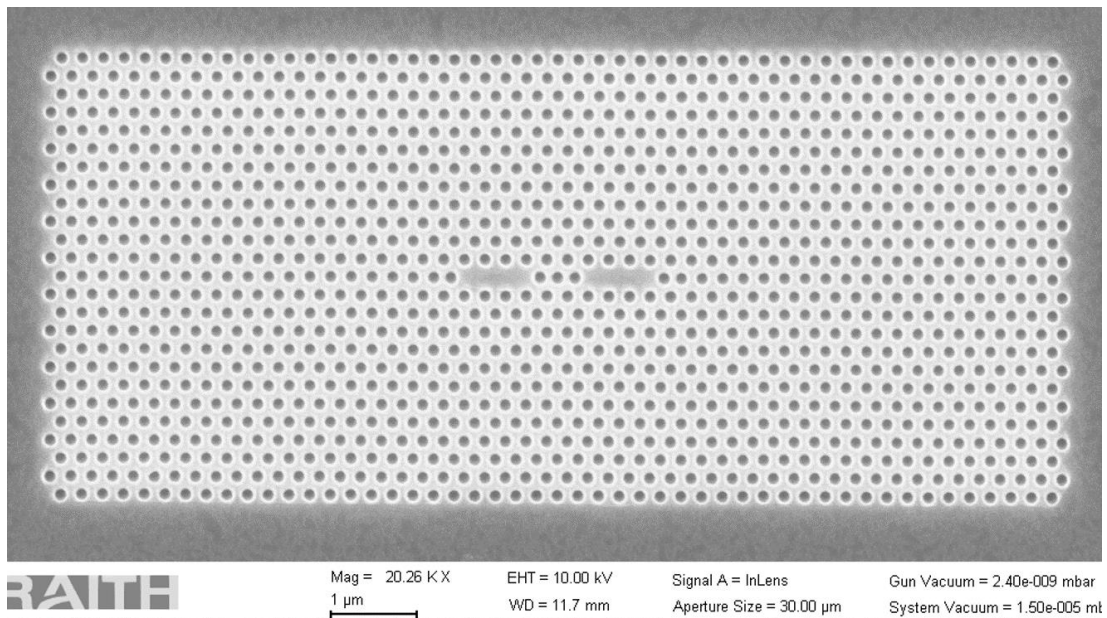


Figure 5.8: An overview SEM image of a photonic molecule device.

Photonic molecules were prepared with different end-hole shifts (from $0.10*a$ to $0.40*a$), and the same a (lattice constant), d (lattice thickness), and r (hole radius) parameters used in the simulation. Two typical scanning electron microscope images of the devices, with different end-hole displacement S_1 and S_2 , showing the precise control of fabrication, are presented in Figure 5.9(a) and (b), respectively.

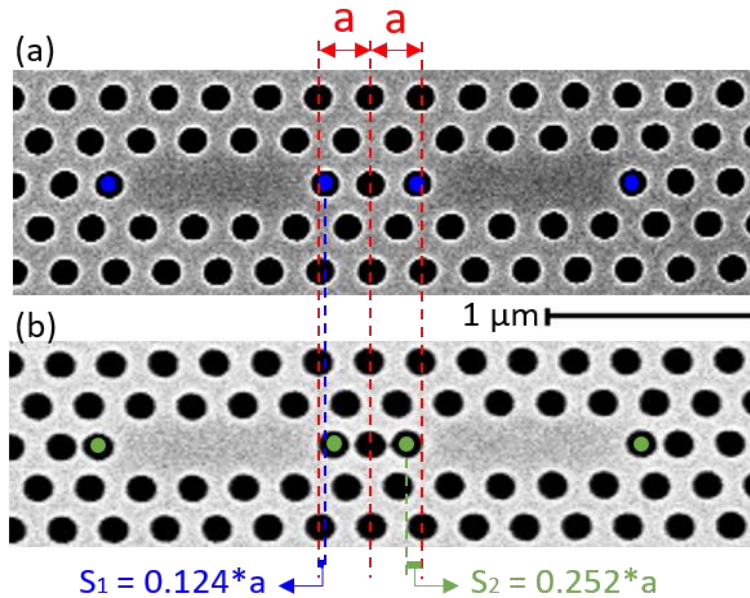


Figure 5.9: Typical SEM images of the coupling L3 cavities with different end-hole shifts S_1 and S_2 , showing the precise control of fabrication.

5.6.2 PL Characterisation of Photonic-Molecules

Photoluminescence spectroscopic (PL) measurements were carried out by exciting the dots, which act as an internal light source within the photonic molecule. The HeNe laser operating at 633 nm was focused to a $\sim 1 \mu\text{m}$ spot using a microscope objective lens with numerical aperture $NA = 0.5$. The samples were mounted in a helium flow cryostat (discussed in Section 3.2), at a temperature of 4 K. Excitation and collection take place on the same position of the device, roughly at the centre of the photonic molecules.

The splitting of the fundamental mode observed in the PL measurements is shown in the waterfall plot (Figure 5.10(a)), corresponding to the end-hole shift from $0.09*a$ to $0.39*a$. The energies of the PL peaks are extracted and plotted in Figure 5.10 (b), where the blue dots show the higher energy mode component of the splitting and the green squares are the lower energy mode. The black and red curves are the theoretical results with $a=245$ nm and $r=0.265*a$ using the simulation method described in Section 5.3. Good agreement can be found between the experimental results and guided mode expansion (GME) calculations.

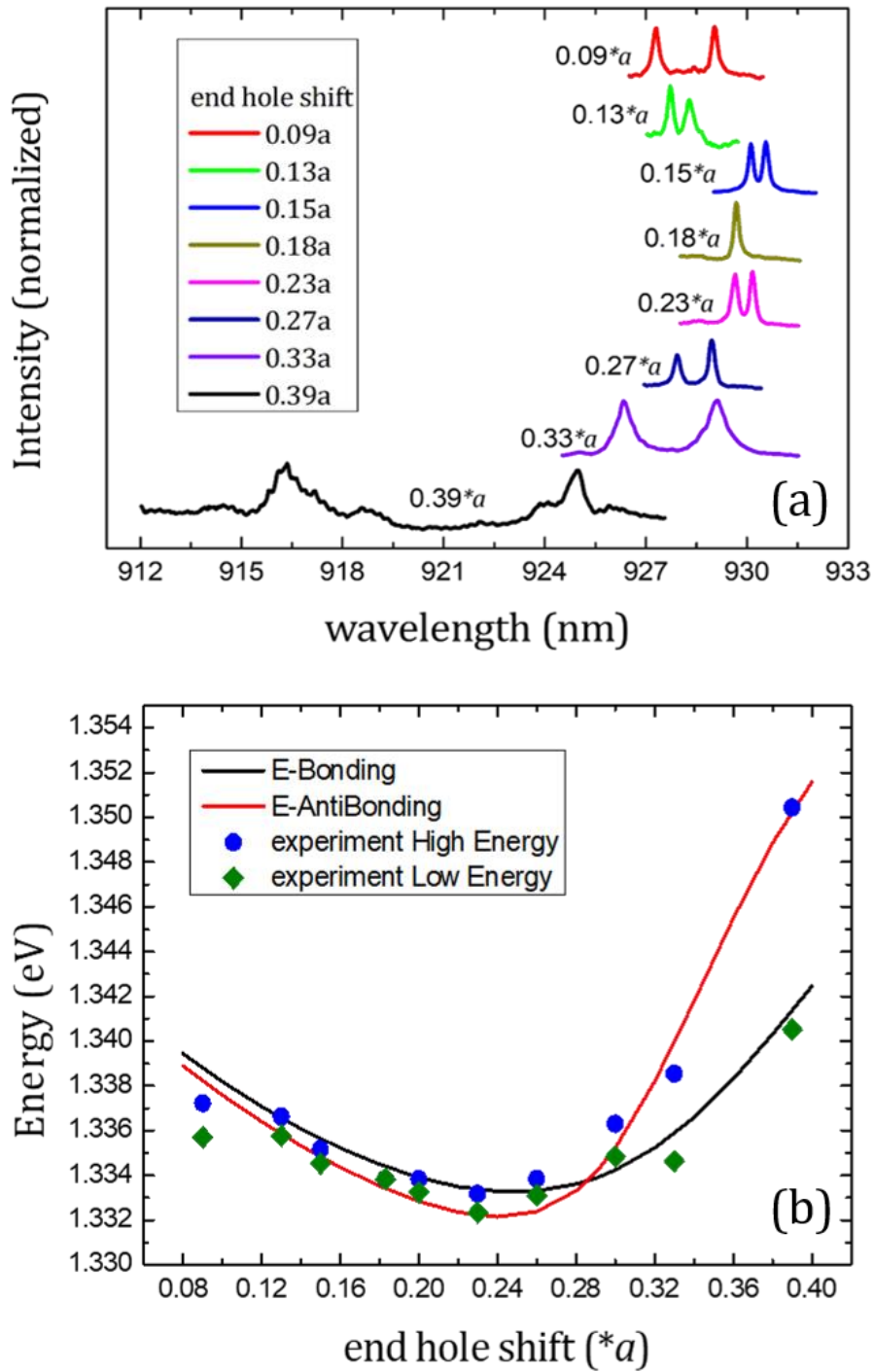


Figure 5.10: (a) Waterfall plot of PL spectra of the photonic molecules with different end-hole shift from $0.09*a$ to $0.39*a$. (b) Energies extracted from the peaks in (a) (green and blue dots) and guided mode expansion (GME) calculated results (red and black lines). Parameters for sample fabrication: $a=245$ nm and $r=0.265*a$.

For further comparison, devices with varying lattice constant a and hole radius r were fabricated and characterized. The end-hole shift dependences of the B-AB splitting for 3 groups of devices are presented in Figure 5.11. Experimental results of samples with $a=243$ nm, $r=0.253*a$ (a), $a=241$ nm, $r=0.26*a$ (b), and $a=240$ nm, $r=0.256*a$ (c) showing significant mode splitting tuning and parity exchange at certain end-hole shift values, as predicted by the GME simulation shown in Figure 5.11(d).

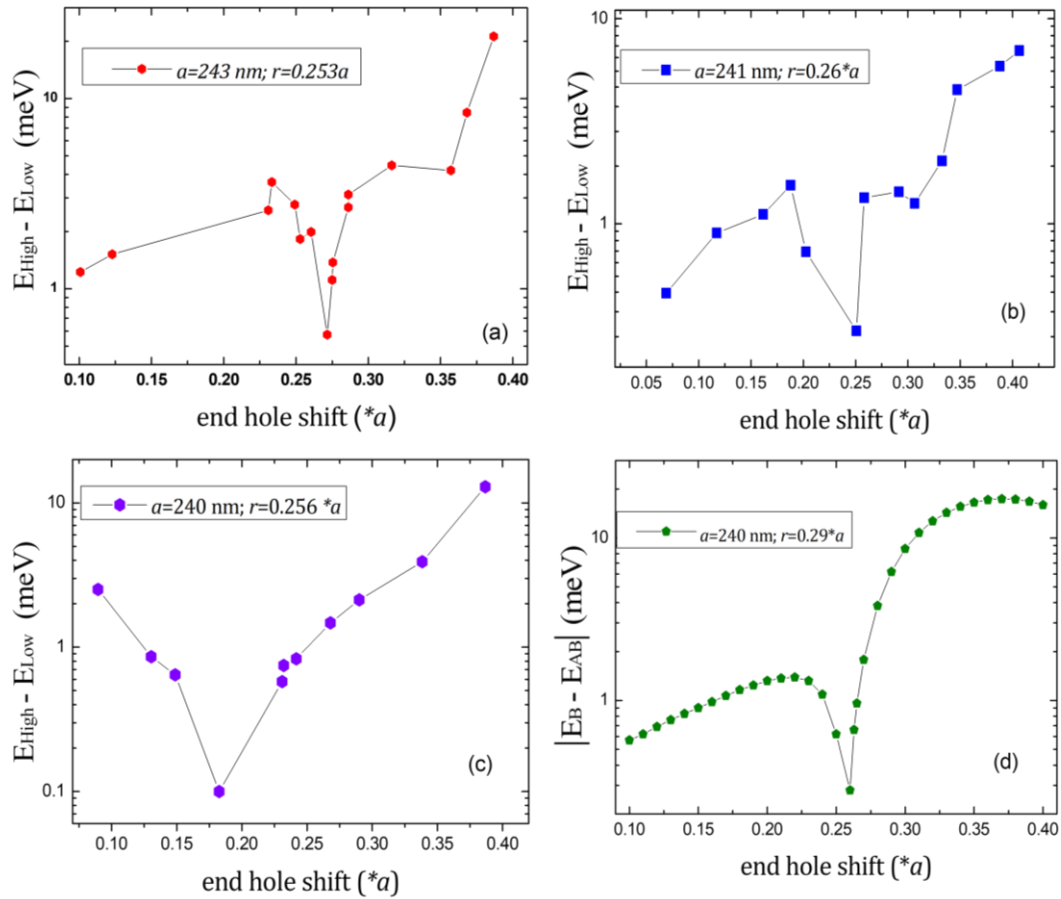


Figure 5.11: (a)-(c) Experimental results of end-hole shift dependences of the S-AS splitting for 3 groups of devices and (d) GME simulation results for comparison.

5.7 Waveguide Induced Strong Coupling between Distant L3 Cavities

When individual cavities are coupled, they must be placed close to each other within the range of a few wavelengths [19, 20] due to the evanescent fields of each cavity extend just a few wavelengths. The photonic molecule device studied above contains two L3 cavities coupled directly through several separated air holes. However, with this spatial limitation, photonic cavities can only couple to the geometrically adjacent cavities. The architecture of the system and the on-demand control of the coupling states are severely restricted. Strong coupling between distant photonic nanocavities and its dynamic control have been realized theoretical and experimentally in Si material [21] based on the established fabrication techniques and high Q factors in Si photonic nanocavities. However, in III-V semiconductors, due to the fabrication limitation and relatively low Q factors, it is yet to be demonstrated. Here, in the following work, preliminary simulation results on strong coupling between distant L3 cavities in GaAs make it possible to break the current spatial limitation and also provide the potential to realize the next-generation photonic circuits.

In order to couple these distant cavities, a waveguide serving as a “bridge” between the cavities need to be introduced. Based on the extensive studies and good understandings of L3 cavities, a pair of L3 cavities was chosen to be connected indirectly through a photonic waveguide. The calculated structure is shown in Figure 5.12.

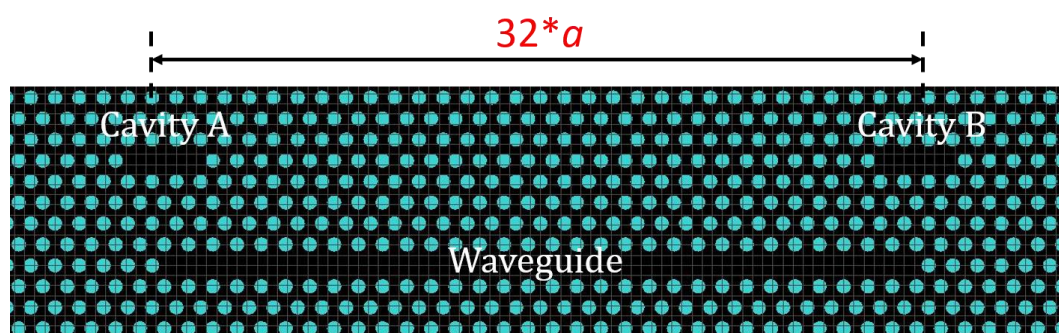


Figure 5.12: Calculated structure based on a photonic crystal waveguide induced L3 cavities device with a lattice constant α of 250 nm.

As indicated in Figure 5.12, the distance between the two L3 cavities (center-to-center) is set as $32*a$ ($8\ \mu\text{m}$). A waveguide (length, $8\ \mu\text{m}$), consisting of a row of missing air holes, is introduced under the cavities and separated by 4 rows of air holes away from the cavities. As the end of waveguide is terminated by air holes, standing waves exist forming FP modes in the waveguide. The free spectral range (FSR) between the FP waveguide modes can be calculated by the length of the waveguide and the group velocity of photons. In the simulation, photons in the L3 cavity can couple to the FP waveguide modes if the cavity mode coincides with any of the FP waveguide modes within the coupling bandwidth. As a consequence, the formation of strong coupling between the distant cavities would be impossible due to the substantial leakage of photons from cavities to the waveguide. Therefore, it is essential to design the coupling bandwidth of cavity modes to be much smaller than the FSR of the FP waveguide modes, and avoid the photons in individual cavities leaking out to the FP waveguide modes. The coupling between distant cavities can still occur indirectly via the forced oscillation of the FP waveguide modes. Strong coupling of the cavity modes can happen due to the cavities having the same resonant wavelength and when the photon leakage is suppressed substantially.

In order to confirm the coupling between distant L3 photonic cavities numerically, varFDTD simulations have been carried out. As discussed in Section 2.3, the varFDTD method provides best trade-off between simulation accuracy and speed: sufficiently accuracy and versatility to that of 3D FDTD, while only needs the modelling time and memory of a 2D planar FDTD simulation. The key to varFDTD method is to use the right effective refractive index. Here, after a series of calculations, $n=2.85$ has been picked. Firstly, photonic modes of the simulated structures, were calculated by exciting the system with a wide-spectrum pulse in the spectral/frequency domain. The results in Figure 5.13 show several FP waveguide modes, labeled as WG1, WG2 and WG3. Red peaks labeled as S and AS represent the symmetric and asymmetric mode, respectively. Only the denoted FP waveguide modes (WG1, WG2, WG3) were observed when calculating without cavities. S and AS peaks correspond to the cavity modes, which split into two peaks, indicating the strong coupling between the distant photonic L3 cavities.

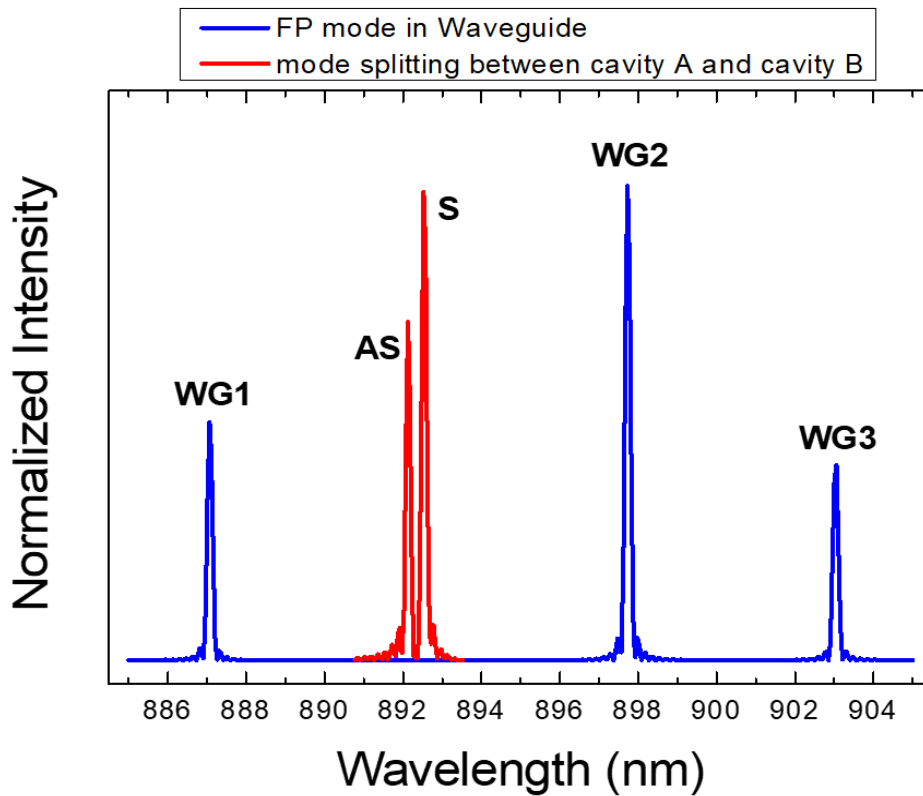


Figure 5.13: Resonant spectra of the simulated structure. Red peaks, resulting from strong coupling between the distant L3 cavities, are labeled as S and AS representing the symmetric and asymmetric mode, respectively. Blue peaks, labeled as WG1, WG2 and WG3, are the FP waveguide modes.

To confirm the splittings are due to the strong coupling, S and AS peaks were monitored in time-domain simulations, where cavity A was excited by a single pulse with the frequency width covered both S and AS modes. Figure 5.14 shows the calculated time evolution of the photon energy in cavity A (black curves) and cavity B (red curves). Rabi oscillation is clearly observed as the cavities exchange photons periodically. Additionally, snapshots of the electric field distribution within the cavities, corresponding to the time evolution investigation, are shown in Figure 5.15. These preliminary results clearly imply that strong coupling between the distant GaAs photonic cavities is possible.

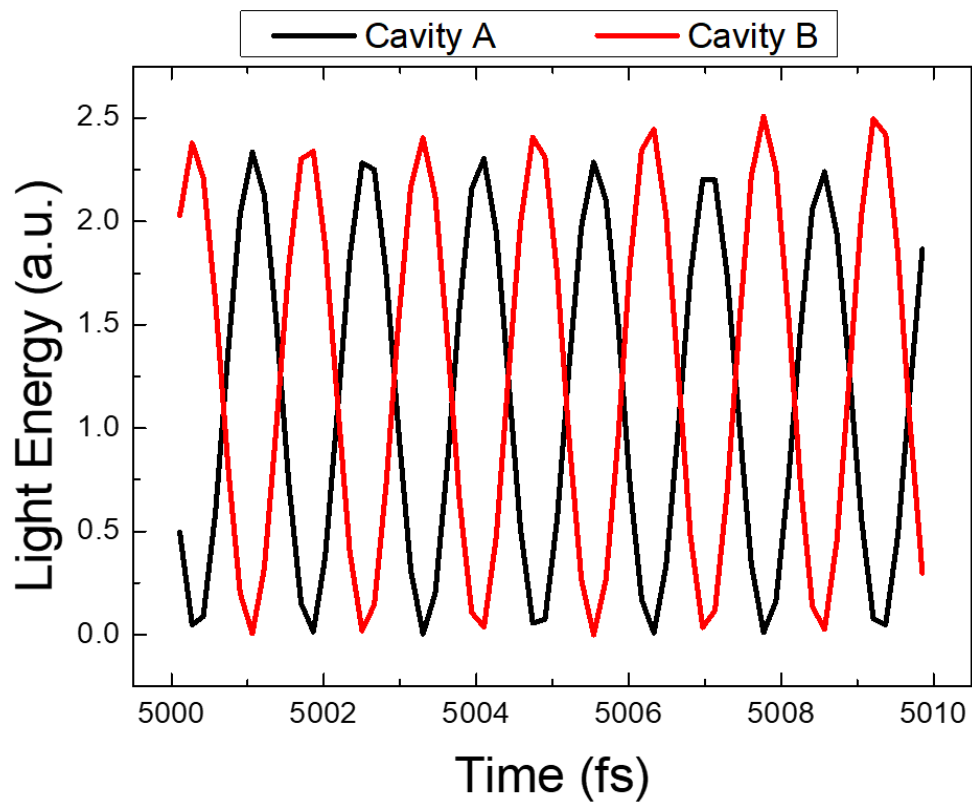


Figure 5.14: Time evolution of the simulated light energy in cavity A (black curve) and cavity B (red curve). Rabi oscillation is clearly observed as the cavities exchange photons periodically.

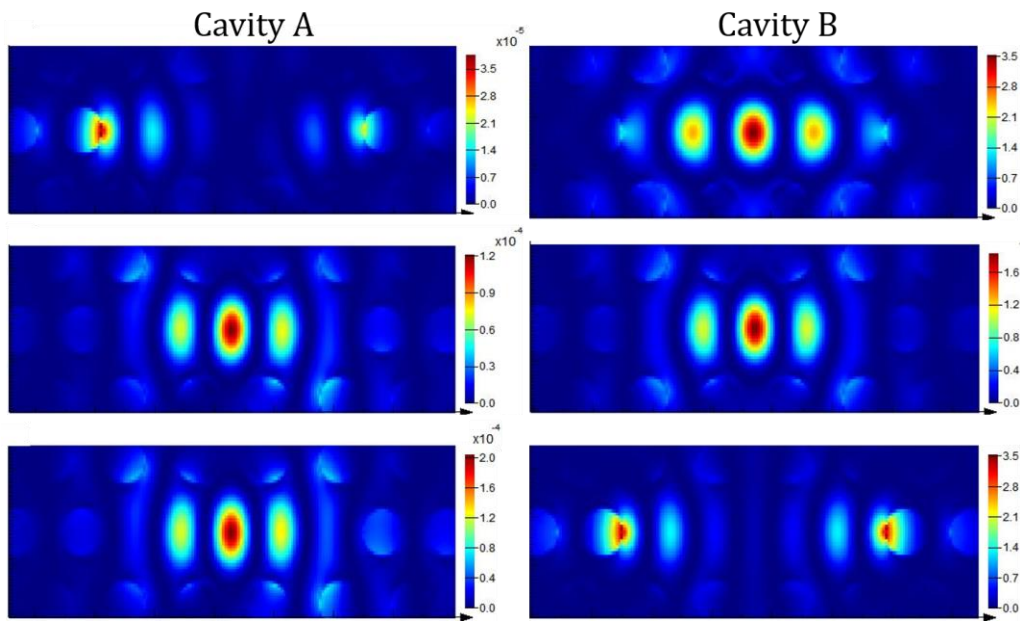


Figure 5.15: Snapshots of the simulated electric field distribution correspond to the time evolution performed in Figure 5.14.

5.8 Summary

In conclusion, key properties such as energy splitting, quality factor and electric field distribution of the fundamental modes of coupled L3 photonic crystal cavities have been studied by performing numerical simulations (FDTD) and developing a theoretical model. A continuous variation of the energy splitting with the end-hole displacement of the cavity, together with a large tuning range and symmetry-reversible bonding and anti-bonding states, have been revealed by numerical simulation and theoretical modeling. Continuous tuning of the coupling strength has been demonstrated experimentally and agrees well with the theoretical calculations. Further work in demonstration of symmetry exchange of localized modes can be carried out by a far-field analysis of the angular emission pattern. Preliminary simulation results for future investigations of waveguide induced strong coupling between distance L3 cavities have also been presented, opening up a potential way to form coupled states on-chip and to realize the next-generation photonic circuits for quantum information processing.

- [1] Robert H. Dicke, Phys. Rev. 93, 99 (1954).
- [2] M. Gross and S. Haroche, Phys. Reports. 93, 301 (1982).
- [3] S. E. Harris, Phys. Today 50, (1997).
- [4] M. O. Scully and M. S. Zubairy, Quantum Optics, Cambridge Univ. Press, Cambridge (1997).
- [5] Xiaodong Yang, Mingbin Yu, Dim-Lee Kwong, and Chee Wei Wong, Phys. Rev. Lett. 102, 173902 (2009).
- [6] E. Peter, P. Senellart, D. Martrou, A. Lemaître, J. Hours, J. M. Gérard, and J. Bloch, Phys. Rev. Lett. 95, 067401 (2005).
- [7] A. Wallraff et al, Nature 431, 162 (2004).
- [8] J. P. Reithmaier et al, Nature 432, 197 (2004).
- [9] Han Du, Xingwang Zhang, Guoqiang Chen, Jie Deng, Fook Siong Chau, and Guangya Zhou, Scientific Reports 6, 24766 (2016).
- [10] Kirill A. Atlasov, Karl Fredrik Karlsson, Alok Rudra, Benjamin Dwir, and Eli Kapon, Optics Express 16, 16255 (2008).
- [11] A. R. Chalcraft, S. Lam, D. O'Brien, T. F. Krauss et al, Appl. Phys. Lett. 90, 241117 (2007).
- [12] Y. Akahane, T. Asano, Bong-Shik Song, and S. Noda, Nature 425, 944-947 (2003).
- [13] Vladimir A. Miransky, Dynamical Symmetry Breaking in Quantum Field Theories.
- [14] ed. by Henryk Arodz, Jacek Dziarmaga, Wojciech Hubert Zurek, Patterns of Symmetry Breaking. P141.
- [15] B. D. Josephson, Phys. Lett. 1, 251 (1962).
- [16] S. Raghavan, A. Smerzi, S. Fantoni, S. R. Shenoy, Phys. Rev. A 59, 620 (1999).
- [17] M. Albiez et al, Phys. Rev. Lett. 95, 010402 (2005).
- [18] N. Caselli, F. Intonti, F. Riboli, A. Vinattieri, D. Gerace, L. Balet, L. H. Li, M. Francardi, A. Gerardino, A. Fiore, and M. Gurioli, Phys. Rev. B 86, 035133 (2012).

[19] F. Xia, L. Sekarixc, and Y. Vlasov, *Nat. Photonics* 1, 65 (2007).

[20] M. Notomi, E. Kuramochi and T. Tanable, *Nat. Photonics* 2, 741 (2008).

[21] Y. Sato, Y. Tanaka, J. Upham, Y. Takahashi, T. Asano and S. Noda, *Nat. Photonics* 6, 56 (2012).

Chapter 6

Waveguide-Coupled Ring Resonators for On-Chip Spectral Filtering Applications

6.1 Introduction

Semiconductor quantum dots (QDs) in whispering gallery mode resonators (WGMs) have been intensively explored as they possess many advantages for quantum photonic applications [1-4]. Previous studies have shown effects such as spontaneous emission enhancement (Purcell effect) [5, 6], QD-based deterministic bright single photon emission [1, 4, 7], lasing [8, 9] and Rabi oscillation [10, 11] etc. Besides these striking features of the QD-WGM coupling system, they can also be very easily integrated with other monolithic circuit elements [1, 12]. This makes them excellent candidates for applications such as optical switching using single photons [13-15] and on-chip spectral filtering [16-19] etc. The integrated semiconductor whispering gallery mode resonator family includes two types of cavities: micro-disk and micro-ring resonators. In fact, a ring resonator can be treated as a special type of WGM resonator transforming from a micro-disk with its inner part being removed. In a micro-disk, the field distribution of the WGMs can cover the whole micro-disk, while in a micro-ring, only the lower order WGMs existence between the outer and inner edges. The free spectral range (FSR),

governed by the first order radial modes, can be largely increased with reduced amplitude of the other modes, leading to a more suitable device towards on-chip filtering techniques using QDs. The energy transfer efficiency of a ring resonator can be higher than that of a micro-disk for spectral filtering applications as the optical loss caused by the absorption of higher order modes can be neglected. Furthermore, different coupling configurations based on ring resonators can be custom designed into integrated optical devices, such as a filter with a flat top [20] or a reflector device [21] for an integrated semiconductor optical amplifier serving as a laser [22].

This chapter investigates the application of WGMs for on-chip spectral filtering applications. The mode structure and transmission spectra of ring resonators coupled to a single mode waveguide are studied by using “2.5D” FDTD simulations, where parameters are optimized to realize the filtering at QD wavelengths. The ultra-narrow notch filtering effect and the Purcell enhancement of single QD emission are achieved using transmittance and photoluminescence spectroscopy measurements.

6.2 Simulation and Design of Ring Resonators

6.2.1 WGMs Formation and Field Distribution in a Ring Resonator

A planar optical WGM resonator is a type of device where optical modes can be almost perfectly trapped by optical total internal reflection (TIR) at the outer lateral interface. As a special resonator (not a true WGM due to additional confinement by inner surface), a ring resonator inherits most optical properties of WGM resonators. The modes in a ring resonator are confined between the outer and inner edges, which work as boundaries and form a potential well. Similar to the case of a microdisk resonator, the internal part of the modal fields of a ring resonator are also the solutions of the 2D Helmholtz equation in cylindrical coordinates for the radial H_z fields [23, 24]. The solutions for the region between inner dielectric radius R_{inner} fields and outer dielectric radius R_{outer} can be obtained as

$$H_z(r, \theta) = J_m(kr)e^{i(\pm m\theta - \omega t)} \quad R_{\text{inner}} \leq r \leq R_{\text{outer}} \quad (6.1)$$

where J_m is the m -th order Bessel function of the first kind, k is the propagation constants and m is the number of optical periods. A schematic illustration of the solutions can be found in Figure 6.1, where (31,3) is the 3rd root (3rd order radial modes) of the 31-th order Bessel function of the first kind [12].

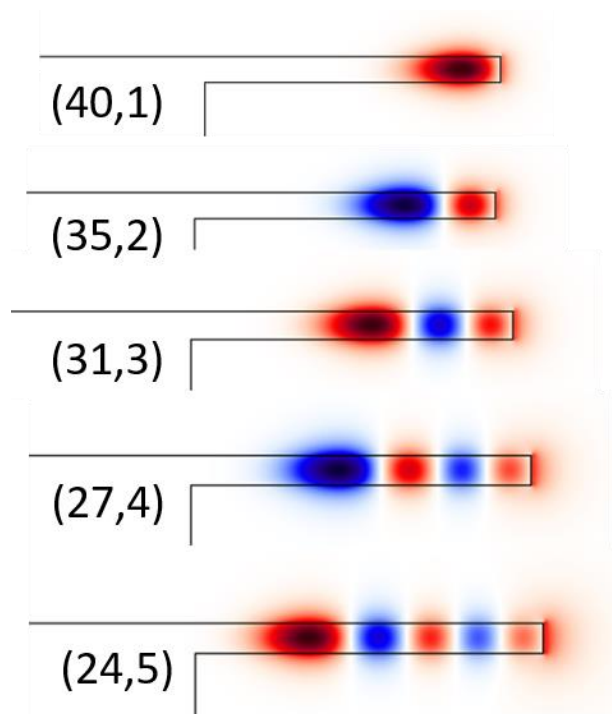


Figure 6.1: Confined modes with different radial potential. As the ring width reduces, higher order radial modes are reduced until they are not observed at all, leaving just a single mode.

Standing waves in a ring resonator, are formed by clockwise (CW) and anti-clockwise (ACW) propagating modes with arbitrary phase due to the cylindrical symmetry of the system. A typical modal field distribution of the simulated ring resonator and the mode is shown in Figure 6.2 (a). A quantum dot can be located at any point along azimuthal axis due to the arbitrary phase. However, the overlap between QD and mode fields is mainly determined by the superposition configuration. Figure 6.2(b) and (c) display the symmetric and anti-symmetric superposition, respectively. When the QD is located in the symmetric (anti-symmetric) superposition, the overlap can be maximized (minimized).

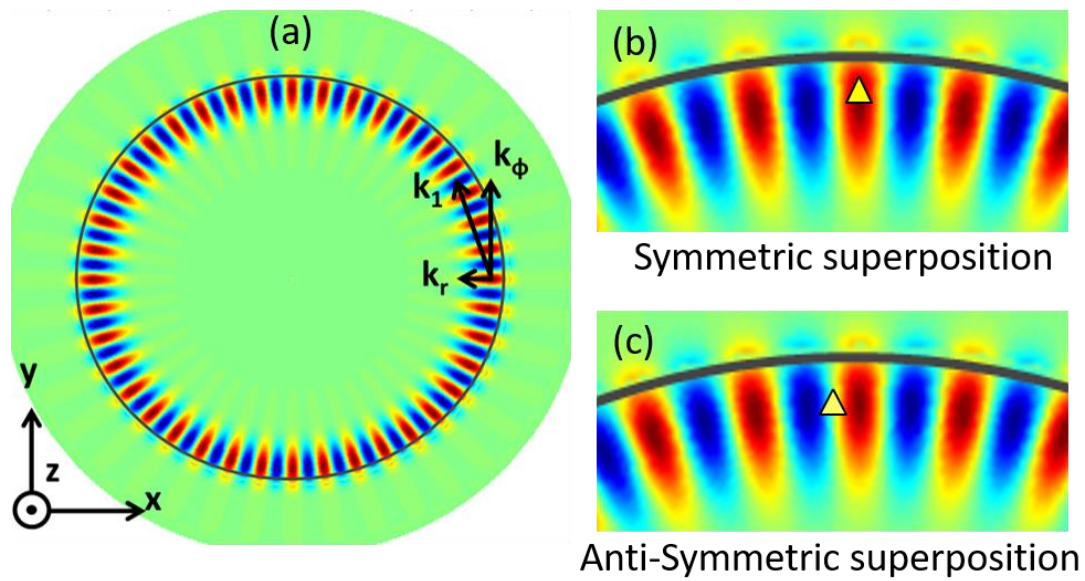


Figure 6.2: (a) is the modal field distribution; (b) and (c) indicate the symmetric and anti-symmetric superposition, respectively.

In these FDTD simulations, the rings have smooth outer and inner boundaries, suggesting that the radiative losses and scattering losses are negligible. In this case, calculating the Q factors for the ring resonators is not practical due to the extremely long time to simulate the decay dynamics of the modes.

6.2.2 Design of an All-Pass Filter using a Ring Resonator

Apart from the internal part of the modal fields, there are field components existing outside of the outer and inner sidewalls, referred to as evanescent field. This evanescent field can be coupled to a nearby resonator such as a waveguide forming an all-pass filter device, as schematically shown in Figure 6.3.

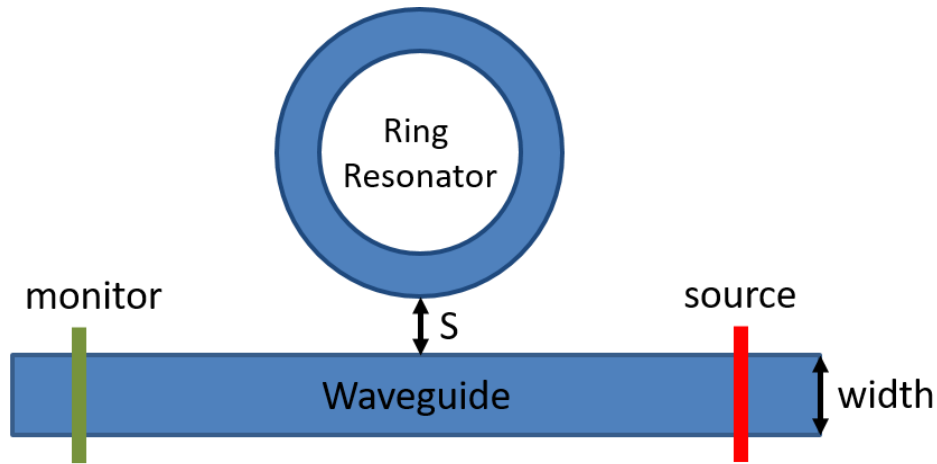


Figure 6.3: Schematic of simulated structure. The spatial separation between ring resonator and waveguide is represented by S .

In general, the coupling strength is determined by the overlapping of the evanescent fields arising from the studied devices. Here, for the all-pass filter device illustrated in Figure 6.3, the coupling strength depends on the overlapping of the evanescent field of ring resonator and that of the waveguide. The efficiency of the power transfer between the ring resonator and waveguide is sensitive to the spatial separation S . In addition, the electromagnetic field, transferred from waveguide to the ring resonator, will carry a phase shift of π when returning to the waveguide, resulting in destructive interference between the direct incoming waveguide modes and the returning resonator modes. Similar to the cases of an all-pass filter device consisting a microdisk and a waveguide, three regimes with different coupling strength: overcoupling, critical coupling, and undercoupling, can be achieved by varying the spatial separation S between the ring resonator and the waveguide. On resonance, in the regime of undercoupling (weak coupling), a dominant waveguide mode can be detected as the returning WGM cavity mode is weak and the destructive interference is incomplete; in the regime of overcoupling, as the intensities of the returning WGM cavity modes are stronger than those of the waveguide modes, it is impossible to observe complete destructive interference in the transmission spectra collected at the monitor site; while in the

critical coupling regime, the intensities of the WGM modes and the waveguides modes are equal, and a complete destructive interference can be observed in the transmittance.

Additionally, coupling efficiency of the device is also affected by the width of waveguide. In order to achieve a complete destructive interference of the cavity mode and the waveguide mode resonating in the critical coupling regime, phase matching of the modes is essential, and the effective mode indices of the WGM modes and the waveguide modes is required to be equal.

In conclusion, critically coupling can be achieved by varying the width of the waveguide and the spatial separation between the waveguide and ring resonator. A minimum transmittance at resonance is reached with a waveguide width of 220 nm and spatial separation of 80 nm in the simulation.

6.2.3 Sample Details

Based on the discussions above, an all-pass filter sample consisting of a ring resonator and a waveguide was fabricated by Dr Ben Royall. SEM images in Figure 6.4 (a) and (b) give a side-view and a top-view of the micro-ring, respectively. An overall view of the whole device can be found in Figure 6.4(c).

As described in Section 3.1, the fabrication process took place using a 140nm GaAs membrane, which contains a low density of self-assembled InAs QDs and a 1 μm sacrificial AlGaAs layer between the membrane and substrate. In order to remove the AlGaAs layer but leave the supporting pedestal for the ring resonator, the duration of HF acid underetch was carefully monitored to ensure complete removal beneath the waveguide and outcouplers. Outcouplers with $\lambda/2n$ periods were added to the ends of the waveguide and designed like a grating to scatter PL emission out of the device plane.

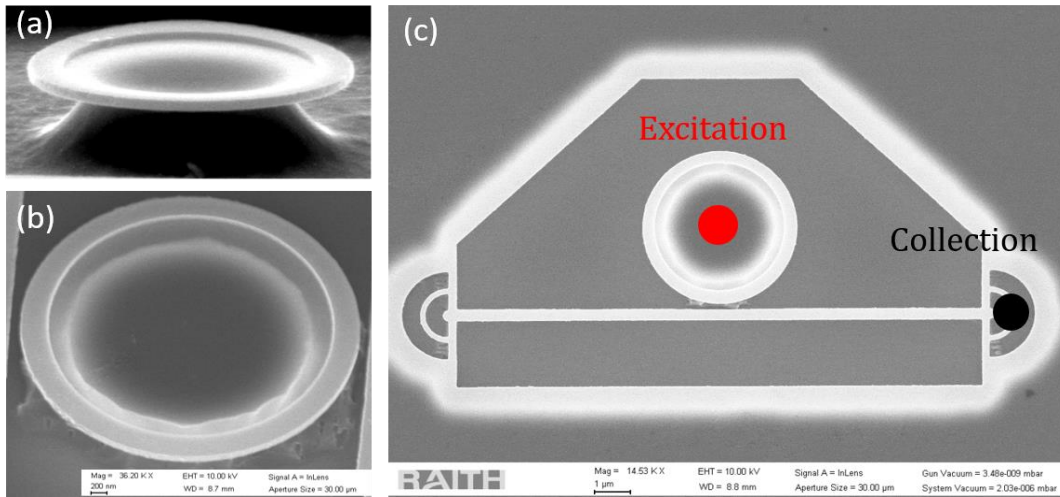


Figure 6.4: (a) is a side-view SEM image of the ring resonator; (b) shows the details of inner and outer edge of the ring resonator; (c) is a waveguide-coupled ring resonator with an inner ring radius of 2 μm , ring width of 0.35 μm and waveguide length of 13.5 μm .

6.3 Characterization of Waveguide-Coupled Ring Resonators

Photoluminescence (PL) spectra of the device were measured by exciting the quantum dot (QD) ensemble in the device using a HeNe laser with a wavelength of 633 nm. A microscope objective lens with numerical aperture of 0.5 was used to focus the laser beam. The samples were mounted in a cryostat system with continuum flow of liquid helium and an optical window, as mentioned in Section 3.2. The samples were cooled down to 4 K for the measurements.

When spectroscopically characterizing the ring resonators, the entire ensemble QDs, pumped by the 633 nm HeNe laser with 40 μW excitation power, was used as an internal broadband light source. A typical PL spectrum, obtained using the configuration illustrated in Figure 6.4(c), is presented in Figure 6.5.

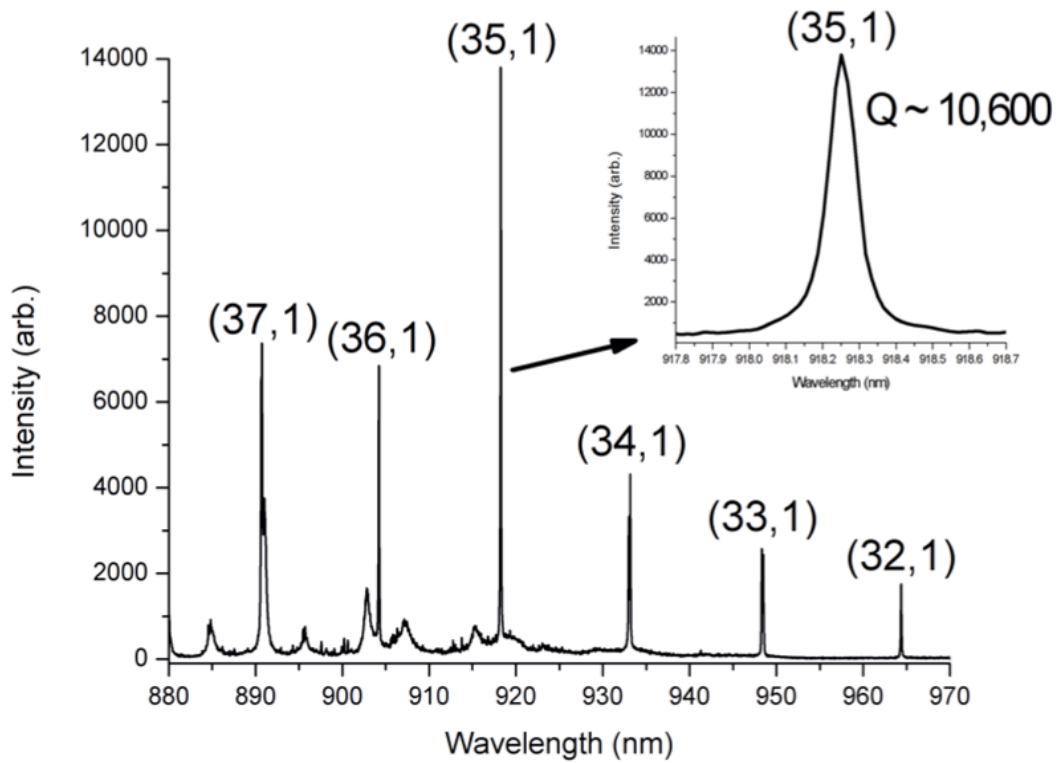


Figure 6.5: PL spectrum of waveguide-coupled ring resonator with ring radius of 2 μm , ring width of 0.35 μm and waveguide length of 13.5 μm , measured using the configuration illustrated in Figure 6.4(c).

The observed modes in Figure 6.5 can be identified by comparing with simulation results. Only the first order radial modes were observed as expected. The free spectral range (FSR) of ring resonator is about 15 nm. Figure 6.6 (a) shows an example PL spectrum of waveguide-coupled ring resonator fitted to 5 peaks corresponding to the modes. Coupling strength is determined by the overlapping of evanescent field of ring resonator and that of the waveguide, resulting in a change of the Q-factor when change the waveguide width or the ring-resonator-waveguide separation. Q-factors of modes of an ensemble of ring resonator samples can be found in Figure 6.6 (b), including from the sample with spectrum shown in Figure 6.6 (a). The spectral structure of the ring resonators is very repeatable, as shown in Figure 6.7. Due to the fabrication imperfection, 4 groups of devices were designed and fabricated. More than 200 devices with different ring-resonator-waveguide separations in each column and different waveguide widths in each line were measured in the same way. The maximum Q-factor

for the region of interest (mode around 900 nm) is achieved as high as 12,500, where the maximum Q-factor in this system can be measured up to 50,000.

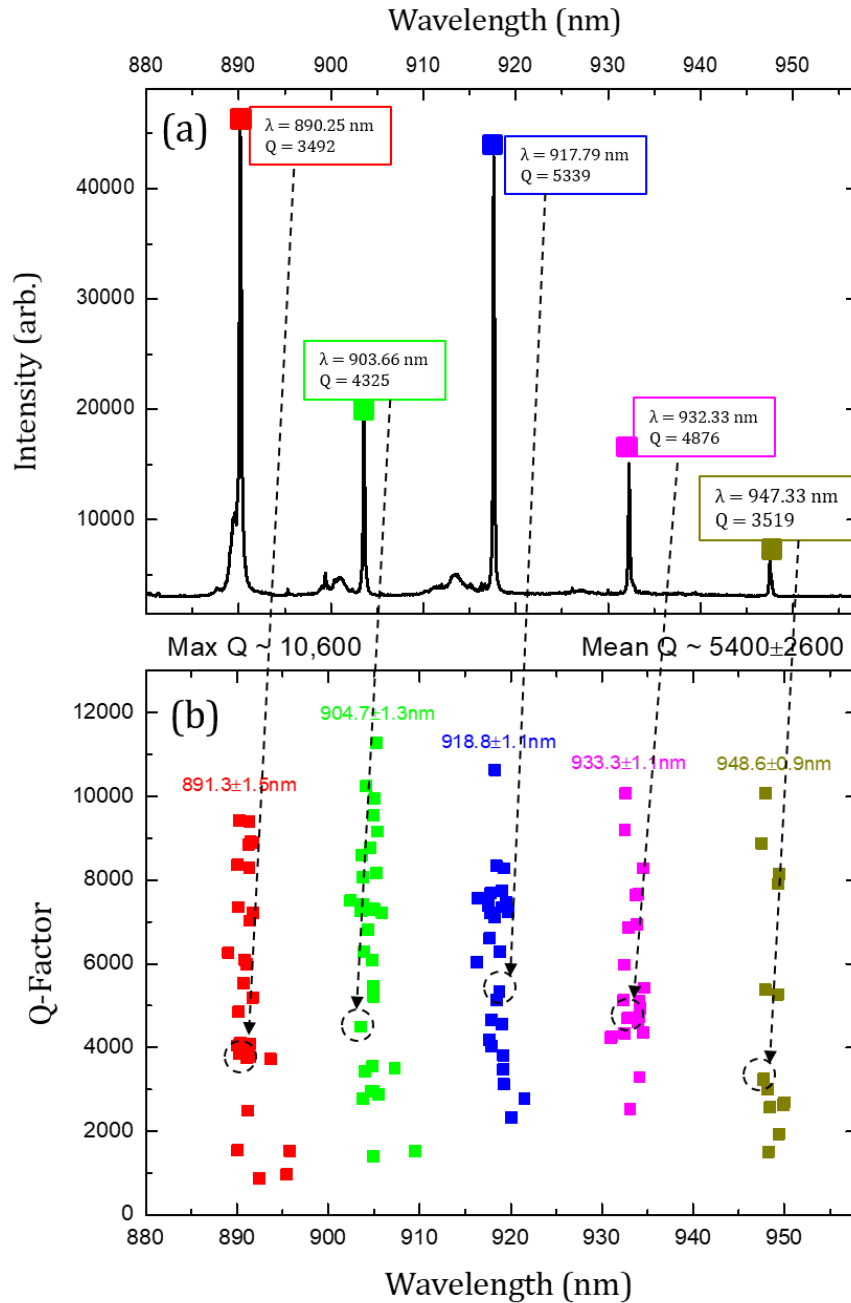


Figure 6.6: (a) example PL spectrum of waveguide-coupled ring resonator fitted to 5 peaks corresponding to the modes. (b) Q-factors of modes of an ensemble of ring resonator samples, including from the sample with spectrum shown in (a).

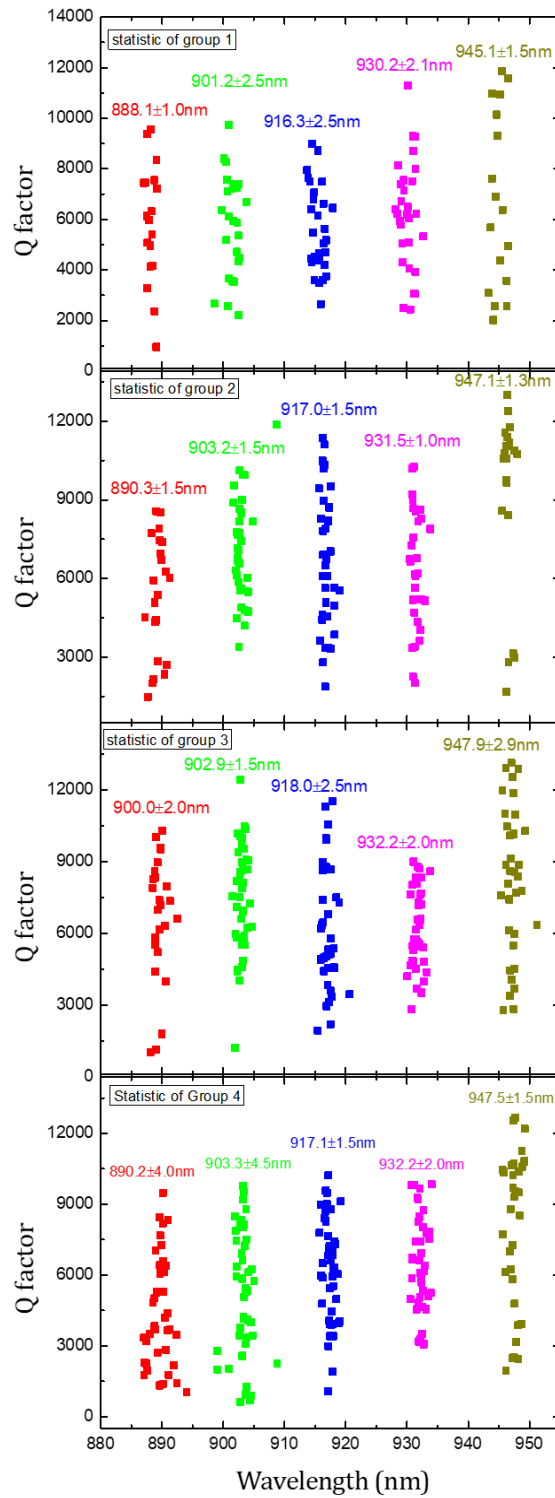


Figure 6.7: Statistics results of 200 devices with different ring-resonator-waveguide separation and waveguide width. The spectral structure of the resonators is very repeatable. The best Q factor achieved for the mode in the region of interest is 12500.

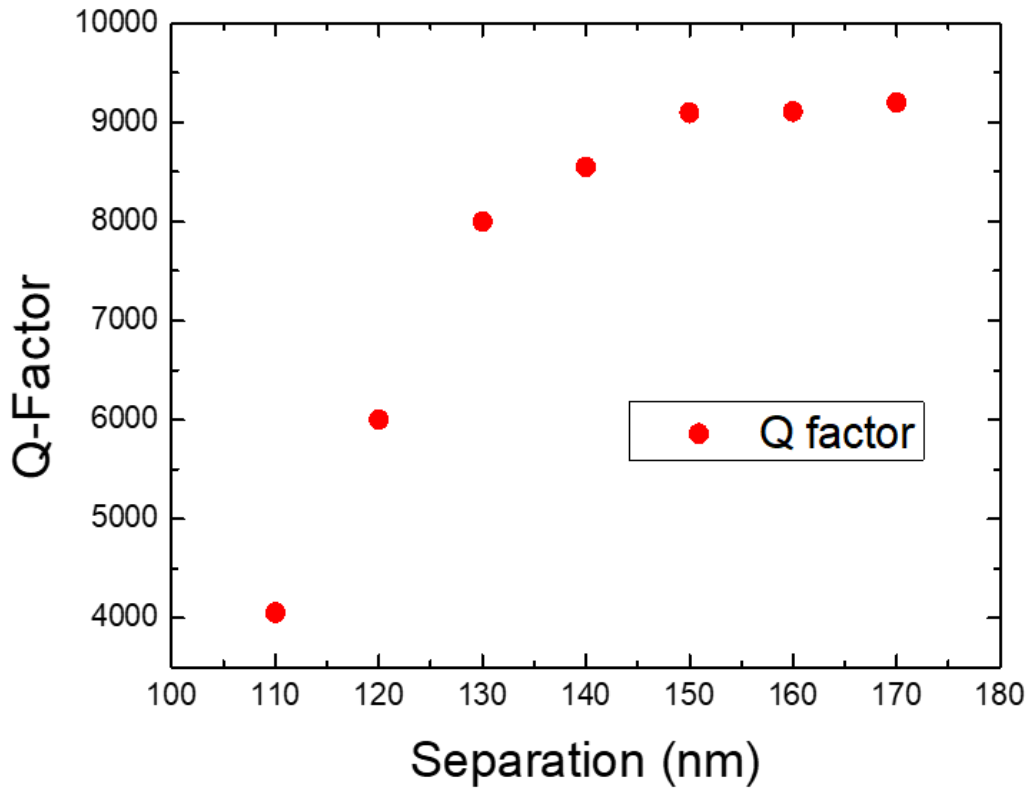


Figure 6.7: The dependence of Q-factor on ring-waveguide spatial separations, for mode (36,1), yielding the intrinsic Q-factor $Q_u = 9000$.

The dependence of Q-factor on ring-waveguide spatial separations (PL measurements on the devices with different cavity-waveguide separations whilst keeping constant waveguide width), for mode (36,1), are studied and analyzed in Figure 6.7, where the red dots are experimental data. As expected, Q-factor of the mode decreases with reducing cavity-waveguide separation as the coupling is enhanced for a closer waveguide, suggesting that a compromise between bandwidth and coupling efficiency has to be made for different application purposes. In general, the band width of a band-pass device consisting of a resonator and a waveguide, is defined as the amount of resonant signal trapped inside the resonator. It varies for different applications. A smaller resonator-waveguide separation establishes a higher coupling rate but a larger bandwidth, resulting in a decreased Q factor. For the case of large separation, the interaction between ring resonator and waveguide is weak (undercoupled) and the Q

factor is higher, which is benefit for the sharp signal filtering applications.

The intrinsic (uncoupled) Q-factor is fitted by

$$Q = Q_u(1 - e^{-2(S-S_0)/\tau}) \quad (6.2)$$

where τ is the decay constant, Q_u is the intrinsic Q-factor, and S_0 is the separation at which Q-factor equals zero. Here, for mode (36,1), the intrinsic Q-factor $Q_u = 9000$ extracted by Eq. (6.2) is much smaller than the simulated Q-factor ($> 70,000$), which can be attributed to scattering by the fabrication introduced roughness of the sidewalls of the ring resonator or waveguide in the coupling region. However, the PL emission of QD within the ring resonator remains visible from outcouplers and the effects of waveguide can be detected, suggesting that the intrinsic loss rate of the device is sufficiently low.

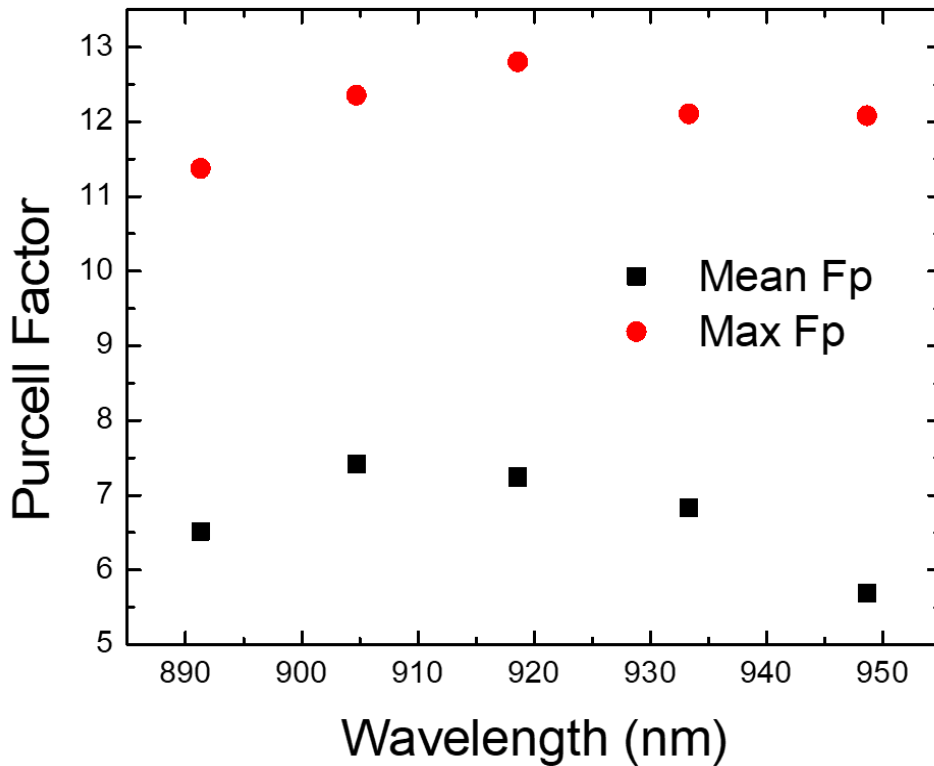


Figure 6.8: Statistics of Purcell factors for 50 ring resonator devices.

As mentioned above, in this type of coupled ring-resonator-waveguide device, an ensemble of two-level emitters (QD ensemble) is incorporated within the ring resonator

and coupled to the WGMs. Enhanced spontaneous emission of QDs (resulting from the Purcell effect) or energetic level splitting (known as Rabi splitting) at resonance may be achieved due to QD-cavity mode coupling. The QD in ring resonator, spectrally and spatially coincident with the cavity modes, can be observed from the waveguides due to the spontaneous emission enhancement and efficient coupling of the cavity modes to the waveguides. In fact, such a system is a suitable candidate for the on-chip Hanbury-Brown and Twiss (HBT) [25] experiments. In order to estimate the coupling strength of the QD-resonator system, Purcell factors are calculated from the experimental data in Figure 6.6(b). The resonant mode wavelength λ_c and the maximum and mean Q-factor are extracted from Figure 6.6(b). According to Eq. (1.8), the mode volume V_m for different modes can be estimated by using Lumerical Mode Solutions (approximately 10^{-18}). Applying λ_c , the maximum (mean) Q-factor and V_m to Eq. (1.11) gives the maximum (mean) Purcell factors of the modes at different wavelength. As shown in Figure 6.8, the mean and Max Purcell factors for the region of interest (around 900 nm) are 7.4 and 12.4, respectively. These values are high enough for indistinguishable single photon emission from QDs, indicating a high quality of the device.

6.4 On-Chip Notch Filtering

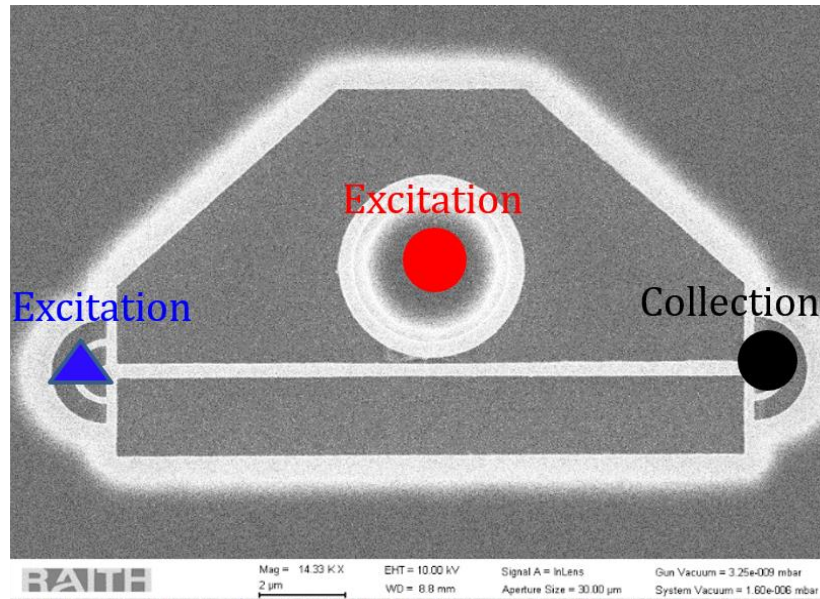


Figure 6.9: Measurement configuration for the transmission spectra.

In a coupled WGM resonator-waveguide device, dips in the transmission spectra of waveguide, can be induced by the destructive interference of the cavity modes and the driving field. Transmission measurements are performed by exciting one outcoupler of the waveguide and detecting the transmittance at the other outcoupler of the waveguide, as illustrated in Figure 6.9. To better identify the dips, a characterization PL spectrum is also measured by exciting the micro ring and collecting from the same outcoupler as was used for the transmission measurement. Transmission spectra (blue curves) of three different devices are presented in Figure 6.10, where the red peaks indicate cavity modes of the corresponding micro ring.

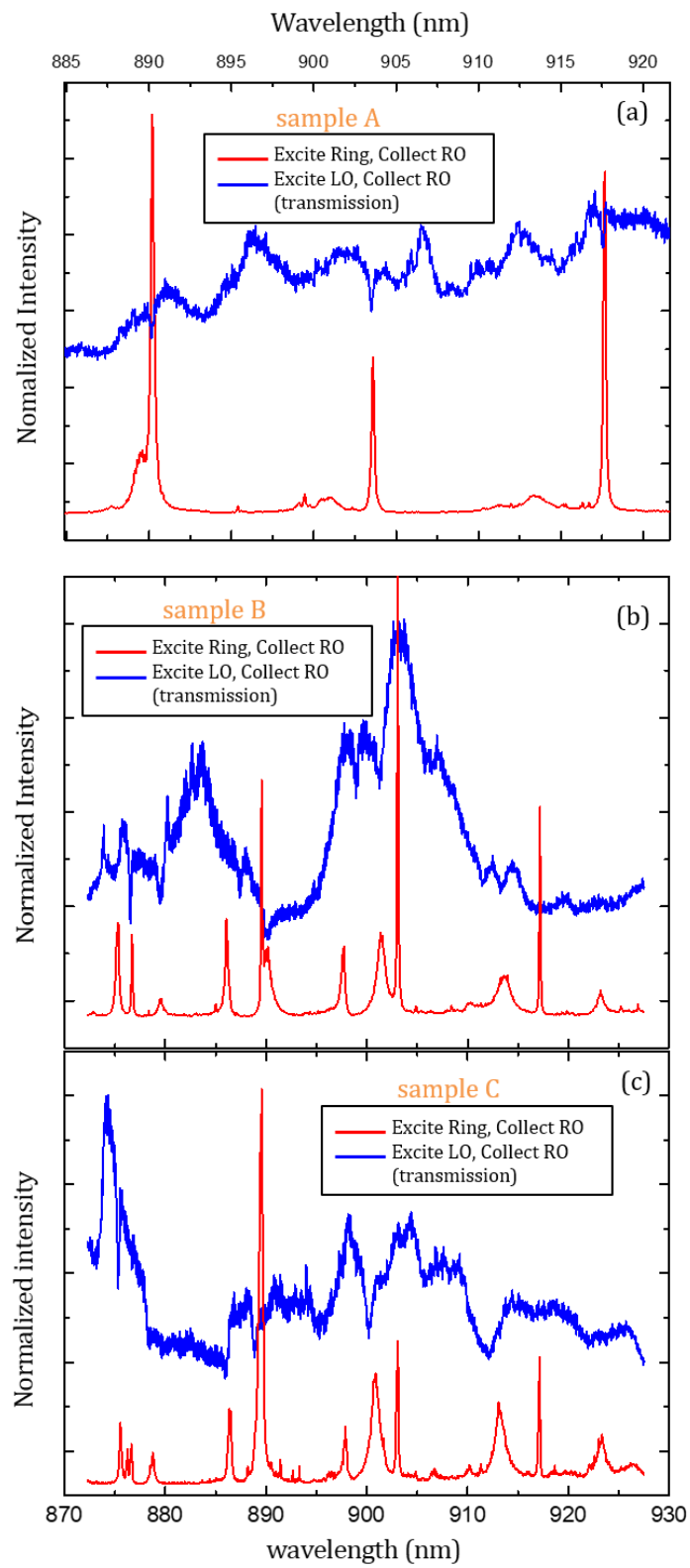


Figure 6.10: Transmission measurements for sample A, B and C, along with PL characterization of cavity modes in micro ring.

As can be noticed in Figure 6.10(c), dips are observed at wavelengths of 886, 889, 900, 912 nm, along with a slight blue shift compared with their corresponding PL peaks. Dips at these wavelengths indicate that the phase matching condition between the WGMs of the ring resonator and the propagating modes of the waveguide is satisfied. In addition, the radial mode families can also be identified from the PL spectrum. Clear dips corresponding to modes (37, 1), (36, 1) and (35, 1) are detected at 890.2, 903.6, and 917.6 nm for sample A, see in Figure 6.10 (a). Similarly, in sample B, dips appear in the transmission spectrum with a complex pattern, attributed to a complicated phase matching condition. The obvious observation of the destructive interference induced dips in transmission spectra indicates that the quality of the ring-resonator-waveguide coupling device is sufficiently high. These results also provide a potential of the device as an on-chip ultra-narrow band notch filter.

6.5 Single QD Emission and its Purcell Enhancement

The measurement of single QDs emission was carried under a weak laser power of 500 nW. Sharp emission lines of individual QDs can be observed, instead of a broad QD ensemble PL emission. The excitation laser spot, red dot in the inset of Figure 6.11, covers the coupling region of the device; while the collection spot, black dot in the inset of Figure 6.11, is focused on one of the outcouplers.

A series of PL spectra of single QDs coupled to WGMs has been taken under different temperatures in Figure 6.11. As reported in previous studies [7, 15], the emission energies of QDs are more sensitive to temperature changes than cavity modes; and QD emission may shift off/on resonance with the cavity mode as the temperature changes. In order to identify the PL peaks from different QDs and cavity modes, peak position and intensity versus temperature have been extracted and plotted in Figure 6.12(a) and (b), respectively.

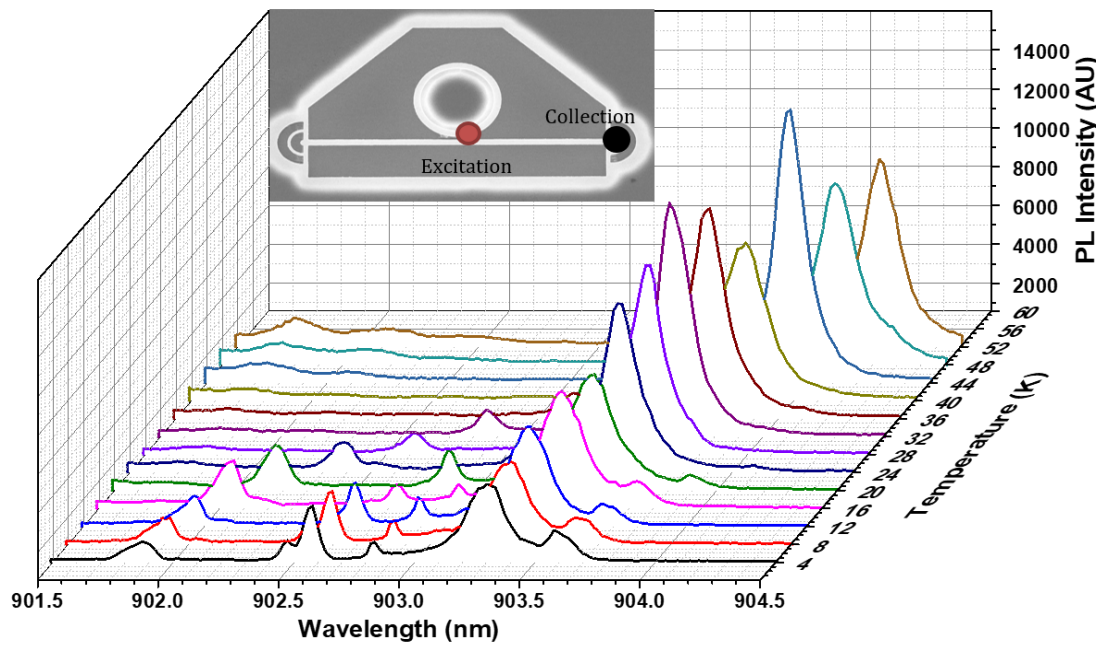


Figure 6.11: The temperature dependence of the single QDs emission. Inset: measurement configuration for the single QD PL spectra.

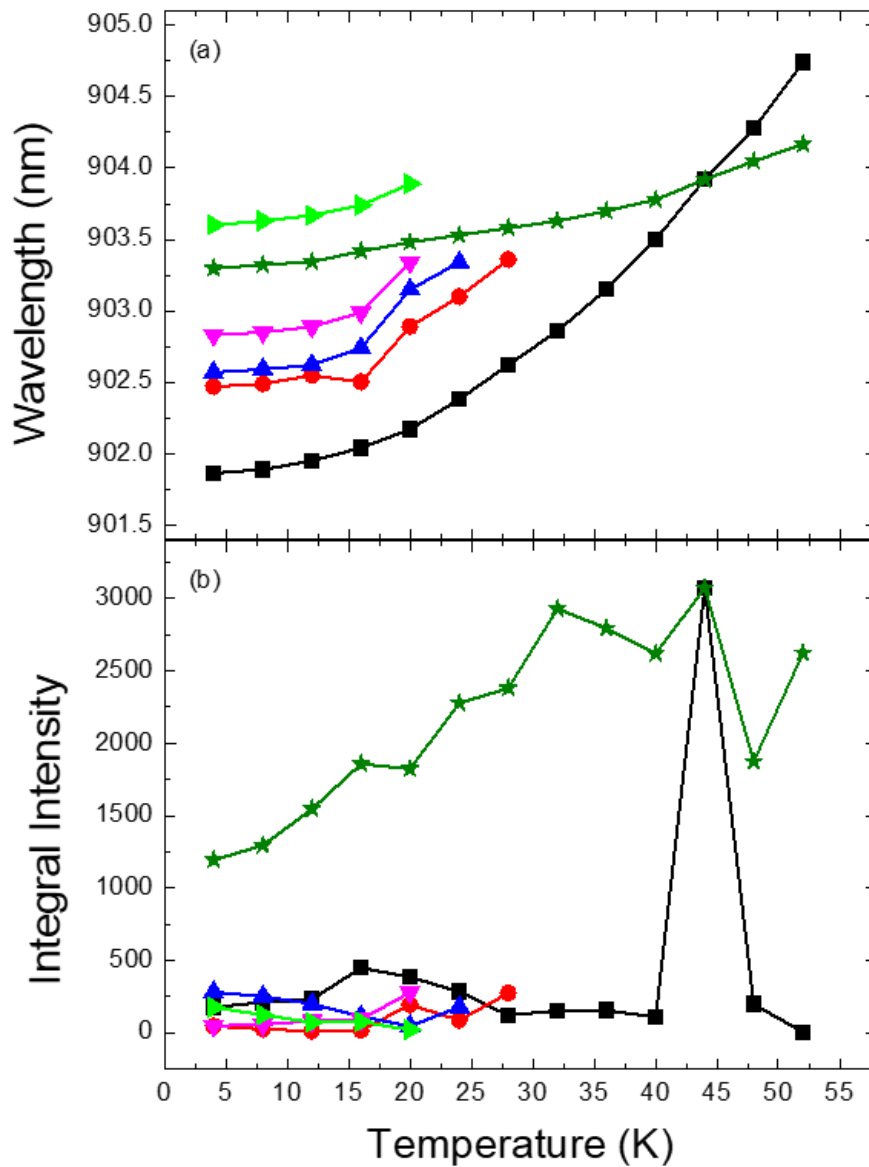


Figure 6.12: Peak positions (a) and integral PL intensities (b) extracted from Figure 6.11 as a function of the temperature.

An enhancement of PL intensity can be noticed at 903.8 nm when temperature goes up to 44 K in both Figure 6.11 and Figure 6.12. The green star curve (WGM) and black square curve (QD emission) cross over at 903.8 nm in Figure 6.12(a) with a factor of 12 increment of the QD emission intensity in Figure 6.12(b), suggesting that the QD is well

coupled to the WGM and a clear Purcell enhancement of the spontaneous emission of the QD-cavity coupling system has been achieved. Additionally, the tuning range of the QDs can be estimated roughly by Figure 6.12(a), where the black curve shows the dot can be tuned by 3 nm from 4 K to 52 K.

6.6 Add-Drop Filters using Ring Resonators

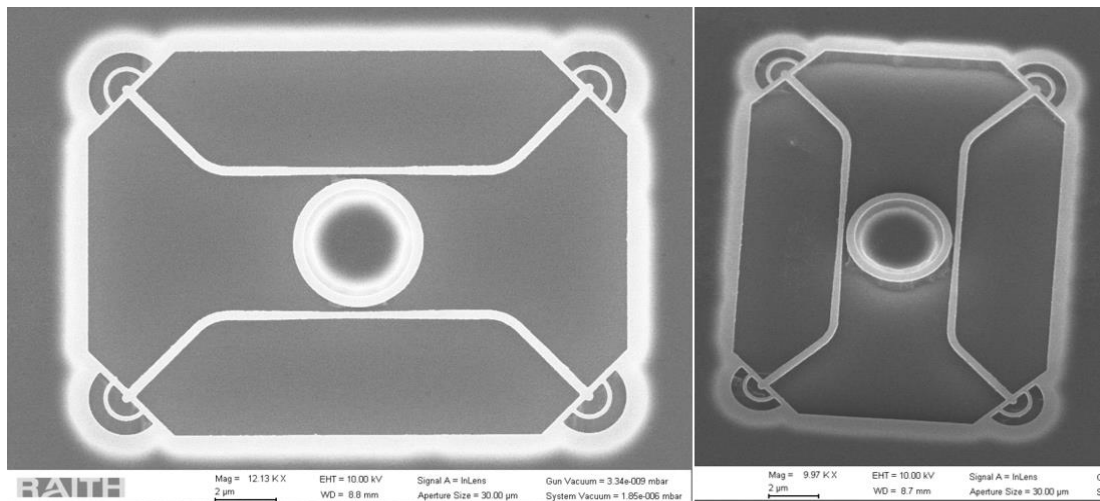


Figure 6.13: SEM images of add-drop filter using a ring resonator.

The previous sections have demonstrated the design of waveguide-coupled ring resonators for spectral filtering and enhanced single QD emission. However, in general quantum photonic circuits the QD emission may occur somewhere else in the optical circuit and the guided photons must be filtered before being detected on-chip. For this scheme, as can be found in Figure 6.13, a second waveguide is introduced to form a passive filter, allowing specific QD emission from elsewhere in the optical circuit to be transmitted.

As discussed in previous section, the propagating mode of waveguide coupled to the WGMs in the ring completes a 'lap' and couples to the waveguide again with a π phase

shift, during which optical power is transferred from waveguide to ring and back to the waveguide. If a second waveguide is added as illustrated in Figure 6.13, the optical power is picked up from the input waveguide and dropped to the second waveguide. Therefore, such a device is referred to as an add-drop filter [26-28]. Unlike detecting notches produced by destructive interference in the transmission measurements for an all-pass filter, there is no interference and notches in transmission of the second waveguide and the transmission signals are significant at resonance. At the time of writing, these devices have been fabricated and are yet characterized.

6.7 Summary

In conclusion, the on-chip spectral filtering of photon emission has been explored using ring resonators coupled to a single mode waveguide. The device parameters were optimized by “2.5 d” FDTD simulations to realize the filtering at QD wavelengths. Narrow notch filtering effect and Purcell enhancement of a single QD have been achieved by performing transmission PL spectroscopy measurements. Proposals for add-drop filters were also presented for future work.

- [1] S. Koseki, B. Zhang, K. De Greve, and Y. Yamamoto, *Appl. Phys. Lett.* 94, 2007 (2009).
- [2] B. Gayral, J.-M. Gérard, A. Lematre, C. Dupuis, L. Manin, and J. L. Pelouard, *Appl. Phys. Lett.* 75, 1908 (1999).
- [3] K. Srinivasan and O. Painter, *Nature* 450, 862 (2007).
- [4] P. Michler, A. Kiraz, C. Becher, W. V. Schoenfeld, P. M. Petroff, L. Zhang, E. Hu, and A. Imamoglu, *Science* 290, 2282 (2000).
- [5] E. M. Purcell, 'Proceedings of the American Physical Society', *Phys. Rev.* 69, 681 (1946).
- [6] S. Haroche, D. Kleppner, *Physics Today* 42, 24 (1989).
- [7] A. Kiraz, P. Michler, C. Becher, B. Gayral, A. Imamolu, L. Zhang, E. Hu, W. V. Schoenfeld, and P. M. Petroff, *Appl. Phys. Lett.* 78, 3932 (2001).
- [8] P. Michler, A. Kiraz, L. Zhang, C. Becher, E. Hu, and A. Imamoglu, *Appl. Phys. Lett.* 77, 184 (2000).
- [9] B. D. Jones, M. Oxborrow, V. N. Astratov, M. Hopkinson, A. Tahraoui, M. S. Skolnick, and A. M. Fox, *Optics express* 18, 22578 (2010).
- [10] T. Yoshie et al, *Nature* 432, 200–203 (2004).
- [11] E. Peter, E. Peter, P. Senellart, D. Martrou, A. Lemaître, J. Hours, J. M. Gérard, and J. Bloch, *Phys. Rev. Lett.* 95, 067401 (2005).
- [12] S. Koseki, "Monolithic Waveguide Coupled Gallium Arsenide Microdisk Microcavity Containing Indium Gallium Arsenide Quantum Dots" (Stanford University, 2008).
- [13] E. Waks and J. Vuckovic, *Phys. Rev. Lett.* 96, 1 (2006).
- [14] D. Englund, A. Faraon, I. Fushman, N. Stoltz, P. Petro, and J. Vuckovic, *Nature* 450, 857 (2007).
- [15] A. A. Garnier, C. Simon, J. M. Gerard, and J. P. Poizat, *Physical Review A* 75, 053823 (2007).

- [16] M. G. Tanner, C. M. Natarajan, V. K. Pottapenjara, J. A. O'Connor, R. J. Warburton, R. H. Hadfield, B. Baek, S. Nam, S. N. Dorenbos, E. B. Urea, T. Zijlstra, T. M. Klapwijk, and V. Zwiller, *Appl. Phys. Lett.* 96, 221109 (2010).
- [17] C. C. M. Natarajan, M. M. G. Tanner, and R. H. Hadfield, *Superconductor Science and Technology* 25, 63001 (2012).
- [18] G. Reithmaier, S. Lichtmannecker, T. Reichert, P. Hasch, K. Muller, M. Bichler, R. Gross, and J. J. Finley, *Scientific Reports* 3, 1901 (2013).
- [19] J. P. Sprengers, A. Gaggero, D. Sahin, S. Jahanmirinejad, G. Frucci, F. Mattioli, R. Leoni, J. Beetz, M. Lerner, M. Kamp, S. Hing, R. Sanjines, and A. Fiore, *Appl. Phys. Lett.* 99, 2013 (2011).
- [20] Katsuaki Yamada, Kyu Jin Lee, Yeong Hwan Ko, Junichi Inoue, Kenji Kintaka, Shogo Ura, and Robert Magnusson, *Optics Lett.* 42, 4127 (2017).
- [21] Wonjoo Suh and Shanhui Fan, *Appl. Phys. Lett.* 84, 4905 (2004).
- [22] Leo H. Spiekman, *Optical Fiber Telecommunications IV-A (Fourth Edition)*, Chapter 14.
- [23] J. Heebner, R. Grover, T. Ibrahim, and T. A. Ibrahim, *Optical Microresonators: Theory, Fabrication, and Applications*, Springer (2007).
- [24] N. C. Frateschi and A. F. J. Levi, *Appl. Phys. Lett.* 2934, 2932 (1995).
- [25] R. Hanbury Brown and R. Q. Twiss, *Nature* 178, 1046 (1956).
- [26] B. E. Little, S. T. Chu, H. A. Haus, J. Foresi, and J. P. Laine, *J. Lightwave Technol.* 15, 998 (1997).
- [27] Zexuan Qiang, Weidong Zhou, and Richard A. Soref, *Opt. Express* 15, 1823 (2007).
- [28] T. Barwicz, M. Popovic, P. Rakich, M. Watts, H. Haus, E. Ippen and H. Smith, *Opt. Express* 12, 1437 (2004).

Chapter 7

Conclusions and Outlooks

This thesis has focused on the study of III-V semiconductor optical microcavities and single quantum dots, which are potential building blocks for the integrated quantum optical circuits.

Chapter 1 introduced the general properties of semiconductor quantum dots including the growth mechanism, electronic structure, and optical response. The general picture of semiconductor optical microcavities and the basic principles of cavity QED of coupled optical cavity-QD systems have also been presented. Following this introductory chapter, Chapter 2 and Chapter 3 present the details of the computational, fabrication and experimental methods related to this thesis.

In Chapter 4, single spins and the nuclear spin matrix of the GaAs/AlGaAs nanohole-filled droplet epitaxial (NFDE) QDs are studied using PL and NMR spectroscopy. A close-to-zero electron g -factor for the NFDE QDs are revealed by the magneto-PL measurements. Efficient dynamic nuclear polarization as large as 65% is also demonstrated. By applying radio-frequency excitation in the NMR experiments, a residual strain as small as $<0.02\%$ in the NFDE grown QDs is revealed. Two subgroups of ensemble QDs (corresponding to those formed in the nanoholes and at the rims of the nanoholes, respectively) with compressive and tensile strain along the growth axis were

investigated. In the NFDE grown QDs, small quadrupolar effects (~ 20 kHz) and thus a large increment of the electron spin coherence time was observed due to the small strain. Despite the relatively small residual strain, stable nuclear spin matrix with a relaxation time >500 s can be deduced.

The results in this chapter suggest that the NFDE QDs can be promising candidates for spin qubit manipulation as decoherence effects from the nuclear spin environment can be largely minimized.

In Chapter 5, properties of coupled photonic-molecules (L3 photonic crystal cavities), such as energy splitting, quality factor and electric field distribution of the fundamental modes, have been studied using numerical FDTD and GME methods. A continuous variation of the energy splitting with the end-hole shift of the cavity, together with a large tuning range and symmetry-reversible bonding and anti-bonding states, have been calculated both in numerical simulation and theoretical model. The calculations agree well with optical spectroscopic experimental measurements. Continuous tuning of the coupling strength has been demonstrated experimentally, however, symmetry exchange via end-hole displacement is yet to be demonstrated in the experiments. A far-field analysis of the angular emission pattern [1-4] opens up a way to experimentally identify the symmetry of localized modes in coupled photonic-molecules, due to the fact that the spatial distribution of localized modes may change from a bonding (B) state to an antibonding (AB) state.

As the position of end-hole have a significant impact on the coupling of photonic cavities and there is growing interest in controlling the coupling between distant quantum emitters in integrated photonic structures, it is worthwhile to analyze the radiative coupling [5, 6] and entanglement [7-9] in such a system, where two quantum dots are placed in a photonic-molecule (two L3 cavities) individually and their coupling and entanglement are tuned by the end-hole displacement.

Due to the ability of trapping and storing photons and the interactions with various gain and nonlinear media (such as quantum dots), photonic cavities are key components to form coupled states on-chip and to realize the next-generation photonic circuits for quantum information processing. Strong coupling between distant photonic nanocavities and its dynamical control have been demonstrated experimentally in Si

system [10], and the preliminary results in Section 5.7 indicate the feasibility in III-V semiconductors. As a potential candidate to implement quantum computation, III-V semiconductor quantum dots can be introduced into such a system, where the strong coupling between distant cavities are induced by a waveguide. Further investigations of long-distance superradiance and entanglement are therefore worthwhile.

Chapter 6 explores the application of WGMs for on-chip spectral filtering. The mode structure and transmission spectra of ring resonators coupled to a single mode waveguide have been studied by using “2.5D” FDTD simulations, where parameters are optimized to realize the filtering at QD wavelengths. The ultra-narrow notch filtering effect has been achieved and demonstrated using photoluminescence spectroscopy measurements. Purcell enhancement of a single QD has been revealed using transmittance spectroscopy. The work presented in this chapter has demonstrated a design for spectral filtering. Moving forwards, it will be interesting to continue investigation of add-drop filters using ring resonator. Furthermore, the response from coupled ring resonators can be custom designed into various integrated optical devices, such as a filter with a flat top, or a reflector device for an integrated semiconductor optical amplifier serving as a laser.

- [1] N. Caselli, F. Intonti, F. Riboli, A. Vinattieri, D. Gerace, L. Balet, L. H. Li, M. Francardi, A. Gerardino, A. Fiore, and M. Gurioli, *Phys. Rev. B* 86, 035133 (2012).
- [2] N. Le Thomas, R. Houdre, M. V. Kotlyar, and T. F. Krauss, *Phys. Rev. B* 77, 245323 (2008).
- [3] M. L. M. Balistreri, H. Gersen, J. P. Korterik, L. Kuipers, and N. F. van Hulst, *Science* 294, 1080 (2001).
- [4] F. Intonti, F. Riboli, N. Caselli, M. Abbarchi, S. Vignolini, D. S. Wiersma, A. Vinattieri, D. Gerace, L. Balet, L. H. Li, M. Francardi, A. Gerardino, A. Fiore, and M. Gurioli, *Phys. Rev. Lett.* 106, 143901 (2011).
- [5] J. P. Vasco, P. S. S. Guimaraes, and D. Gerace, *Phys. Rev. B* 90, 155436 (2014).
- [6] G. Parascandolo and V. Savona, *Phys. Rev. B* 71, 045335 (2005).
- [7] J. Cho, D. G. Angelakis, and S. Bose, *Phys. Rev. A* 78, 022323 (2008).
- [8] J. M. Raimond, M. Brune, and S. Haroche, *Rev. Mod. Phys.* 73, 565 (2001).
- [9] J. P. Vasco, D. Gerace, P. S. S. Guimaraes and M. F. Santos, *Phys. Rev. B* 94, 165302 (2016).
- [10] Yoshiya Sato, Yoshinori Tanaka, Jeremy Upham, Yasushi Takahashi and Susumu Noda, *Nature Photonics* 6, 56 (2012).